

Université de Lille 1, Sciences et Technologies
L'Ecole Doctorale SMRE

N° d'ordre : 40508

PHD THESIS

To obtain
Doctor of Science

Of the University of Science and Technology of Lille
In
Laboratory of Atmospheric Optics

ANALYSES OF AEROSOL CHARACTERISTICS OVER EAST ASIA USING POLDER OBSERVATIONS

By

Xiaoli SU

Supervised by

Philippe GOLOUB and Hongbing CHEN

Reviewers : Xiang-ao XIA Professor at IAP/CAS

Jean-Claude Roger Professor at LMP/UBP

Zhengqiang LI Professor at IRSA/CAS

Examiners : Da-ren LU Professor at IAP/CAS

Zhongxiang HONG Professor at IAP/CAS

Isabelle Chiapello Associate Scientist CNRS
at LOA/USTL

Université de Lille 1, Sciences et Technologies
L'Ecole Doctorale SMRE

N° d'ordre : 40508

PHD THESE

pour obtenir le grade de :
Docteur de l'Université de Lille I

Spécialité :
Lasers, Molécules, Rayonnement Atmosphérique

soutenue le 10 Mai 2011 par
Xiaoli SU

Titre :

Analyse des aérosols en Asie à partir des observations spatiales de POLDER

JURY

Xiang-ao XIA	Rapporteur
Jean-Claude Roger	Rapporteur
Zhengqiang LI	Rapporteur
Da-ren LU	Examineur
Zhongxiang HONG	Examineur
Isabelle Chiapello	Examineur et co-encadrant
Philippe GOLOUB	Directeur de thèse
Hongbin CHEN	Directeur de thèse

Laboratoire d'Optique Atmosphérique
U.F.R de Physique Fondamentale
Université des Sciences et Technologies de Lille
59655 Villeneuve d'Ascq
France

Acknowledgements

There are so many people who more or less contribute to making this thesis possible and to whom I owe deep gratitude.

My deepest gratitude goes first and foremost to my advisors, Prof. Philippe Goloub and Prof. Hongbin Chen. They together figure out a perfect blend of big thinking and gave me the opportunity to work closely with them. Prof. Goloub has not only offered me valuable guidance in the academic studies, but also helped me a lot to adapt to the new environment in France. His enlightening instruction and constructive criticism have contributed greatly to the completion of this thesis. I will never forget the happy moments spent with his family during the festival days and I am greatly indebted to their cordial hospitality, friendliness and thoughtfulness. Prof. Chen, a respectable, responsible and resourceful scholar, has provided me a vast scope to develop the framework for this thesis and afforded me precious opportunities to broaden my vision and improve my research capabilities. Without the tremendous assistance and friendly encouragement from these two advisors, this thesis could not have reached its present form. I sincerely appreciate all their support, generosity, and, above all, patience.

My second thanks are given to all my collaborators. I have enjoyed working with Dr. Isabelle Chiapello, Pro. Jean-Luc Deuzé, Zhengqiang Li since I learned so much from your carefulness, your patience and your great experiences in research and writing papers. I am also grateful to Dr. Fabrice Ducos, for preparing the datasets and giving many valuable suggestions on shell scripts. I would like to express my heartfelt gratitude to Prof. Jean-Claude Roger and Xiang'ao Xia, for their valuable comments to my thesis.

Moreover, I would thank my French colleagues, Neda Boyouk, Nicolas Ferlay, Thierry Podvin, Fabien Waquet, Isabelle Jankowiak, Shan Zeng, Oleg Doubovik, Luc Blarel, Virginie Buchard, Romain De Filippi, Christine Deroo, Maurice Herman, Andrée Giard, Marie-Lyse Liévin, Frédéric Parol, Colette Brogniez et al in LOA. Special thanks to Nanying Zhao, who's now also my good friend, for her tender thoughtfulness in France. Thanks to their help with my work and life, I have an unforgettable and pleasant experience in LOA, Lille. Grateful acknowledgements are also made to all the teachers in IAP, Daren Lu, Xiushu Qie, Pucal Wang, Jianchun Bian, Ying Chen, Ronghua Liu, Pengyu Sun, Xuehua Fan, Yanliang Zhu, Wenying He et al., who's rigorous scholarship and impressive kindness enlighten me not only during my study for a doctorate but also in my future.

The most wonderful thing in my Ph.D. life is living in two cities with different cultures, Lille and Beijing, which enables me to make innumerable friends. I would like to express my gratitude to these friends who are either teachers or students at USTL or IAP. I have been enjoying the amazing time in Lille with Haibo Wang, Ling Shang, Quan Xu, Luanluan Xue, Tao Zeng, Ji He and Yuanyuan Zheng for being foreigners together. I also would like to sincerely thank all my friends in IAP, Meijing Lin, Ying Zhang, Rui Wang, Jun Li, Junrong Xia, Liang Peng et al. for helping me and sharing their knowledge with me.

I give special thanks to my parents, my brother and sister, for their so many years of love, care and encouragement. I especially thank my husband, Ke Hai, who is always on my side and comforts me whenever I got depressed or frustrated over the last five years. Without him, this thesis could not be finished.

Lastly, I gratefully acknowledge the French Embassy in China for financing my wonderful studies in USTL.

Contents

Abstract	1
Résumé	2
Chapter 1 Introduction	3
1. 1 Microphysical and chemical properties of atmospheric aerosols	4
1. 1. 1 Aerosol size distributions	4
1. 1. 2 Major chemical components of aerosols	8
1. 2 Optical properties of atmospheric aerosol	11
1. 2. 1 Optical processes of aerosol particles	11
1. 2. 2 Parameters characterizing aerosol optical properties	13
1. 3 Aerosol vertical distribution	17
1. 4 Aerosol measurement techniques	19
1. 5 Impacts of atmospheric aerosols	23
1. 5. 1 Effects on the radiation and climate	24
1. 5. 2 Effects on human health and environment	26
1. 6 Motivations and outline of the thesis	27
Chapter 2 Data Collection Descriptions	31
2. 1 AERONET/PHOTONS measurements and inversions	31
2. 1. 1 Automatic sun and sky scanning spectral radiometer	32
2. 1. 2 AERONET direct measurements and aerosol inversions	35
2. 2 Satellite aerosol retrievals	39
2. 2. 1 The “A-Train” Constellation	39
2. 2. 2 Description of POLDER-2/-3 and MODIS radiometers	42
2. 2. 3 Aerosol retrieval algorithm of POLDER and MODIS over land	46
2. 2. 3. 1 Aerosol retrieval algorithm from POLDER observations over land	48
2. 2. 3. 2 Aerosol retrieval algorithm from MODIS observations over land	51
2. 2. 4 Aerosol retrieval algorithm from POLDER (2-3) and MODIS over ocean	55
2. 2. 5 Description of CALIOP and its aerosol retrieval algorithm	59
2. 3 Particle concentration measurements	64
2. 4 Conclusion and Strategy	66
Chapter 3	69
Regional validation of POLDER-3 aerosol retrievals over land	69
3. 1 Data collection and processing	69
3. 1. 1 AERONET data and processing method	70
3. 1. 2 POLDER level 2 aerosol products and processing method	73
3. 2 Results and Discussion	74
3. 3 Conclusions	78
Chapter 4	79

Characteristics of aerosol loads over East Asia from POLDER observations	79
4. 1 Characteristics of POLDER AOD distribution over East Asia	80
4. 1. 1 Spatial distribution patterns of aerosol loads from POLDER	80
4. 1. 2 Seasonal variability of POLDER AOD over East Asia	83
4. 1. 3 Results and Discussion	85
4. 2 Year-by-year evolution of summer aerosol loads in North China region	86
4. 2. 1 Inter-annual variability of summer aerosol loads over North China	87
4. 2. 2 Year-by-year evolution of aerosol loads focusing on Beijing City	92
4. 3 Conclusions	95
Chapter 5	97
Comparative analyses and fusion of POLDER and MODIS observations	97
5. 1 Data collection description and methods	99
5. 2 Results and discussions	100
5. 2. 1 Evaluation of satellite aerosol retrievals	101
5. 2. 1. 1 Fine mode Aerosol Optical Depth at 550 and 670 nm	101
5. 2. 1. 2 Total Aerosol Optical Depth at 550 and 670 nm	103
5. 2. 2 Combination of POLDER-3 and MODIS observations	104
5. 2. 2. 1 Spatial distribution patterns of coarse mode aerosols and the fine mode fraction	105
5. 2. 2. 2 Seasonal variation of coarse mode AOD over East Asia	109
5. 3 Conclusions	114
Chapter 6	117
Feasibility study of air quality remote sensing from POLDER observations	117
6. 1 Dataset description and methods	118
6. 2 Results and Discussions	121
6. 2. 1 Monthly variation and year-by-year evolutions of POLDER AOD and PM _{2.5} in different seasons over Beijing sites	121
6. 2. 2 The relation between POLDER AOD and ground-level PM _{2.5} concentrations	125
6. 2. 3 Main factors and possible improvements	128
6. 2. 3. 1 Diurnal variation of PM _{2.5} concentration over Beijing	129
6. 2. 3. 2 Aerosol vertical distribution from CALIOP	131
6.3 Conclusions	135
Chapter 7 Conclusions and Perspectives	137
7.1 Conclusions	137
7.2 Perspectives	138
Bibliography	139

Abstract

This thesis is devoted to provide a comprehensive characterization of aerosols over East Asia based on more than six years of POLDER-3 retrievals over the land surface, with ancillary dataset such as AERONET measurements and inversions, MODIS/Aqua and CALIOP/CALIPSO level 2 aerosol products, as well as PM_{2.5} concentrations measured at ground. We first performed the regional validation of POLDER-3 Aerosol Optical Depth (AOD) by comparing them with fine mode AOD (particles radius $\leq 0.30 \mu\text{m}$) computed from AERONET (Aerosol Robotic Network) inversions over 14 sites located in East Asia. The rather good correlation ($R \approx 0.92$) observed over land demonstrates the remarkable sensitivity of POLDER-3 retrievals to the smaller fraction of fine particles, mostly originating from anthropogenic sources. Considering four years of POLDER-3 Level 2 data (March 2005 to February 2009), we analyzed the characteristics and seasonal variation of aerosol distribution over East Asia. Additionally, the inter-annual variation during 2003-2009 periods of summer fine-mode AOD over North China, in particular the Beijing City region, was analyzed for the contribution to evaluating the regional impact of emission reduction enforced in Beijing during the 2008 Olympic Summer Games. Enlightened by the different characteristics of the POLDER and MODIS sensors, we depicted the distribution characteristics of coarse mode aerosols, as well as their seasonal variability, by combining the POLDER-3 aerosol retrievals over both land and ocean with the MODIS aerosol products. Finally, we discussed the potential of POLDER to assess air quality and provide some preliminary conclusions.

Key words: Aerosol remote sensing, POLDER, MODIS, Air quality

Résumé

Cette thèse a pour objectif principal de fournir une analyse de distribution et de la variabilité des aérosols en Asie à partir des observations satellitaires de POLDER-3/PARASOL au-dessus des continents. Nous avons d'abord comparé les épaisseurs optiques en aérosols (AOD pour aerosol optical depth) POLDER-3 à celles du mode fin (particules de rayon $\leq 0.30 \mu\text{m}$) calculées à partir des inversions des mesures photométriques de 14 sites AERONET. La qualité des corrélations obtenues ($R=0.92$) a démontré la bonne sensibilité des restitutions de POLDER-3 à la plus fine fraction des aérosols, qui proviennent principalement de sources anthropiques. Nous avons analysé les caractéristiques et la variabilité saisonnière des distributions en aérosols à partir de quatre années de données POLDER-3 de niveau 2 (mars 2005 à février 2009). Notre étude a montré que la distribution spatiale des aérosols du mode fin en Asie restituée par POLDER-3 était étroitement liée à celle des activités humaines. Nous avons également mis en évidence une forte variabilité saisonnière de l'AOD du mode fin qui diffère selon les zones géographiques considérées. Enfin, nous avons analysé la variabilité interannuelle sur la période 2003-2009 des AOD du mode fin en été au nord de la Chine, en particulier dans la région de Pékin, et dans le contexte des réductions d'émissions des jeux olympiques de l'été 2008. Nous avons montré que les AOD du mode fin sont relativement élevées au cours des étés 2003, 2007 et 2008. Les variations interannuelles des AOD moyennes mensuelles (juin à août) ont montré que la variabilité était maximale en juin et similaire à celle de juillet, à la différence de celle observée en août. Dans cette étude, les AOD (totale et du mode fin) mesurées par AERONET dans la région de Pékin en été sont utilisées comme références et également analysées.

Chapter 1 Introduction

Atmospheric aerosols can be defined as solid or liquid particles, with radii varying from about 2 nm to more than 100 μm , suspended in air. Aerosol particles can be directly emitted into the atmosphere by source (primary emissions e.g., sea spray aerosol, dust, biomass or fossil fuel burning aerosol, volcanic ash) or formed in the atmosphere by physicochemical processes (secondary formation, e.g., sulfates, nitrates, ammonium salts). Aerosols, which are produced from the surface due to natural processes such as the action of the wind (sea spray aerosol, desert dust), dominate the total aerosol mass. However, anthropogenic emissions of both primary particles and precursor gases contribute significantly to the total aerosol load [Andreae and Rosenfeld, 2008].

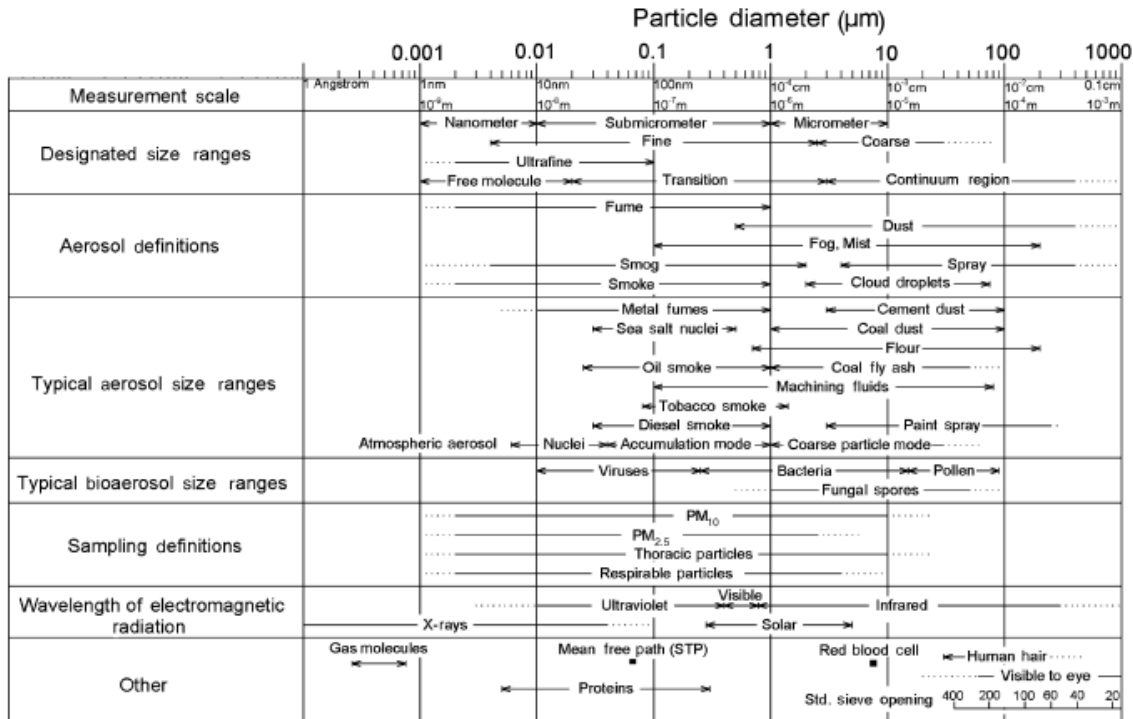


Figure 1.1: Typical aerosol particle size ranges [Hinds, 1999].

Different types of aerosols can be distinguished based on their formation processes, the size of the particles, and whether the particles are solid or liquid. Typical particle size ranges and other properties are illustrated in Figure 1.1.

1. 1 Microphysical and chemical properties of atmospheric aerosols

Aerosols are a mixture of particles (in suspension of air) of different sizes, shapes, compositions, and chemical, physical, and thermodynamic properties. They range in size from nanometers to micrometers, spanning from molecular aggregates to cloud droplets. Aerosols between about 0.1 μm and 2.5 μm in radius are among the most important in terms of impacts on climate, precipitation, visibility, degradation of air quality and human health. Most aerosols of interest are found in the troposphere and concentrated toward the Earth's surface (having a scale height about 2-3 km).

Aerosol particles can be directly emitted from sources and be formed in the atmosphere by chemical reactions and physical process, which determine the microphysical and chemical properties of aerosols. Once aerosols are formed, their properties can also be modulated in space and time by atmospheric physical and chemical process, such as condensation, evaporation and coagulation.

1. 1. 1 Aerosol size distributions

The optical properties of aerosol particles are largely determined by the ratio a/λ , where λ is the wavelength of incident light and a is the characteristic size of a particle (e.g., the radius of a droplet or the side of a cubic crystal). Therefore, information on typical sizes of aerosol particles is of great importance for aerosol optics. Aerosol size distribution, combined with their chemical properties, can be used to estimate many physical and optical properties of ambient aerosol [Nyeki *et al.*, 1998; John, 2001].

In practice, aerosol size distribution can be described by two different forms, number distribution or mass distribution, although containing the same modes. The reason for this is that particles at small end of the size distribution can be very abundant in number, but because mass depends upon the cube of diameter, such particles may contribute only small amount of the total mass. Hence, a size distribution expressed as the number of particles per size fraction will give far more emphasis to the smaller particles than a distribution expressed by mass per size fraction.

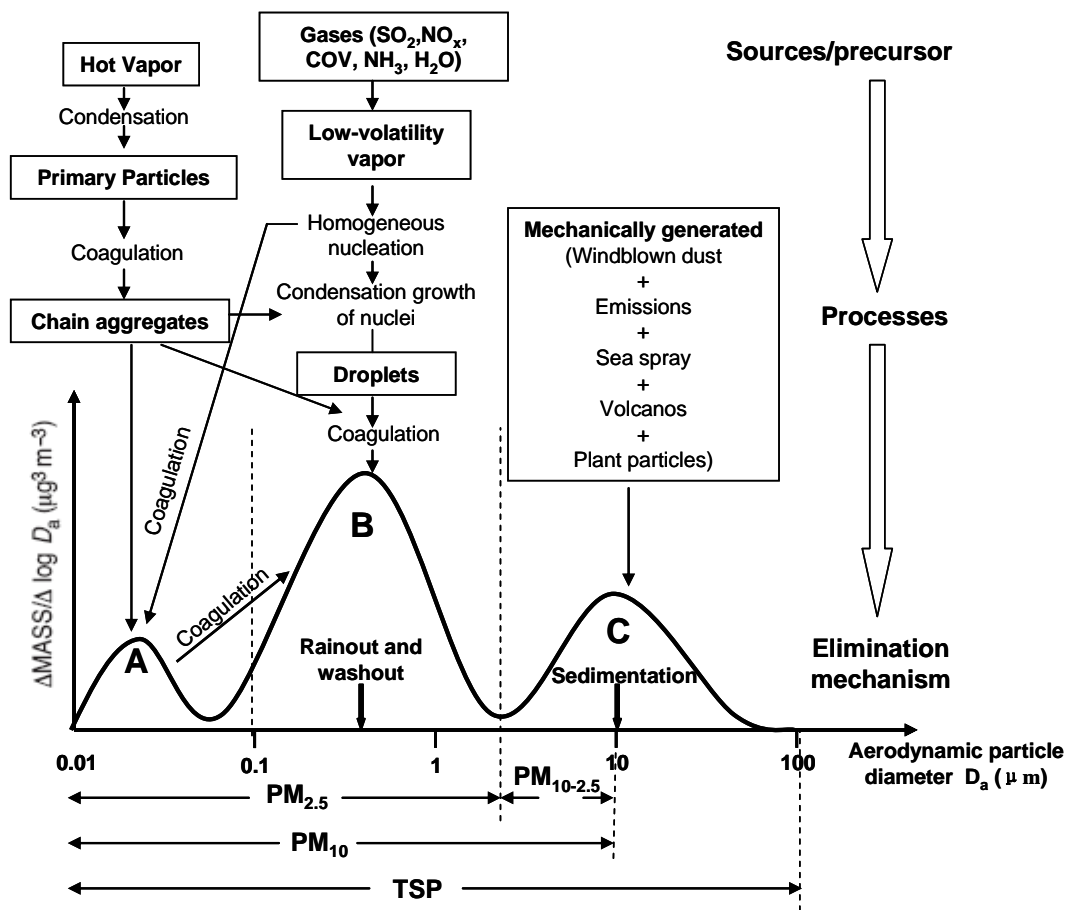


Figure 1.2: Aerosol mass distribution for an idealized ambient urban aerosol and the Schematic picture showing the physical and physico-chemical processes in the development of atmospheric aerosols (Reproduced from Whitby et al., [1980] and Wilson et al., [2002], A: Nuclei mode; B: Accumulation mode; C: Coarse mode).

Figure 1.2 shows the distribution of aerosol mass as a function of particle size for an idealized urban aerosol and the Schematic picture showing the physical and physicochemical processes in the development of atmospheric aerosols. There are several modes included in the mass distribution of particle sizes in the atmosphere. The particles in these modes are generally originated from different source types and have different atmospheric fates. The distribution of aerosol mass and other properties between these modes can vary in both space and time.

Fine mode aerosols (radius $r \leq 1.0 \mu\text{m}$) can be further subdivided into nuclei (A mode in Figure 1.2 with diameters less than $0.1 \mu\text{m}$) and accumulation modes (B mode in Figure 1.2). The nuclei-mode particles (A) are generally emitted from processes involving condensation of hot vapors, or formed within the atmosphere by gas to particle conversion. Due to their high number concentration they are subject to rapid coagulation and/or condensation of vapors (lifetime less than 1 h) and they enter the accumulation mode. The nuclei-mode aerosols are also termed “ultrafine particles” and designated as $\text{PM}_{0.1}$ (particulate matter). Likewise, the fine mode fraction with particle diameters less than $2.5 \mu\text{m}$ is also called the $\text{PM}_{2.5}$ fraction. The accumulation mode (B) particles, the other component of fine mode fraction, have a typical atmospheric lifetime of around 1-2 weeks, as removal by precipitation scavenging or dry deposition is less efficient. These particles are therefore involved in long-range transport. Aerosols larger than about $2 \mu\text{m}$ (diameter) are known as coarse particles (C mode in Figure 1.1), and are primarily from mechanical erosion of the Earth’s surface. Coarse particles include sea salt, soil dust lifted by winds and many industrial dusts. All the particles with diameters below $10 \mu\text{m}$ are designated as the “respirable” fraction and also as the PM_{10} fraction. It includes the nuclei modes, the accumulation modes and a portion of the coarse modes. TSP (total suspended particles) is then designated as the fraction that includes the nuclei, accumulation and coarse modes.

Since the Angström's empirical formula [Angström, 1929] for the wavelength dependence of the extinction coefficient was first directly related to a parameter of a Junge size distribution when the radii extend from 0 to ∞ [Van de Hulst, 1957; Junge, 1963], many different types of aerosol size distribution have been inferred using different methods [Deirmendjian, 1969; Yamamoto and Tanaka, 1969; Grassl et al., 1971; King et al., 1978]. Here, we chose the lognormal distribution type [Aitchison and Brown, 1957], which tends to be the best fit for single source natural aerosols [Hinds, 1982], to describe the distribution of particle numbers over particle size. For a single lognormal mode, the number size distribution of aerosols is:

$$n(r) = \frac{dN}{d \ln r} = \frac{N_0}{\sigma_0 \sqrt{2\pi}} \exp \left[-\frac{(\ln(r/r_0))^2}{2\sigma_0^2} \right] ; \quad (1.1)$$

Where $n(r)$ is the number size distribution with r denoting radius (in μm), N_0 is the total number of particles (Eq. 1.2). The in situ aerosol measurement community commonly defines aerosol size in terms of diameter (e.g., Seinfeld and Pandis [1998]), whereas the remote sensing community defines size by radius. Here, we define the means of the log-radius of the number (r_0) and its standard deviation (σ_0) as:

$$\ln r_0 = \frac{\int_{r_{\min}}^{r_{\max}} \ln r \frac{dN(r)}{d \ln r} d \ln r}{\int_{r_{\min}}^{r_{\max}} \frac{dN(r)}{d \ln r} d \ln r} ; \quad \sigma_0 = \sqrt{\frac{\int_{r_{\min}}^{r_{\max}} (\ln r - \ln r_0)^2 \frac{dN(r)}{d \ln r} d \ln r}{\int_{r_{\min}}^{r_{\max}} \frac{dN(r)}{d \ln r} d \ln r}} ; \quad N_0 = \int_0^{\infty} \frac{dN}{d \ln r} d \ln r ; \quad (1.2)$$

This also leads to the definition of effective radius (r_{eff}) of a distribution, i.e.,

$$r_{\text{eff}} = \frac{\int_0^{\infty} r^3 \frac{dN(r)}{d \ln r} d \ln r}{\int_0^{\infty} r^2 \frac{dN(r)}{d \ln r} d \ln r} = r_0 \exp(2.5\sigma_0^2) ; \quad (1.3)$$

We can note that the effective radius is larger than r_0 , which reflects a strong

contribution of large particles in the volume distribution.

For the particular case of hydrophilic aerosols, which have the ability to absorb water vapor (e.g., *Malm et al.*, [1994]; *Kotchenruther et al.*, [1999] and *Gasso et al.*, [2003]) and thus become involved in cloud processes and hydrologic cycle, an increase of relative humidity is often accompanied by a hysteretic increase in particle size. The influence of relative humidity RH on the radius r of the particle can be modeled via the relationship provided by *Hänel* [1976] as follows:

$$r_w = r(1 - RH)^{-e}; \quad (1.4)$$

Where the suffix w refers to wet conditions and RH is the relative humidity. r_w is the radius of aerosol particles in the wet condition. The coefficient e depends on the considered type of aerosol and is taken as 0.285 for Water Soluble (WS) [*Hanel*, 1976] and is at present unknown for Particulate Organic Matter (POM).

For aerosols composed of two or more modes, integration must be over both size bin and mode. For example, for a bimodal distribution,

$$r_{eff} = \frac{\int_0^{\infty} r^3 \frac{(dN_1 + dN_2)}{d \ln r} d \ln r}{\int_0^{\infty} r^2 \frac{(dN_1 + dN_2)}{d \ln r} d \ln r}; \quad (1.5)$$

1. 1. 2 Major chemical components of aerosols

The composition of atmospheric aerosols is seldom simple, because it is determined by the sources of primary particles and for secondary particles by the process forming the particles. Table 1.1 presents the emissions of main aerosol types in the atmosphere (in Tg per year).

Table 1.1: Emission of main aerosol types in the atmosphere (produced by Kacenenbogen, [2008] referring to Ramaswamy et al., [2001]).

		Natural Particles (with the maximum of 94%)		Anthropogenic Particles (with the maximum of 6%)	
Sources	Aerosol Type	Emission (Tg/yr)	Aerosol Type	Emission (Tg/yr)	
Primary emission	Mineral Dust	2150	Industrial Dust	100 - 200	
	Sea Salt	3340			
	Volcanic Dust	33	Carbon Soot (burning of fossil fuel and biomass)	6 - 8	
	Biogenic Debris	56			
	Carbon Soot (biomass burning)	6 - 9			
Secondary formation	Sulfates (Volcanic VOC and SO ₂ , biomass burning)	78	Sulfates (SO ₂)	122	
	Organic Carbon (VOC, biomass burning)	61- 96	Nitrates (NO _x)	14	
	Nitrates (NO _x and biomass burning)	4	Organic Carbon (burning of fossil fuel and biomass)	10 - 30	
Maximum of the total	5766		374		
Maximum of the total for all particles	6140				

As shown in Table 1.1, atmospheric aerosols consist mainly of two types of particles, natural and anthropogenic, according to their sources. The natural particles, which are dominant in the total load of aerosols (94%), are chiefly composed of coarse aerosols generally emitted by mechanical processes (e.g., mineral dust, sea salt etc) compared to the secondary aerosol formation (mostly anthropogenic particles). Table 1.1 also exhibits four predominant aerosol types (chemical components) of aerosol particles: sea salt, desert dust or dust, Organic Carbon (OC) and water soluble, each of which typically contributes about 10—30% of the overall mass load. The predominance of these chemical components is closely linked to the emitting source

and the formation mechanisms of the particles.

Sea-salt (SS) aerosol originates from the oceanic surface due to wave breaking phenomena. The largest droplets fall close to their area of origin. Only the smallest aerosol particles with size from approximately 0.1 to 1 μm are of a primary importance to the large-scale atmospheric aerosol properties. These particles can exist in the atmosphere for a long time. They have been identified over continents as well.

Mineral dust aerosols originate from the arid and semi-arid land surfaces. They are composed of solid particles, most of them being not soluble in water. Therefore, dramatic changes of the aerosol particle shape and structure in the humidity field are rare events as compared to sea-salt aerosols. However, the mineral core can be covered by a water or ice shell in high humidity conditions. This will lower the refractive indices of the particle. Another noticeable property of dust aerosol is its non-sphericity, which increases the difficulty in the modeling of its optical properties.

The carbonaceous material in atmospheric aerosols is mainly comprised of organic compounds and elemental carbon (EC). The latter is sometimes referred to as “black carbon”. OC originates from mechanical processes and by atmospheric reactions from gaseous precursors, while BC is produced only in combustion processes as a primary pollutant. The large varieties of organic compounds that are present in aerosols are generally denoted by the generic term OM or POM (Particulate organic matter). It consists of highly polymerized organic material with a low content of hydrogen and oxygen.

WSOC (Water Soluble Organic Carbon) is likely composed of chloride ions, nitrate, sulfate, lithium, sodium, ammonium, potassium, magnesium and calcium [Lioussé *et al.*, 1996]. It influences the ability of ambient aerosols to act as CNN

[*Novakov and Corrigan, 1996*], and is involved in the aqueous phase chemistry in fogs and clouds. A more detailed knowledge on WSOC will help clarifying if any negative health effects can be associated with these carbonaceous sub-fractions and can be used in assessing the sources of the OC and the extend of its atmospheric processing. Some recent studies used aerosol WSOC as an index of the formation of Secondary Organic Aerosol (SOA) [*Kumagai et al., 2009*]; and it has been suggested as an adequate quantitative tracer for SOA in the urban environment [*Favez et al., 2008*].

1. 2 Optical properties of atmospheric aerosol

Aerosol particles interact strongly with light because their particle size is often of the same order of magnitude as the wavelength of light (e.g., *Chandrasekhar, [1950]*). This interaction affects visibility and is the basis of particle concentration and size-measuring instrument. Aerosol particles interact with light by scattering, absorbing or transmitting incident light depending on their chemical composition (complex refractive index, η), size distribution, and orientation (if non-spherical). Light scattering processes dominate over processes of absorption in the visible. However, absorption of light cannot be ignored because it influences the total radiation balance considerably. The reduction in the intensity of a direct beam during its propagation through an aerosol medium is determined simultaneously by absorption and scattering processes. The sum of total light scattering in all directions and absorption is called extinction. Additionally, aerosol particles radiate the energy, which is absorbed by particles, at larger wavelength. This process is called emission. It is negligibly small at optical wavelengths.

1. 2. 1 Optical processes of aerosol particles

Scattering: The scattering of light by a particle comprise of the diffraction of light

passing around the particle, reflection of light at particle surface and refraction of light as it passes through the particle. All particles scatter light. For spherical particles smaller than 0.05 μm , visible light scattering can be calculated by Rayleigh scattering [Rayleigh, 1889]. In this size range, scattering is a strong function of particle size, proportional to particle diameter raised to the 6th power. The intensity of the Rayleigh scattered radiation increases rapidly as the ratio of particle size to wavelength increases. Furthermore, the intensity of Rayleigh scattered radiation is identical in the forward and reverse directions. For large spherical particles, greater than 5 or 10 μm , scattering is described by Mie theory [Mie, 1908]. The intensity of Mie scattered radiation is roughly independent of wavelength and it is larger in the forward direction than in the reverse direction. The greater the particle size, the more of the light is scattered in the forward direction.

Absorption: For homogeneous particles, absorption of light occurs when the material of the particle absorbs light. Usually light absorption is small and the ratio of absorption to extinction coefficients is smaller than 0.1 and even 0.01 for remote clean areas. The primary absorber of light in the atmosphere is soot [Horvath, 1993], which is very abundant over urban areas. The value of the absorption coefficient of aerosol determines the cooling or warming effect of aerosol above a scene with a given ground albedo and thus is very important for climate change. However, the characterization of atmospheric aerosol absorption is complicated due to the smaller amount of energy absorbed by aerosols, compared to the light scattered energy. Therefore, a lot of uncertainties remain in our understanding of solar light absorption by atmospheric aerosol particulate matter.

Extinction: Extinction (or attenuation) of light by aerosol is due to both light scattering and absorption. Although the chemical composition of aerosols and their size distributions are governed by a number of complex and not-well-understood

processes, the resulting spectral aerosol extinction coefficient, $\sigma_{ext} = N\overline{C_{ext}}$, where N is the number of particles in a unit volume and $C_{ext} = C_{abs} + C_{sca}$ is the extinction cross-section (the over-bar means averaging with respect to the aerosol size distribution), is often governed by the following simple analytical equation:

$$\sigma_{ext} = b\lambda^{-a}; \quad (1.6)$$

Where a is called the Angström parameter and b gives the value of the aerosol extinction coefficient at wavelength $1 \mu\text{m}$, if the wavelength λ is expressed in micrometers. Depending on the aerosol type, the actual dependence of σ_{ext} on the wavelength can be different, but the dependence as given above closely represents average atmospheric conditions.

Polarization: Polarization is one of the important properties of light, which is composed of electromagnetic waves oscillating with a high frequency. Natural light is generally unpolarized, but can be transformed to almost 100% polarized light using the phenomena of light reflection, transmission, and scattering. Polarization effects clearly play an important role in atmospheric optics and in aerosol optics in particular [Gorchakov, 1966]. They are sensitive to both the size and refractive index of particles. Also polarization characteristics of reflected light are influenced by the shape and internal structure of scatter. Therefore, they enable the solution of a number of inverse aerosol optics problems including aerosol remote sensing from aircraft, space and ground [Chowdhary et al., 2005].

1. 2. 2 Parameters characterizing aerosol optical properties

In order to quantify and characterize aerosol optical properties more accurately, some geophysical parameters have been defined and analyzed.

Aerosol Optical Depth (AOD): Aerosol optical depth, AOD (τ), is a measure of radiation extinction due to the interaction with aerosol particles in the atmosphere, primarily due to the processes of scattering and absorption. This dimensionless parameter is defined as the integrated extinction coefficient, σ_{ext} , over a vertical column of unit cross section from the surface to the top of the atmospheres (TOA), i.e.

$$\tau(\lambda) = \int_0^{TOA} \sigma_{ext}(\lambda, z) dz ; \quad (1.7)$$

For a single spherical aerosol particle, the extinct coefficient can be written as:

$$\sigma_{ext}(\lambda, z) = \int_0^{\infty} \pi r^2 Q_{ext}(\eta, r, z, \lambda) n(r, z) dr ; \quad (1.8)$$

Where Q_{ext} is the extinction efficiency, which depends on the refraction index (η), the particle size (r), the wavelength (λ), and the altitude (z). n is the size distribution of a set of particles depending on the altitude.

Aerosol Angström Coefficient: It is an exponent that expresses the spectral dependence of aerosol optical depth with the wavelength of incident light. The spectral dependence of aerosol optical depth can be approximated (depending on size distribution) by [Angström, 1964],

$$\tau(\lambda) = k \lambda^{-\alpha} ; \quad (1.9)$$

Where k is a constant and α is aerosol Angström coefficient (exponent). For measurements of optical depth $\tau(\lambda_1)$ and $\tau(\lambda_2)$ taken at two different wavelengths λ_1 and λ_2 respectively, the Angström exponent can be derived by:

$$\frac{\tau(\lambda_1)}{\tau(\lambda_2)} = \left(\frac{\lambda_1}{\lambda_2} \right)^{-\alpha} ; \quad (1.10)$$

The Angström exponent is inversely related to the averaged size of the particles in the

aerosol: the smaller the particles, the larger the exponent. Thus, aerosol Angström exponent is a useful quantity to assess the particle size of atmospheric aerosols. Generally, the Angström exponent ranges from values close to 0 (very large particles, for example, desert dust) to 3 (very fine particles, for example, urban pollution). It should be noted that coarse particles may have a slightly negative Angström exponent in some cases.

Refraction Index: The complex refraction index ($\eta = \eta_r + i\eta_i$) express the scattering and absorption of radiation by a single aerosol particle, where the real part represents scattering and the imaginary part represents absorption. The refraction index is strongly dependent on the chemical composition of the particle, the relative humidity and the wavelength. Following *Shettle and Fenn [1979]*, the real and imaginary parts of the complex refractive index for urban, rural and maritime aerosols, as a function of wavelength, are shown in Figure 1.3. The results for pure water are shown as references.

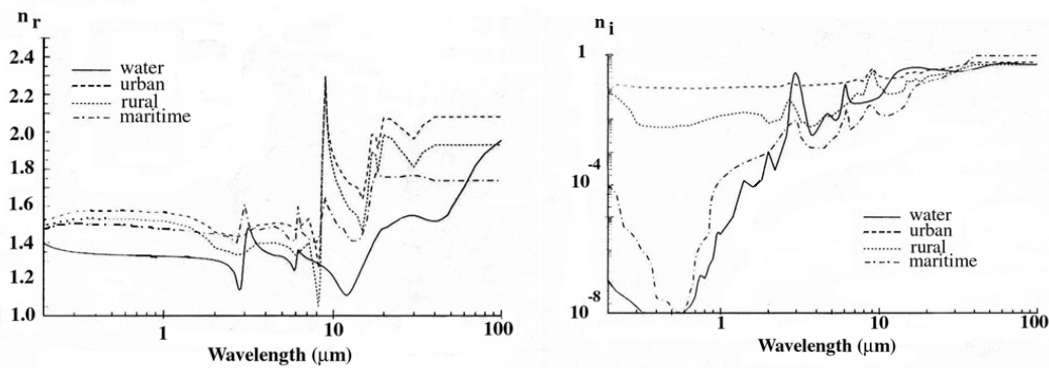


Figure 1.3: Real and imaginary parts of the complex refractive index for different aerosol models (*Shettle and Fenn [1979]*).

Single Scattering Albedo: Aerosol single scattering albedo (SSA or ω_0) is a measure of the effectiveness of scattering relative to extinction for the light

encountering the atmospheric aerosol particles. It is a dimensionless quantity ranging from 0 to 1. As most aerosols are weakly absorbing in mid-visible wavelengths (except for those with large concentrations of organic/black carbon), extinction is primarily by scattering ($\omega_0 > 0.90$ at $0.55 \mu\text{m}$). Black or element carbon (soot) can have $\omega_0 < 0.5$ [Bond and Bergstrom, 2006] especially near sources. Mineral dusts are unique because they are characterized by a spectral dependence of absorption, so that they absorb more strongly in short visible and UV wavelengths ($\lambda < 0.47 \mu\text{m}$) than at longer wavelengths.

Phase Function: Atmospheric particles scatter light in different directions. The aerosol phase function $p(\theta)$, describing the dependence of scattered radiance on scattering angle, is defined as the energy scattered per unit solid angle in a given direction to the average energy in all directions. It is dimensionless and can be normalized as follows (treated as a probability distribution):

$$\frac{1}{4\pi} \int_0^{4\pi} p(\theta) d\omega = 1; \quad (1.11)$$

Where θ is the scattering angle (Figure 1.4), defined as the angle between the forward directions of the incoming light and the scattered light, and $d\omega$ is a differential solid angle in the direction with scattering angle θ . Figure 1.4 represents the angular distribution of the intensity of the light scattered by particles with different size. Clearly, the light scattered in the forward direction by large particles (diameter equals to $1 \mu\text{m}$) is much larger than by the small particles (diameter = $0.01 \mu\text{m}$).

The polarized phase function $q(\theta, r)$ can also be calculated. In the case of molecules (Rayleigh scattering), the phase function is equal to $(3/4)(1 + \cos^2 \theta)$ for total (unpolarized) scattering and $(3/4)(1 - \cos^2 \theta)$ for linearly polarized scattering,

where θ is the scattering angle.

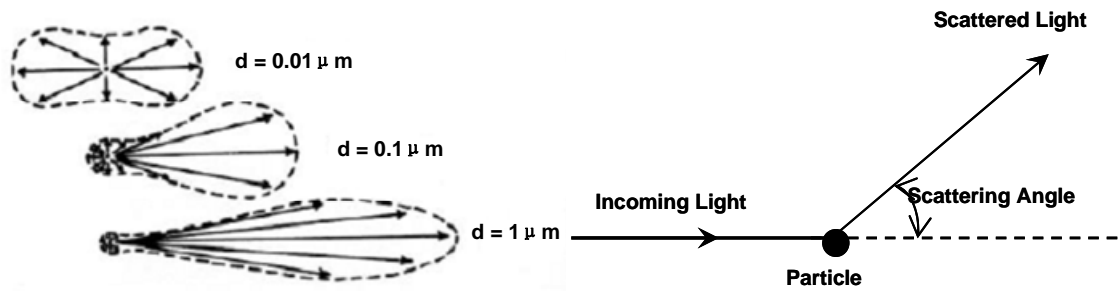


Figure 1.4: Angular distribution of the intensity of the light scattered by particles with different size (diameter = 0.01, 0.1 and 1 μm) and the definition of the scattering angle.

1. 3 Aerosol vertical distribution

Defined as suspension of liquid or solid particles in air, aerosols vertical distribution is strongly influenced by the stability of the atmosphere. The stability of the atmosphere is directly related to the changes of temperature with height. When the atmosphere is stable, an air mass, which is lifted to the air with higher temperature than the air mass, will be denser and tend to fall to its original position.

Depending on the temperature vertical profile, the atmosphere is divided into five layers, including troposphere, stratosphere, mesosphere, thermosphere and exosphere. As the first layer above the surface, troposphere contains more than half of the Earth's atmosphere and almost all of the water vapor, as well as dust particles. Figure 1.5a shows the simplified vertical structure of the troposphere. It extends from the surface to the Tropopause, approximately 11 km above sea level. The bottom of the troposphere, closest to the surface of Earth, is called the "boundary layer" (or planetary boundary layer and atmospheric boundary layer). It's directly influenced by the Earth's surface (frictional drag, evaporation and transpiration, heat transfer, pollutant emission,

etc.) and responds to surface forcing with time scale of about an hour or less. Its thickness ranges from hundreds of meters to a few kilometers depending on the various time and space [Stull, 1988]. Generally, the boundary layer is thinner in high-pressure regions and its structure could be defined better compared to the case with low pressure.

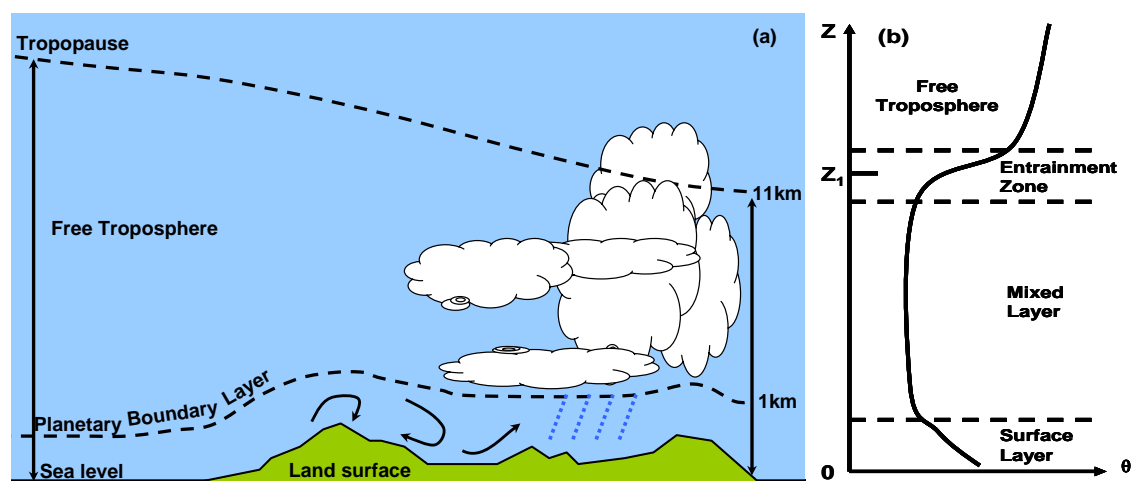


Figure 1.5 (a) Schematic of the vertical structure of the troposphere, consisting of Planetary Boundary Layer (PBL) and Free Troposphere (FT). (b) Typical daytime profiles of mean potential temperature in high-pressure regions [Stull, 1988].

According to the profile of potential temperature during the daytime in high-pressure regions (Figure 1.5b), the vertical structure of the atmospheric boundary layer is observed consisting of three major parts: a surface layer (about 10% of the boundary layer) at its base, followed by the mixed layer and the Entrainment zone. A decrease of a constant value in the surface and mixed layer imply an unstable atmosphere in these two layers. Pollutants emitted at the surface are carried aloft by convective thermals to the top of mixed layer. Above the mixed layer, the stable Entrainment layer (potential temperature increases with height) constrains the pollutants and contributes to the accumulation of aerosol pollutants.

According to Gras [1991], the vertical distribution of aerosol mass concentration usually shows an exponential decrease with altitude above the height of H_a and a low profile or approximately a constant beyond this altitude. The profile of aerosol mass concentration can be expressed as follows:

$$PM(z) = PM(0) \exp^{-z/H_a}; \quad (1.12)$$

Where $PM(0)$ is the mass concentration at the surface. H_a is the height with majority of aerosols defined above. It is observed to equal to 900, 2000 and 730 in the cases of sea salt, desert dust and the continental natural aerosols, respectively [Jaenicke, 1993]. The integration of the mass concentration profile between the ground and an altitude equal to the infinite is simply the product of $PM(0)$ with the scale height H_a :

$$\int_0^{\infty} PM(z) dz = PM(0) \times H_a; \quad (1.13)$$

We should note that the vertical distribution is excessively simplified here with an assumption of the homogeneous mixture of particles in the boundary layer. Obviously, it is often contradicted in the actual case of multiple layers of aerosols in the atmospheric boundary layer or particle transport at high altitudes above this layer.

In short, aerosol vertical distribution is well connected with the variation of the atmosphere profile, especially the vertical structure of boundary layer. An accurate knowledge of the aerosol vertical distribution is required for climate forcing and for air quality, such as the validation of aerosol modeling and satellite aerosol retrievals, and particle-cloud interaction assessment. Consequently, more and more active remote sensing techniques are developed, which will be introduced in the next chapter.

1. 4 Aerosol measurement techniques

Numerous techniques have been developed to observe and quantify aerosol

physical and chemical properties, either in situ or by remote sensing, comprising passive and active methods. The in situ instruments generally measure aerosol properties (aerosol loading, size distribution and chemistry etc.) by perturbing the aerosols collected on their filter or cavity, such as nephelometers and aetholometers. By contrast, remote sensing techniques observe a radiation field as it interacts with the atmosphere and surface, actively by utilizing its own light source or passively by using the ambient radiation as the source. Like in situ techniques, remote sensing includes ground-based (e.g. sunphotometer) and airborne radiometers. Radiometers can also be mounted on orbiting satellites (e.g. MODIS, POLDER) for retrieving continuous information at regional and global scales [Kaufman *et al.*, 1997a; King *et al.*, 1999; Kokhanovsky *et al.*, 2009].

The measurement techniques involved in this thesis are both the in situ technique (e.g. TEOM particulate monitor) measuring aerosol mass concentrations at ground level, and passive remote sensing of aerosols by ground-based instrument (e.g. CIMEL sunphotometer) and space-borne radiometers (e.g. MODIS, POLDER). The corresponding operation principles of instruments and retrieval algorithms are described in Chapter 2. In order to make the descriptions hereinafter readily comprehended, we introduce some basis about the geometry of satellite remote sensing and radiative transfer, which are very important in the aerosol remote sensing and retrieval.

Radiative Transfer: The equation of radiative transfer is established to describe the interaction of sunlight with various components of the atmosphere (a set of aerosol assumed to be spherical and molecules) and the Earth's surface [Lenoble, 1993]. Modern satellite retrievals of aerosol properties are based on the LUTs (Look Up Tables), which are calculated using radiative transfer codes [Rozanov and Kokhanovsk, 2006] for different observation geometries and aerosol phase

functions, dependent on the scattering angle, single scattering albedo and AODs.

The sunlight, which is naturally unpolarized, becomes polarized due to the interactions with the components of the atmosphere or land surface. The electromagnetic radiation can be defined in two ways:

1) By the four Stokes parameters [*Chandrasekhar, 1950; Van De Hulst, 1957*], I , Q , U and V . I is associated with the total intensity of the beam, while the other three parameters characterize the polarization state of radiation. Therefore, the solar radiation is characterized only by I . Note that the parameter V is associated with the ellipticity of the radiation [*Deuzé, 1974*], and will be considered to be invalid because the polarization of solar radiation, after interaction with the atmosphere and the surface, is linearly [*Kawata, 1978*].

2) By its spectral reflectance L ($\text{W}\cdot\text{M}^{-2}\cdot\text{sr}^{-1}\cdot\mu\text{m}^{-1}$), the energy flux emitted or reflected per unit area and unit solid angle depending on the wavelength. The total reflectance L_t is equal to the Stokes parameter I , and the polarized reflectance L_p is equal to $\varepsilon\sqrt{(Q^2 + U^2)}$, where ε is the sign (± 1) of the polarized reflectance. The parameter ε is equal to 1 when the electric field is polarized in the perpendicular direction of scattering plane, and equals to -1 when the electric field is polarized in the direction of the scattering plan.

Using a radiative transfer code, the electromagnetic radiation received by the instrument (L_{inst}), the contribution of radiative aerosols (L_{aer}), the Earth's surface (L_{surf}) and molecules (L_{mol}) can be calculated and:

$$L_{inst} = L_{aer} + L_{mol} + L_{surf}; \quad (1.14)$$

Neglecting the coupling terms between aerosols, molecules and the surface in

Equation 1.14, the contribution of only the particles (L_{aer}) can be approximately for the optically thin layers (e.g., $\tau \leq 0.01$) as follows:

$$L_{aer} = \frac{\omega_0 \times \tau_{ext} \times P(\Theta)}{4\mu_v}; \quad (1.15)$$

Where ω_0 is the single scattering albedo, $P(\Theta)$ is the normalized aerosol phase function for the scattering angle Θ , and μ_v is the cosine of the zenith viewing angle (Figure 1.4).

The contribution of molecules is well known and can be easily modeled. Thanks to profiles of known pressure and temperature, it is indeed possible to calculate the optical thickness of molecular (through the so-called Rayleigh scattering) and to derive molecular reflectance (L_{mol}) by radiative transfer.

The radiative contribution from the surface (L_{surf}) can be a major component of signal received by the instrument. The choice of conditions of observation (spectrum) requires very different techniques over the oceans and continents. Above oceans, the near-infrared supports the measurement of aerosols because the ocean there hardly reflects solar radiation ($L_{surf} = 0$).

In this thesis, we focus on the observation of the aerosols over land, which is more complex because the radiation reflected by the surface and backscattered by aerosols are difficult to distinguish. Indeed, in the spectrum visible over the continents, strong surface contribution to the total reflectance (as a case of highly reflective surface, desert) hinders the aerosol measurements.

Thus, retrieval algorithms of aerosols over land from satellite observations generally use different approaches, either in the ultraviolet spectral band [*Herman et al.*

1997a] or the thermal infrared band [Legrand *et al.*, 1989] over desert surfaces, or by measuring the polarization of reflected light [Deuzé *et al.*, 1993; Herman and *al.*, 1997b] for other types of land surfaces. This issue will be introduced more detailed in the next chapter.

Satellite remote sensing geometry Unlike the ground-based instruments, which derive aerosol optical properties from measurements of extinction or sky light scattering in the downward direction, satellite derived aerosols properties from measurements of up-scattered (reflected) radiation (e.g., [Kaufman *et al.*, 1997a]). The geometry of the satellite measurement is illustrated in Figure 1.6, such that θ_s , θ_v , and ϕ are the solar zenith angle, the zenith viewing angle and the relative azimuth angle, respectively. Θ is the scattering angle.

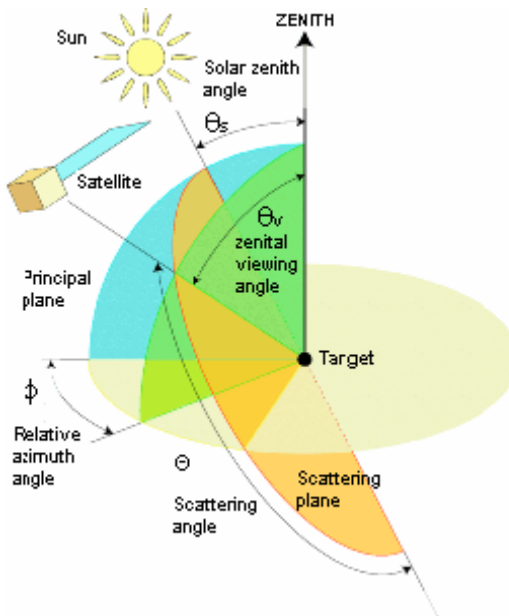


Figure 1.6: Schematic of satellite remote sensing geometry.

1. 5 Impacts of atmospheric aerosols

Atmospheric aerosols, ubiquitous particles suspended in the atmosphere, play an

important role in the climate system. They affect the Earth’s radiative budget both directly by scattering and absorbing solar radiation and indirectly by modifying properties of clouds such as their albedo and lifetime [Forster et al., 2007]. The effects of aerosols are thought to partially counterbalance global warming caused by greenhouse gases [Charlson et al., 1992; Forster et al., 2007]. Furthermore, tropospheric aerosols, especially aerosols close to the Earth’s surface, greatly influence air quality and thereby affect both the environment and human health.

1. 5. 1 Effects on the radiation and climate

Radiative forcing is a change in net radiative flux at the tropopause after the stratosphere comes back into equilibrium (official IPCC definition). It is the term used to describe changes imposed on the planetary radiation balance caused by the impact of external factors in the climate system and measured in Watts per square meter (Wm^{-2}). Radiative forcing can be considered to be warming or cooling corresponding to their positive or negative values.

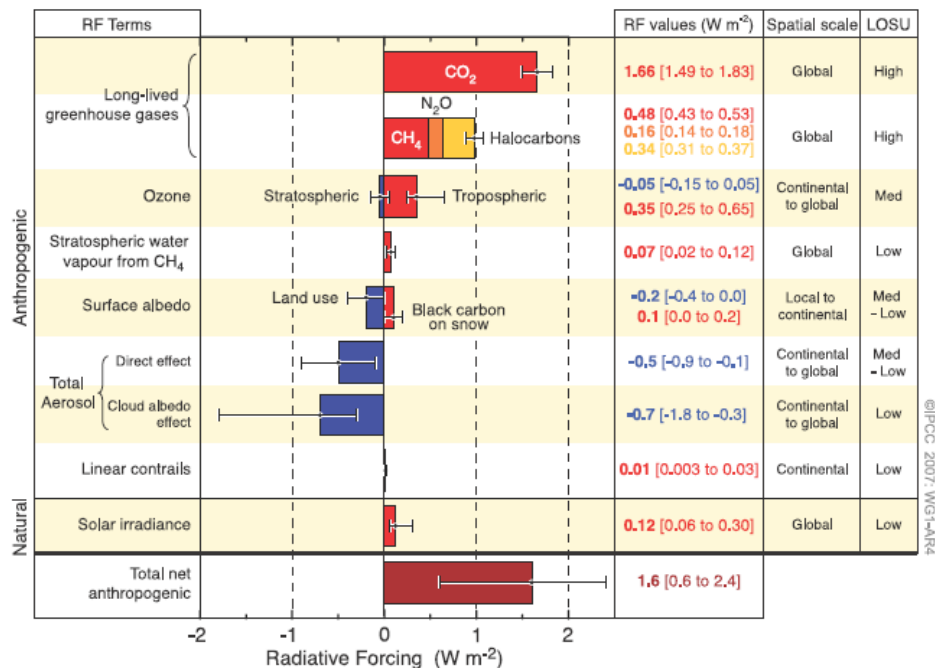


Figure 1.7: *Assessment of global average radiative forcing (RF) by the different atmospheric components in 2005 [Forster et al., 2007].*

Natural as well as anthropogenic aerosols affect the global radiation balance directly and indirectly. As a direct effect, the aerosols scatter and absorb the incoming solar (shortwave) and outgoing (long wave, IR) radiation, and then affect the planetary albedo and surface radiative fluxes [Haywood and Ramaswamy, 1998; Jacobson, 2000]. As an indirect effect, aerosols in the lower atmosphere can modify the radiative properties, the number and size of cloud droplets [Kaufman et al., 2002], and then the precipitation efficiency [Poschl, 2002]. Additionally, the effects of aerosols on temperature vertical profile and consequently on the formation and cloud types have been considered as a semi direct effect [Hansen et al., 1997; Ackerman et al., 2000]. IPCC's fourth assessment report included a significant discussion on the radiative forcing due to atmospheric aerosols. It represents the sign and intensity of the radiative forcing resulting from these direct and indirect effects of aerosols (Figure 1.7) [Forster et al., 2007]. The radiative forcing driven by the total anthropogenic emissions (including greenhouse gases and aerosols) is shown to be positive to 1.6 Wm^{-2} (from 0.6 to 2.4 Wm^{-2}), indicating the likely a warming impact of human activities. However, focusing on the effects of total aerosols in Figure 1.7, we observed the negative radiative forcing (blue, cooling the Earth-atmosphere system) due to the direct ($-0.5 \pm 0.4 \text{ Wm}^{-2}$) and indirect effects (-0.7 Wm^{-2}) of aerosols. Indeed, the presence of weakly absorbing aerosol layers tend to contribute to global cooling over the surfaces with low reflectance (oceans or forests). Note that the estimate of the total direct effects of aerosols is now more accurate [Forster et al., 2007] than before [Ramaswamy et al., 2001] because it relies on a combination of model simulations and observations. But, much larger uncertainties remain in aerosols radiative forcing estimates, especially in the indirect effects, compared to the other atmospheric components.

Besides the radiative effects indicated above, other climate impacts are caused by aerosols, are shown in recent studies. For example, aerosol particles are found to be able to reduce near-surface wind speeds by stabilizing the air, reducing the vertical transport of horizontal momentum [*Jacobson and Kaufman, 2006*]. Furthermore, man-made aerosols have the capability of dimming the surface of the planet while making it brighter at the top of the atmosphere [*Ramanathan and Feng, 2009*].

1. 5. 2 Effects on human health and environment

Aerosols also contribute to atmospheric pollution, with substantial impacts on human health and visibility. Atmospheric particles inhaled through the respiratory tract may damage health. Relatively large particles are likely to be retained in the nasal cavity and in the pharynx, whereas very small particles can reach the lungs and be retained by them. These small particles, mostly from combustion processes, may contain toxic metals and organic pollutants [*Manahan, 1993*]. Aerosol pollutants, which decrease air quality, always cause some public health problems [*Tie et al., 2009*]. Amounts of studies prove that there are associations between long-term (and short-term) exposure to ambient particulates and elevated cases of cardiovascular problems, respiratory morbidity, and mortality, particularly for infants and elderly people [*Ibald-Mulli et al., 2002; Hauck et al., 2004; Schulz et al., 2005; Murr and Garza, 2009; Tie et al., 2009*].

Another obvious effect of aerosols on air quality is reduction of visibility because human psychology and physiology are sensitive to visual input. Visibility refers to the clarity or transparency of the atmosphere and the associated ability to see distant objects. In the condition of moderate or high aerosol loading, radiation scattering by particles is the primary limitation to visibility. Particles, which are in the anthropogenic (accumulation) mode particles, are a principal factor in producing

brownish smoggy air throughout the world.

1. 6 Motivations and outline of the thesis

Considering the above description, we obtain more understanding on aerosols properties and recognize clearly their importance for a wide range of geophysical and environmental problems, ranging from local issues (e.g., human health) to global scale (e.g., climate change). However, the large temporal and spatial variability of aerosol loads, as well as the variability of their physical properties make the estimation of their impacts a challenging task. The lack of data characterizing the optical and physical properties of aerosols remains a primary source of uncertainty in quantifying both their climatological and environment effects [*Kaufman et al.*, 2002].

Motivated by climate change and adverse health effects of traffic-related air pollution, aerosol research has increasingly intensified over the past couple of decades. Numerous passive and active techniques have been developed to observe and quantify aerosol physical and chemical properties, either in situ or by remote sensing [*King et al.*, 1999; *Lee et al.*, 2009]. POLDER [*Deschamps et al.*, 1994], the first generation of large-field of view polarimeter aboard the ADEOS-1 satellite in 1996, led us to a new era of the remote sensing of tropospheric aerosols from space [*King et al.*, 1999]. It is designed to collect accurate observations of the polarized and directional solar radiation reflected by the Earth-atmosphere system and demonstrates its unique advantages compared to either the traditional ground-based instrument or the other space-borne radiometers. As one kind of the space-borne sensors, POLDER provides daily global coverage thanks to its large field of view, which can not be performed by the ground-based instruments. Moreover, while most other satellite sensors have difficulties in deriving aerosol properties over land because of the high surface reflectivity and spatial variability, POLDER effectively overcomes the unknown

surface contamination through the use of polarization information primarily due to atmospheric scattering processes [Deuzé *et al.*, 2001].

The aim of this study was to provide a comprehensive characterization of aerosols over East Asia based on more than six years of POLDER-3 retrievals over the land surface, with ancillary dataset such as AERONET measurements and inversions, MODIS level 2 aerosol products, CALIOP/CALIPSO level 2 aerosol products, and PM concentrations measured at ground.

After introducing the data collection used in this thesis in chapter 2, we compared POLDER-3 AOD against AERONET recomputed fine mode AOD with cut-off radius of 0.30 μm over 14 sites located in this large area (chapter 3), in order to evaluate the quality of POLDER aerosol retrievals. The good consistency (correlation coefficient above 0.9) between the totally independent retrievals shows the POLDER capability to measure the optical depth of anthropogenic aerosols and more generally the optical depth of the smallest aerosols ($r \leq 0.30 \mu\text{m}$). Based on assurance of the quality of POLDER aerosol retrievals over land, we analyzed the characteristics and seasonal variations of aerosol distribution over East Asia using POLDER-3 aerosol retrievals over a 4-year period (March 2005-February 2009) in chapter 4. Then, considering all of the data available from POLDER-2 and 3, we analyzed summer AOD in the Northern China region, especially the inter-annual evolution of summer aerosol content in Beijing City in the context of August 2008 Olympic Games. These results have been published recently in *Su et al.* [2010]. Combined with aerosol retrievals with high accuracy from MODIS/Aqua due to its sufficient spectral diversity, POLDER has extended capability to characterizing coarse aerosol loads and depicts the distribution patterns of coarse mode aerosols (or fine mode fraction) over East Asia and their seasonal variability in chapter 5. In chapter 6, we discussed the possibility to assess the air quality with statistical method using POLDER derived AOD and the factors that

affect the correlation between satellite derived AOD and $PM_{2.5}$. Some preliminary analyses are performed focusing on the diurnal variation of $PM_{2.5}$ and the vertical distribution of aerosols. Finally, chapter 7 gives the general conclusions of this thesis and presents recommendations for future work.

Chapter 2 Data Collection Descriptions

The purpose of this thesis is to explore aerosol characteristics over East Asia from POLDER observations based on the regional validation of POLDER-3/PARASOL aerosol retrievals over land. Our primary area of interest in this work, East Asia, is a region considered to be one of the world's major sources of both natural and anthropogenic aerosols. It is defined as the area with latitude ranging from 10 ° N to 55 ° N and longitude ranging from 70 ° E to 140 ° E in this study. Our approach mainly comprises four parts as follows: (1) evaluation of POLDER-3 continent aerosol products with AERONET/PHOTONS inversions from 14 sites located in East Asia, (2) analyses of aerosol variability over East Asia using POLDER aerosol retrievals validated in the first part, (3) further study on aerosol characteristics by the combination of POLDER and MODIS/AQUA observations, and (4) preliminary discussion on the potential of POLDER in monitoring aerosol pollution in terms of particulate mass concentration at ground level. For the evaluation of POLDER-3 AOD, we use a dataset covering the period between March 2005 and June 2008, while in the second and third parts of thesis, we consider POLDER-3 and MODIS/AQUA Level 2 AOD from March 2005 to March 2009. Moreover, Level 2 aerosol layer products of space-borne lidar CALIOP/CALIPSO are also included in the last part of our work. In order to broaden our database for the purpose of year-by-year evolution analysis during the summertime, we also include data from POLDER-2 in our work. In this chapter, all the aerosol measurements from ground-based instruments and space-borne sensors used in the thesis are introduced.

2. 1 AERONET/PHOTONS measurements and inversions

The Aerosol Robotic Network (AERONET) [Holben *et al.*, 1998] program is a

federation of ground-based remote sensing aerosol instruments established by NASA with contribution of PHOTONS, the French component of the program (based in LOA). Today it consists of more than 400 permanent and temporary sites in 50 countries located over all the seven continents. Figure 2.1 shows the locations of AERONET sites world-wide in June 2009 (indicated by red squares). The purpose of AERONET program is to provide long-term, continuous measurements of aerosol optical, microphysical and radiative properties for aerosol research as well as validation of satellite retrievals and models [Holben *et al.*, 1998; 2001].

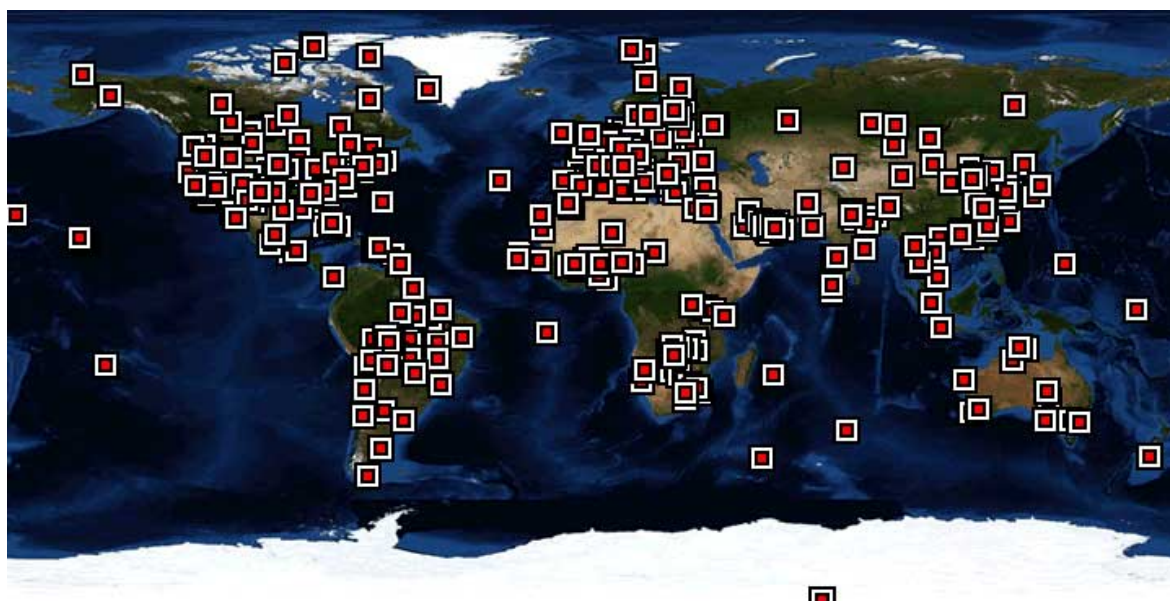


Figure 2.1: Locations of AERONET sites in June 2009 indicated by red squares (from <http://aeronet.gsfc.nasa.gov/>).

2. 1. 1 Automatic sun and sky scanning spectral radiometer

The instrument used in AERONET program is a CIMEL CE 318 automatic sun/sky radiometer (Figure 2.2-left) manufactured in Paris, France. It is a solar-powered, weather-hardy, robotically-pointed sun and sky spectral radiometer.

This modern instrument incorporates technological advances in optics and electronics and is generally more sensitive and more stable, compared to the previous sun-photometers developed during the early part of the 20th century. It is composed of three parts:

- An optical head: contains two detectors (sky-sun) with their separate collimators having the same field of view (1.2°), a control and measurements card, a four quadrant position detector (for a precise tracking of the sun), a motorized filter holder wheel with eight filters and a temperature sensor. It is pointed by stepping azimuth and zenith motors with a precision of 0.05 degrees.
- A two axis motorized system: a robot carrying the optical head, which is moved by step-by-step motors in two directions (in the zenith and azimuth planes).
- A control and measuring unit (the electronic box): contains two microprocessors for real time operation for data acquisition and motion control.

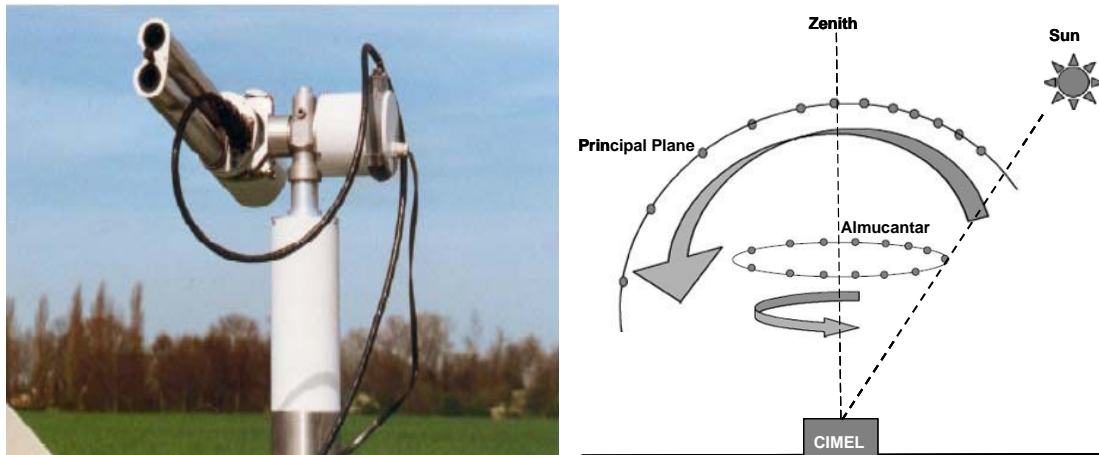


Figure 2.2: CIMEL CE 318 Sun-photometer (left) used in AERONET program and its basic sky observation sequences (right).

The radiometer makes two basic measurements, either direct Sun or sky, both within several programmed sequences. The direct Sun measurements are made in eight spectral bands (anywhere between 340 nm and 1020 nm; 380 nm, 440 nm, 500 nm, 670 nm, 870 nm, 940 nm, and 1020 nm are standard), while sky measurements are performed at 440 nm, 670 nm, 870 nm, and 1020 nm with two basic sequences, the “almucantar” and “principal plane”. As it is shown in Figure 2.2-right, the almucantar sky radiance is obtained by scanning the sky at the solar zenith angle with different azimuth angles to obtain the angular variation of skylight in four filters. Solar principal plane sky measurement is obtained by scanning in a plane containing the sun and the instrument and normal to the surface. Besides, as an option with this instrument, polarized solar principal plane sky radiance is taken at 870 nm immediately after the standard principal plane measurement sequence [Holben *et al.*, 1998]. Table 2.1 summarized the instrument characteristics and observational specifications.

Table 2.1 Instrument characteristics and observational specifications
(from http://www.cimel.fr/photo/sunph_us.htm).

	Spectral range (nm)	Target	Number of observations	Interval between observations
BASIC DIRECT SUN	340 to 1020	Sun	1 per filter	~8s between 2 obs. with the same filter
Triplet observation	340 to 1020	Sun	3 times the basic direct sun every 30s	~10s for 3 consecutive obs and 30s apart
Standard measurement	340 to 1020	Sun	Variable	Every 15 mn between m=2am and m=2pm
Langley	340 to 1020	Sun	17	m=2 to 5 every 0.25 m=5 to 7 every 0.5
BASIC SKY	440 to 1020	Sky	1 per filter	none
Langley sky	440 to 1020	Sky	17	m=2 to 5 every 0.25 m=5 to 7 every 0.5
Almucantar	440 to 1020	Sky	72	m=4, 3, 2, 1.7 then hourly between 9am and 3pm
Polarization	870	Sky	42	hourly between m=3am and m=3pm
Principal plane	440 to 1020	Sky	42	hourly between m=3am and m=3pm

Measurement sequences of the CIMEL sun/sky scanning spectral radiometer (m: air mass)

2. 1. 2 AERONET direct measurements and aerosol inversions

Sun-photometer CIMEL CE-318 makes measurements of the direct Sun and diffuse sky spectral radiances to retrieve aerosol optical properties. All the AERONET data and inversions are available on the website: <http://aeronet.gsfc.nasa.gov/> .

1) Direct Sun Measurements

Sun photometer measures the direct solar radiation every 15 minutes at a number of fixed wavelengths within the visible and near-infrared spectrum and provides information to calculate the columnar aerosol optical depth (AOD), which can be used to compute total column precipitable water (using 940 nm channel), Angström exponent, fine and coarse AOD and fraction, as well as some statistics such as daily averages and monthly averages.

To retrieve the aerosol column optical depth of the atmosphere, the inversion of the direct sun measured by the sun-photometer is based on the Beer-Lambert-Bouguer law:

$$E_{\lambda} = E_{0,\lambda} R^{-2} \exp(-m \tau_{\lambda}) T_{g,\lambda} \quad (2.1)$$

Where E_{λ} is the solar irradiance at the ground level, $E_{0,\lambda}$ is the extra-terrestrial solar irradiance at a distance of one Astronomical Unit (AU), R is the actual Sun-Earth distance coefficient in AU at the time of measurement [Michalsky, 1998], m is the optical air mass, which is approximated by the revised formula provided in *Kasten and Young* [1989]; $T_{g,\lambda}$ is the transmission of absorbing gases (the ozone and water vapor absorption at 675 nm and 870 nm); τ_{λ} is the total vertical optical depth. If the instrument voltage is V for irradiance E , the above equation can be written as:

$$V_{\lambda} = V_{0,\lambda} R^{-2} \exp(-m\tau_{\lambda}) T_{g,\lambda} \quad (2.2)$$

Where $V_{0,\lambda}$ on the right hand side of this equation is the calibration coefficient obtained by measuring voltage V_{λ} as a function of air mass m and extrapolating the resulting curve to zero air mass. τ_{λ} could also be determined by the Langley plot [Langley, 1881; O'Neill and Miller, 1984], which is a log of V_{λ} against the optical air mass m between the range of 2 and 5 during the day that aerosol and irradiance is stable.

The total optical depth (τ_{λ}) is made up of molecular (Rayleigh) scattering, trace gas absorption (such as ozone), and aerosol extinction. Each of these components can be separated. The Rayleigh component is readily calculated, depending only on the Rayleigh equation suggested by Bodhaine *et al.* [1999]. By appropriately making different assumptions depending on wavelength (λ) to neglect or estimate other components, the contribution of aerosols (aerosol optical depth) could be isolated and estimated. Additionally, the cloud-screening procedure [Smirnov *et al.*, 2000] needed to be performed before retrieving AOD from the direct sun measurements.

The extraction of water vapor amount from sun-photometer measurements generally relies on a measurement in the region of water vapor absorption at 940 nm. Transmission in the water vapor band (T_w) can be modeled as [Halthore *et al.*, 1997; Smirnov *et al.*, 2004]:

$$T_w = \exp(-aW^b) \quad (2.3)$$

Where W is vertical column abundance, equaling to the air mass, m , multiplied by the precipitable water (PW), which can be calculated by a modified Langley method;

constants a and b are unique to the particular filter.

The aerosol optical depth at relevant wavelengths can be derived from the measurements in several channels of the photometer and used to derive the Angström exponent, which is related to the aerosol size distribution [*Junge*, 1963]:

$$\tau_a(\lambda) = k\lambda^{-\alpha} \quad (2.4)$$

Where λ is the wavelength; $\tau_a(\lambda)$ is aerosol optical depth at λ ; k is Angström turbidity coefficient and α is Angström wavelength exponent.

2) Diffuse Sky Radiance

In addition to the direct “sun” measurements, The CIMEL sun-photometers are programmed to observe angular distribution of sky radiance, approximately every hour during the daytime. These “sky” measurements are made at discrete azimuth angles along sun’s “almucantar” or at discrete zenith angles along sun’s “principle plane” (illustrated in Figure 2.2-*right*), at least at four wavelengths (440 nm, 670 nm, 870 nm and 1020 nm) in order to observe aerosol spectral scattering. The use of the almucantar sky radiance scans in conjunction with the aerosol optical depth are the basis of the AERONET *Dubovik* retrievals, which provide the aerosol volume size distribution over a wide range of sizes (0.05–15 μm), aerosol complex refractive index, single scattering albedo and the aerosol scattering phase function. These aerosol properties are retrieved via an inversion algorithm developed by *Dubovik and King* [2000]. The accuracy of the *Dubovik* retrievals has been assessed with the retrieval of synthetic data in *Dubovik et al.* [2000]. Moreover, *Dubovik et al.* [2006] developed further algorithms to take into account non-spherical shapes of aerosol particles such as mineral dust.

By assuming the ambient aerosol to be an homogenous ensemble of polydisperse spheres and randomly oriented spheroids [Dubovik *et al.* 2006], the algorithm retrieves the volume distribution ($dV/d\ln r$) for 22 radius size bins and spectral complex refractive index (at wavelengths of sky radiance observations) that correspond to the best fit of both sun-measured AOD and almucantar sky radiance. The non-spherical fraction is modeled with distribution of aspect ratios retrieved by Dubovik *et al.* [2006] that fit scattering matrices of mineral dust measured in the laboratory [Volten *et al.*, 2001]. In either case, the modeling is performed using kernel Look-Up Table (LUTs) of quadrature coefficients employed in the numerical integration of spheroid optical properties over size and shape.

Retrievals from both sun and sky AERONET measurements are controlled by rigorous calibration and cloud-screening processes. In this thesis, we principally consider AERONET total Aerosol Optical Depth (AOD) and AOD of fine mode with cut-off radius $0.30\ \mu\text{m}$ computed using the aerosol size distributions and the refractive index based on Mie Theory. The accuracy of the aerosol optical depth is approximately 0.01–0.02 for field operated Cimels. Aerosol size distribution ($dV/d\ln r$) has an accuracy of 15% for the range of sizes, $0.1\ \mu\text{m}$ – $7\ \mu\text{m}$ [Dubovik *et al.*, 2000]. In the AERONET database, three different levels of data are available. The first level, termed Level 1.0, is available in real time. Level 1.0 data includes possible cloud contamination; however, in contrast, cloud contamination is automatically filtered from the second level of data, termed Level 1.5. For the third level of data, Level 2.0, data are cloud-screened and quality-assured and include final post-deployment calibrations. In order to obtain the largest amount of available ground-based data collocated by satellite retrievals, we use Level 1.5 AERONET AOD and inversions products for the evaluation of POLDER-3 (chapter 3) and MODIS (chapter 5) retrievals. When we performed this evaluation phase, we needed an as dense as

possible aerosol record. For many sites, level 2 data were not available, and in order to get the most recent AERONET data records, we had to use level 1.5 AOD and inversions products. Nevertheless, to keep the best quality data we applied additional filters on the data, explained in both third and fifth chapters.

2. 2 Satellite aerosol retrievals

Satellite aerosol products considered in this thesis consist of level 2.0 aerosol products over both land and ocean from POLDER (POLDER-2/ADEOS-2, POLDER-3/PARASOL) and MODIS/AQUA, and CALIOP/CALIPSO level 2 aerosol layer products. Although the orbit of PARASOL has been lowered since December 2009 due to insufficient fuel supplies, it flew in the “A-Train” formation during our study period (March 2005 to March 2009), as well as AQUA satellite. Simultaneous measurements from these two satellites flying in the same orbit imply a possibility to acquire more knowledge about aerosols by combining aerosol retrievals from POLDER-3/PARASOL and MODIS/AQUA.

2. 2. 1 The “A-Train” Constellation

The Afternoon Train, or “A-Train”, for short, is a constellation of satellites that travel one behind other, along the same track. Four satellites currently fly in the A-Train – Aqua, Cloudsat, CALIPSO, and Aura. Recently Glory failed during its launch (March 2011), although GCOM-W1, and OCO-2 are scheduled to join the configuration in 2012, and 2013, respectively. In December 2009, PARASOL began to leave the formation and it will exit completely by 2012, although it was part of the A-Train during more than 4 years (*Figure 2.3*). The satellites cross the equator within a few minutes of each other at around 13h30 (local time). By combining different sets of nearly simultaneous observations from these satellites sensors, our ability to study

important aerosol parameters related to climate change and air pollution should strongly progress. In this thesis, we use aerosol retrievals from POLDER (aboard PARASOL), MODIS (aboard AQUA) and CALIOP (onboard CALIPSO).

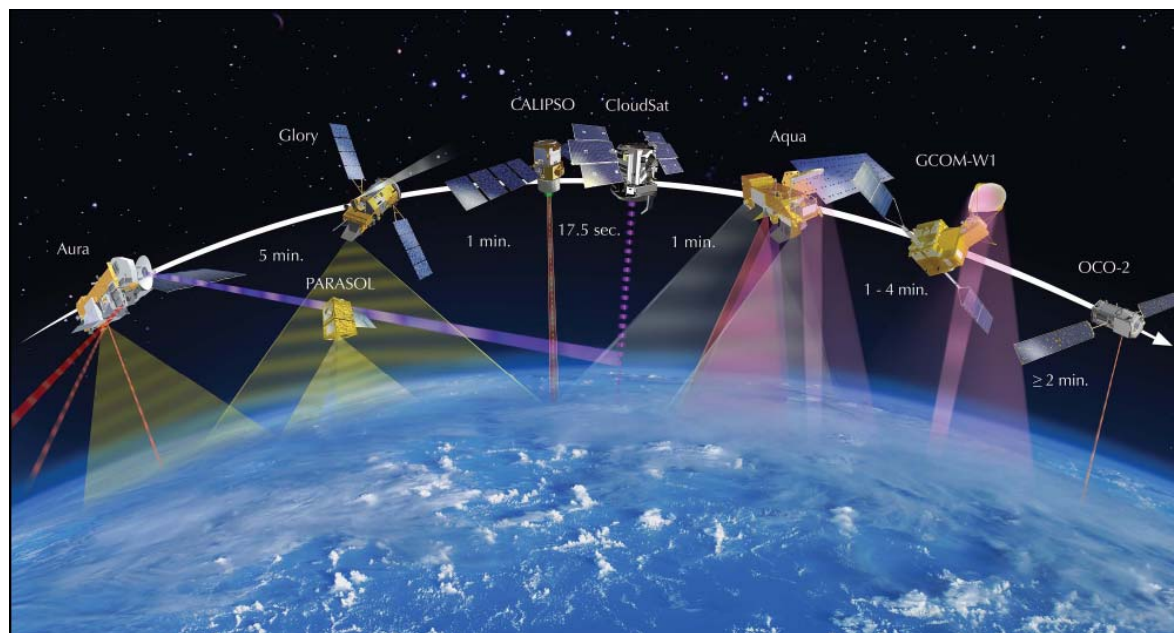


Figure 2.3: *The Afternoon “A-Train” Constellation comprising OCO-2, GCOM-W1, Aqua, CloudSat, CALIPSO, Glory, and Aura. Before December 2009, PARASOL was also one member of this constellation, flying in the same orbit of 705 km with other members of A-Train Constellation.*

Aqua, the leader spacecraft in the A-Train formation until the launch of GCOM-W1 and OCO-2, was launched on May 4th, 2002. It is named for the large amount information (water in the Earth system) and has six different Earth-observing instruments on board. This satellite ascends across the equator at the same local time every day, approximately 1:30 p.m. Correspondingly, on the other side of its orbit, Aqua descends across the equator at approximately 1:30 a.m. We will particularly introduce one of its instruments – MODIS hereinafter in this chapter.

PARASOL (Polarization & Anisotropy of Reflectances for Atmospheric Sciences

coupled with Observations from a Lidar), was launched in December 2004 as the third member of the A-Train Constellation and started its operational life at the early beginning of March 2005. The instrument aboard this satellite is the third POLDER (Polarization and Directionality of the Earth's Reflectances), which has been developed by CNES to improve our knowledge of the radiative and microphysical properties of clouds and aerosols by measuring the directionality and polarization of light reflected by the Earth-atmosphere system. Originally designed to be a 2-year mission, PARASOL flew within about 30 seconds of other members of A-Train Constellation, CALIPSO and Cloudsat satellites. However, the PARASOL satellite was moved to a lower orbit (3.9 km beneath) in early December 2009 in order to minimize the risk of collision caused by the insufficient fuel supplies. On the new orbit, observations from PARASOL will no longer be simultaneous with the other A-Train sensors, except for only a few days at regular intervals. Nevertheless, in this thesis we focus our study on the period before March 2009, when PARASOL still flew on the A-Train orbit. Consequently, we analyze aerosol characterization over East Asia by combining simultaneous observations from POLDER-3/PARASOL and MODIS/Aqua in the fifth chapter.

CALIPSO (Cloud-Aerosol Lidar and Infrared Pathfinder Satellite Observation) was launched on 28, April 2006 with an equator-crossing time of about 1:30 p.m. and 1:30 A.M., and a 16-day repeating cycle. Three instruments are on board this mini satellite, including CALIOP (Cloud-Aerosol Lidar with Orthogonal Polarization), IIR (an imaging infrared Radiometer) and WFC (the wide Field Camera). CALIOP is a two-wavelength (532 and 1064 nm) polarization-sensitive LIDAR which provides vertical profiles of aerosols and clouds with high resolution. The vertical distribution of aerosols and thin clouds properties bring new information essential for the study of interactions between cloud, aerosol and radiation.

2. 2. 2 Description of POLDER-2/-3 and MODIS radiometers

The POLDER instrument [*Deschamps et al.*, 1994] has been developed by the Atmospheric Optics Laboratory (LOA) in Lille. As the first generation of large-field of view polarimeter, POLDER (Polarization and Directionality of Earth's Reflectances) sensors have flown on three different platforms. First, POLDER-1 was flown aboard the Japanese ADEOS-1 (Advanced Earth Observation Satellite) platform in operation from November 1996, to June 1997. Subsequently, POLDER-2 was flown aboard ADEOS-2 from April to October 2003. Finally, in December 2004, the third instrument, POLDER-3, was carried on the French microsatellite PARASOL, which was part of the A-Train up to the spring of 2010, and started routine observations in March 2005. POLDER has provided the first global, systematic measurements of spectral, directional and polarized characteristics of the solar radiation reflected by Earth-atmosphere system. Its original observation capabilities have opened up new perspectives of discriminating the radiation scattered in the atmosphere from the radiation actually reflected by the surface.

MODIS (or Moderate Resolution Imaging Spectroradiometer) is a key instrument aboard the Terra (EOS AM) and Aqua (EOS PM) satellites [*Salomonson et al.*, 1989]. Aqua MODIS, the sensor considered in this thesis, is viewing the entire Earth's surface every 1 to 2 days, acquiring data in 36 spectral bands, or groups of wavelengths. These data will improve our understanding of global dynamics and processes occurring on the land, in the oceans, and in the lower atmosphere. MODIS is playing a vital role in the development of validated, global, interactive Earth system models, which are able to predict global change accurately enough to assist policy makers in making sound decisions concerning the protection of our environment.

The characteristics of these two different instruments POLDER (aboard ADEOS-2

and PARASOL) and MODIS (aboard AQUA) are briefly summarized in *Table 2.2*.

The POLDER instrument (POLDER-2/-3) is a camera composed of a CCD matrix detector, a wide field of view (FOV) telecentric optics and a rotating wheel carrying 15 spectral and polarized filters which allow obtaining images in several wavelengths and according to several directions of polarization. The dimension of the POLDER-2 CCD detector array (242×274detectors) provides a moderate spatial resolution (6 km) and a multi-angle viewing capability. When the satellite carrying POLDER instrument passes over a target, about 12 (up to 14) directional radiance measurements (for each spectral band) are performed successively aiming at the same point (Figure 2.4). Every day, satellite tracks are shifted so that the target is viewed under different angles. The Bidirectional Reflectance Distribution Function (BRDF) and the Bidirectional Polarization Reflectance Distribution Function (BPDF) of the targets are thus measured by POLDER with a single comprehensive sampling. For POLDER-3/PARASOL, the wider dimension of the CCD detector array allows higher spatial resolution and more directional radiance measurements (up to 16) obtained on a single orbit pass.

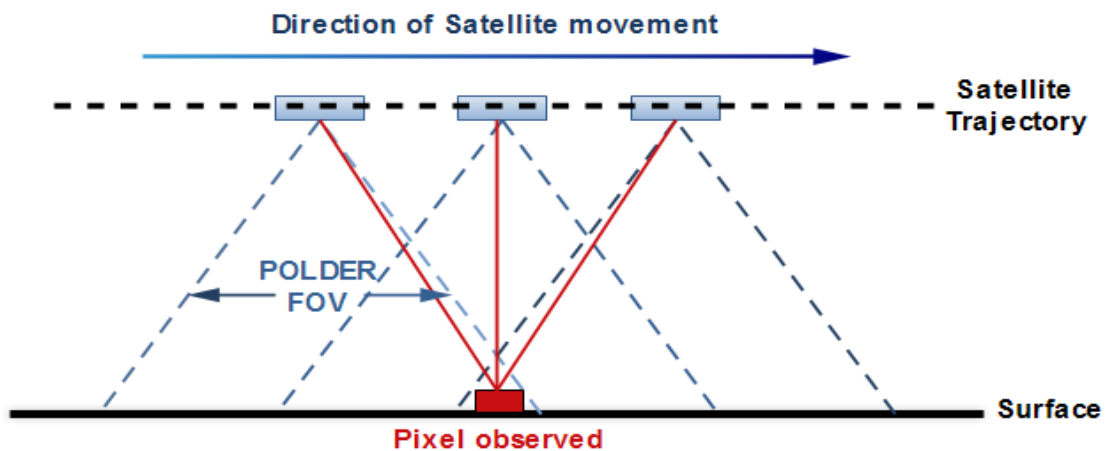


Figure 2.4: *The scheme of POLDER Multi-angular observation.*

The rotating wheel, another component of the POLDER instrument, supports the interference filters and polarizers that select the spectral bands and polarization directions. It carries 16 slots, one of which is an opaque filter to estimate the CCD detector dark current. The remaining 15 slots carry 6 un-polarized and 9 polarized filters (3 polarization directions for 3 different wavelengths) [Deschamps *et al.*, 1994]. However, some improvements are shown by POLDER-3, compared to POLDER-2. POLDER-3 instrument covers a spectral domain ranging from 443 to 1020 nm, while POLDER-2 covers the range of 443-910 nm. Likewise, a 2010-nm waveband has been added, replacing POLDER-2 490-nm band, to conduct observations for comparison with data acquired by Lidar on CALIPSO (1064 nm). Additionally, the POLDER-2 443 polarized band was also replaced by the 490 polarized band of POLDER-3 in order to reduce the impacts of atmospheric molecular scattering. Moreover, the telecentric optics array of POLDER-3/PARASOL has been turned 90 degrees to favour multidirectional viewing over daily coverage. The spectral bands, as well as their characteristics, used in POLDER-2 and POLDER-3 are illustrated in *Figure 2.5*, contrastively.

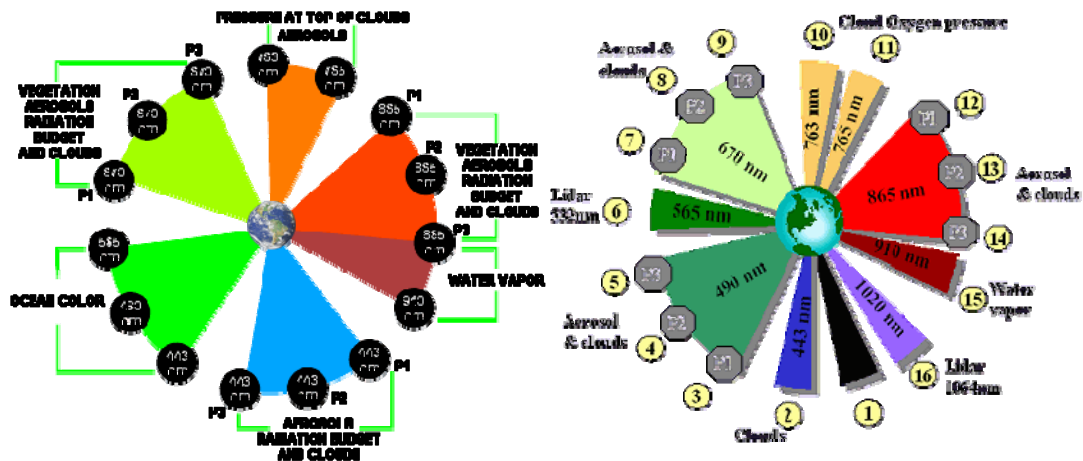


Figure 2.5: Multi-spectral bands used in POLDER-2/ADEOS-2 (left) and POLDER-3/PARASOL (right) (from <http://smc.cnes.fr/>).

Aboard the different satellite platforms, POLDER-2 and POLDER-3 flew on the different orbit of 803 km and 705 km, respectively. With the wide swath across-track (2400 km for POLDER-2 and 1600 km for POLDER-3), POLDER achieves near-global coverage every day in daylight (with a resolution of 6×7 km for POLDER-2 and 5×6.5 km for POLDER-3).

Table 2.2 Characteristics of POLDER-2/-3 and MODIS radiometers, which provide the satellite aerosol products for this thesis.

	POLDER-2/ADEOS-2	POLDER-3/PARASOL	MODIS/Aqua
Satellite Duration	Apr. 2003 - Oct. 2003	Dec.2004 - present	Apr.2002 - present
Orbit Altitude	803 km	705 km	705 km
Swath across track	2400 km	1600 km	2330 km
Equator pass	10h30 LT (Descend)	13h30 LT (Ascend)	13h30 LT (Ascend)
Channels measuring aerosols	3 channels (443, 670 and 865 nm)	3 channels (490, 670 and 865 nm)	7 channels (0.47, 0.55, 0.65, 0.86, 1.24, 1.64 and 2.12 μ m)
Polarized bands	443, 670 and 865 nm	490, 670 and 865 nm	NO
Spatial resolution	6×7 km	5×6.5 km	250×250 m or 500×500 m

Note: characteristics of POLDER-3/PARASOL listed in this table refer in particular to the parameters of this sensor before December, 2009, when it was moved to a lower orbit (3.9 km beneath).

MODIS is a payload scientific instrument operated by NASA since 1999 on board the Terra Satellite, and since 2002 on board the Aqua Satellite. In our study, we only consider aerosol retrievals from the MODIS aboard Aqua, one of the companion satellites of PARASOL in A-Train Constellation. Carried by the Aqua Satellite, this instrument flew in the same orbit of 705 km and crossed the equator nearly at the same local time (13h30) than PARASOL (before December 2009). It captures data in 36 spectral bands ranging in wavelength from 0.4 μ m to 14.4 μ m and at varying spatial

resolutions (2 bands at 250 nm, 5 bands at 500 nm and 29 bands at 1 km). With a ± 55 -degree scanning pattern, the MODIS instrument achieves a 2330-km swath across the track and provides global coverage every one to two days [Salomonson *et al.*, 1989].

Both POLDER and MODIS instruments have excellent capabilities to characterize the spatial and temporal characteristics of the global atmospheric aerosols field. For POLDER, the multidirectional and polarized measurements at 490 (443 nm for POLDER-2), 670 and 865 nm provide a correct description of aerosol spectral signatures, while seven of the 36 channels of MODIS instrument, centered on 0.47, 0.55, 0.66, 0.86, 1.24, 1.64 and 2.12 μm , respectively, are used to retrieve aerosol characteristics [Remer *et al.*, 2005]. The aerosol retrieval algorithms of POLDER and MODIS are described in the following subsection.

2. 2. 3 Aerosol retrieval algorithm of POLDER and MODIS over land

Aerosol retrievals from satellites are performed currently over the cloud-free scenes, which makes cloud-screening the first step in the aerosol retrieval algorithms. Clouds have a very high reflectance that overwhelms the aerosol signal which renders cloud-contaminated pixels not suitable for aerosol retrieval. Several criteria may be applied for cloud detection. The cloud detection scheme implemented in POLDER data processing consists in a simple cloud filtering based on a threshold method [Bréon and Colzy, 1999], while the MODIS method applied the scheme described in Ackerman *et al.*, [1998] to detect the cloudy pixels.

Another difficulty in aerosol remote sensing over land, from clear sky measurements, is to account for the land surface contribution to the Top Of Atmosphere (TOA) reflectance. Unlike the ocean with rather uniform surface signal,

land surfaces are much more variable in their reflectance properties and their spatial variability. Different algorithms have been applied to POLDER and MODIS dataset to solve the inverse problem of separating the surface and atmospheric scattering contributions. MODIS retrievals of aerosol over land [Kaufman *et al.*, 1997a; Remer *et al.*, 2005] are based on the correlation of the surface reflectances in the visible channels (0.47 and 0.66 μm) and the shortwave infrared (SWIR) at 2.1 μm [Kaufman *et al.*, 1997b; Levy *et al.*, 2007a, 2007b]. Whereas, POLDER, which has multi-angle view over a particular pixel, uses polarized light for aerosol retrieval, employing the fact that land surface reflectance is much less polarized than atmospheric scattering, and is independent of the wavelength within the considered spectrum with smaller spatial variability [Deuzé *et al.*, 2001].

After separating land surface and atmospheric contributions to the cloud-screened signal observed at the satellite level, the path radiance, which includes contributions from molecular scattering and absorption, remains. To properly account for molecular effects for the given sun-satellite geometry, a radiative transfer model is usually applied to a set of geometries to provide look-up tables (LUTs) which are used in the retrieval step to speed up the processing [Kokhanovsky *et al.*, 2009]. Additionally, the LUTs are usually prepared using vector radiative transfer calculations for a set of aerosol models which are representative for a certain area [Kaufman *et al.*, 2001; Dubovik *et al.*, 2002b; Levy *et al.*, 2007a, 2007b]. Ideally, aerosol retrieval are implemented finally via the selection of the most appropriate aerosol model or mixture of aerosol models based on a climatology (e.g., Levy *et al.* [2007a], Curier *et al.* [2008]), which can be derived from observations (e.g., Dubovik *et al.* [2002b]; Levy *et al.* [2007a]) or from results obtained using transport models for the area of interest [Curier *et al.*, 2008].

After the general description of satellite aerosol retrieval process, the algorithms

for aerosol retrievals over land from POLDER and MODIS observations are introduced below.

2. 2. 3. 1 Aerosol retrieval algorithm from POLDER observations over land

Aerosol remote sensing over land from visible radiance measurements is more difficult than over ocean because the surface reflectance is generally much greater than the aerosol ones, except over dark surfaces (vegetation in the blue channel, lakes in near infrared). The relative contribution of the land surface to the TOA reflectance, compared to the atmosphere, is much smaller and more stable for the polarized component than that of the total component [Nadal and Bréon, 1999; Waquet *et al.*, 2007]. So, the use of polarized reflectance measurements for aerosol retrievals over land surfaces is a substantially simpler and more robust method. The principle of the algorithm currently used for the analysis of the POLDER observations is based on the one developed in Deuzé *et al.*, [2001]. Essentially, the approach is to use a search of look-up tables (LUTs) to find the size and optical depth of aerosol that best fits the observations in two bands at 670 and 865 nm. The observations are simulated for different atmospheres (aerosol model and optical thickness) and ground surfaces conditions. In a given direction, the simulated polarized radiances, L_p , are computed as follow:

$$L_p = L_p^{mol} + L_p^{surf} \exp[-m(c_a \delta_a + c_m \delta_m)] + L_p^{aer} \exp(-m c_m \delta_m) \quad (2.5)$$

Where L_p^{mol} is the molecular contribution depending on the wavelength and on the pressure or pixel elevation, L_p^{surf} is the surface contribution depending on the kind of surface [Nadal and Bréon, 1999], and L_p^{aer} is the aerosol one which forms the useful

part to extract aerosol properties. The exponential terms, in which c_a and c_m are empirical coefficients, take into account the attenuation of the aerosol signal through the molecular slab and the attenuation of the ground contribution through the total atmosphere. δ_a (resp. δ_m) is the aerosol (resp. molecular) optical depth. The air mass m is equal to $1/\cos\theta_s + 1/\cos\theta_v$, where θ_s (resp. θ_v) is the solar (resp. zenith view) angle.

The contribution from surface to the polarized reflectance, L_p^{surf} , is estimated based on a priori value (as a function of observation geometry and surface type deduced from IGBP classification [Belward *et al.*, 1999]) derived from a statistical analysis of POLDER data [Nadal and Bréon, 1999] and the current normalized difference vegetation index (NDVI) [Tucker, 1979]. The atmospheric contribution is calculated by interpolation within LUTs computed using a multiple scattering code. In order to account for the altitude of the pixel, the calculations are made for two values of molecular optical depth corresponding to surface levels of 0 and 2 km. Likewise, calculations are made also for several aerosol optical depth varying between 0.0 and 2.0 at 865 nm and for 10 aerosol models.

Ground based measurements have shown that the aerosol polarization mainly comes from the small spherical particles [Vermeulen *et al.*, 2000; Li *et al.*, 2009] with radii less than 0.5 μm corresponding to the accumulation mode. So, the aerosol models used in the algorithm consist of single lognormal size distributions of small spherical particles with effective radius varying between 0.075 and 0.225 μm and an effective variance of 0.175 (corresponding to the Angström exponent varying between 3 and 1.8). Polarization measurements at 670 nm and 870 nm do not contain sufficient information to constrain the aerosol refractive index. As the method is mainly sensitive

to fine mode particles, a refractive index of $1.47 - 0.01i$ is assumed for all retrievals, which is the mean value for urban-industrial and biomass burning aerosols [Dubovik *et al.*, 2002b]. When the calculation of LUTs has been accomplished, the aerosol load and type are obtained based on the best fit between the multi-directional polarized POLDER measurements ($Lp_{i\lambda}^{mea}$) and the polarized radiances simulated with Eq. 2.5 ($Lp_{i\lambda}^{sim}$) at 670 and 870 nm. The root mean square, ε_n , which is computed with Eq. 2.6, is considered to indicate the fit quality:

$$\varepsilon_n = \sqrt{\frac{1}{2N} \sum_{\lambda=1}^2 \sum_{i=1}^N (Lp_{i\lambda}^{mea} - Lp_{i\lambda}^{sim})^2} \quad (2.6)$$

The ε_n minimum gives the best model, characterized by its Angström exponent and the corresponding aerosol optical depth.

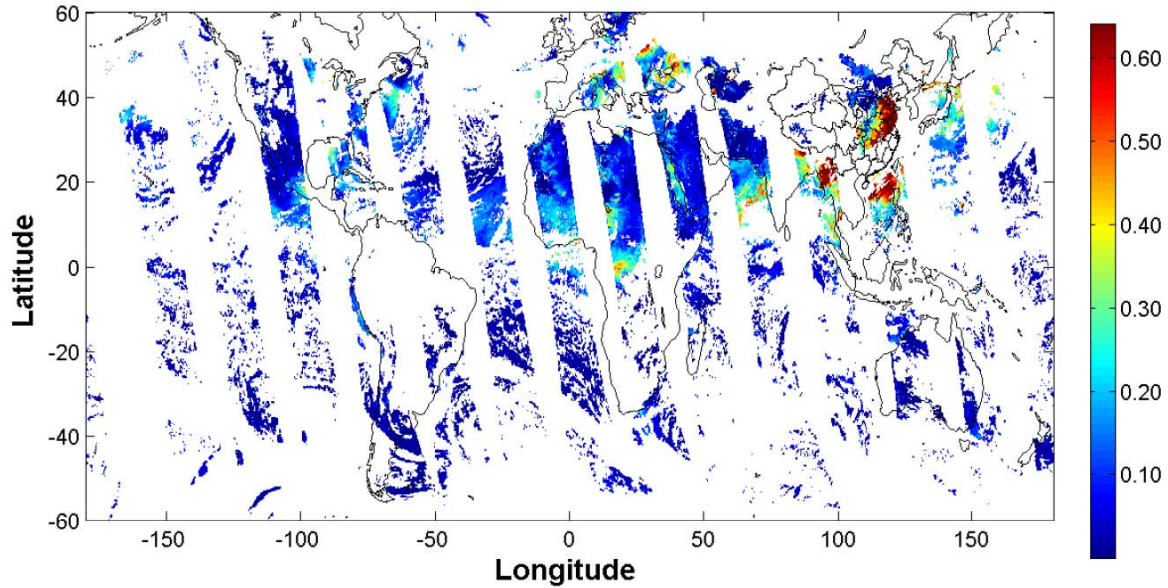


Figure 2.6: Global fine mode AOD at 550 nm computed from fine mode AOD at 865 nm and the corresponding Angström Exponent of POLDER-3 aerosol retrievals on April 6th, 2005.

POLDER level 2 aerosol products are computed from the level 1 product (with spatial resolution of 6 km) for each super-pixel (3×3 pixels) at about 20 km resolution, by orbit segment. All these level 2 parameters are non-directional. In this thesis, we consider principally POLDER-2/-3 level 2 products including geographic coordinate of the pixels, Aerosol Optical Depth of fine mode at 865nm and the Angström exponent between wavelength 865 and 670 nm.

Figure 2.6 presents an example of global fine mode AOD at 550nm computed from fine mode AOD at 865 nm and the corresponding Angström Exponent of POLDER-3/PARASOL aerosol retrievals on April 6th, 2005. Based on the measurements from the environmental protection departments in Beijing, it is a highly polluted day with the air quality of the Grade of V Standards and a visibility of only 1 km. The high POLDER-3 AOD values at 550nm (up to 2.0) appearing around Beijing demonstrate this case of heavy air pollution clearly and imply a possibility of POLDER to monitor the air quality by characterizing aerosol loads.

2. 2. 3. 2 Aerosol retrieval algorithm from MODIS observations over land

MODIS has a unique ability to retrieve aerosol optical depth with great accuracy and to retrieve parameters characterizing aerosol size due to its sufficient spectral diversity [Tanré *et al.*, 1996; 1997]. The algorithm for remote sensing of tropospheric aerosols over land from MODIS [Kaufman and Tanré, 1998] differs from the one applied to POLDER, and is described below.

Aerosol retrieval algorithm over land from MODIS observed spectral reflectance was originally formulated by Kaufman *et al.* [1997a]. So far, MODIS/Aqua aerosol product over land has been updated for 3 times: Collection 003, 004 and 005 (C003-L, C004-L and C005-L for short). The theoretical basis of the algorithm has not changed

from inception, although some of the mechanics and details of the algorithms have evolved. The MODIS aerosol products used in this thesis are retrieved with MODIS aerosol algorithm C005-L described in *Levy et al.* [2007b]. Compared to the C004-L family of algorithms, MODIS C005-L algorithm is a complete overhaul [*Levy et al.*, 2007a, 2007b] with many improvements.

Firstly, the surface reflectance relationships are refined in the new generation of MODIS algorithm [*Levy et al.*, 2007b]. For MODIS C004-L, the surface reflectance in two visible channels (0.47 and 0.66 μm), are each assumed to be fixed ratio of that at 2.12 μm [e.g., *Kaufman et al.*, 1997a; *Remer et al.*, 2005], 0.25 and 0.5, respectively. However, many studies such as *Remer et al.*, [2001] and *Gatebe et al.*, [2001] showed that the VIS/SWIR surface ratios vary as a function of scattering geometry and surface type. Additionally, MODIS C004-L algorithm assumed that aerosol is transparent in the 2.12 μm channel, whereas the C005-L algorithm assumes that the 2.12 μm channel contains information about coarse mode aerosols as well as the surface reflectance [*Levy et al.*, 2007b]. Therefore, the C005-L algorithm adopts a new assumption: over dark surface, the RED/SWIR surface ratio varies as a function of scattering angle and vegetation index, and the RED/BLUE surface ratio is assumed to be fixed. Under this assumption, the relationships between visible bands and SWIR band could be written as follows [*Levy et al.*, 2007b]:

$$\rho_{0.66}^s = f(\rho_{2.12}^s) = \rho_{2.12}^s * slope_{0.66/2.12} + y \text{int}_{0.66/2.12} \quad (2.7)$$

$$\rho_{0.47}^s = g(\rho_{0.66}^s) = \rho_{0.66}^s * slope_{0.47/0.66} + y \text{int}_{0.47/0.66} \quad (2.8)$$

Where: $slope_{0.66/2.12} = slope_{0.66/2.12}^{NDVI_{SWIR}} + 0.002\Theta - 0.27$

$$y \text{int}_{0.66/2.12} = -0.00025\Theta + 0.033$$

$$slope_{0.47/0.66} = 0.49$$

$$y\ int_{0.47/0.66} = 0.005$$

$$slope_{0.66/2.12}^{NDVI_{SWIR}} = 0.48; NDVI_{SWIR} < 0.25$$

$$slope_{0.66/2.12}^{NDVI_{SWIR}} = 0.58; NDVI_{SWIR} > 0.75$$

$$slope_{0.66/2.12}^{NDVI_{SWIR}} = 0.48 + 0.2(NDVI_{SWIR} - 0.25); 0.25 \leq NDVI_{SWIR} \leq 0.75$$

$$NDVI_{SWIR} = (\rho_{1.24}^m - \rho_{2.12}^m) / (\rho_{1.24}^m + \rho_{2.12}^m)$$

$\rho_{0.66}^s$, $\rho_{0.47}^s$, $\rho_{2.12}^s$ represent the surface reflectance in 0.66, 0.47 and 2.12 μm , respectively; $\rho_{1.24}^m$, $\rho_{2.12}^m$ represent the measured surface reflectance in 1.24 and 2.12 μm respectively; Θ is the scattering angle.

The second improvement has mainly been made to radiative transfer code. MODIS aerosol algorithm is based on a Look-Up Table (LUT) approach, i.e., radiative transfer calculations are pre-computed for a set of aerosol and surface parameters and compared with the observed radiation field. The C004 MODIS LUT was calculated using the non-polarized (scalar) SPD radiative transfer (RT) code [Dave *et al.*, 1970], while the algorithm chooses RT3 [Evans and Stephens, 1991], a vector RT code, to calculate the C005-L MODIS LUT. RT3 runs in scalar and vector modes, in order to keep joined with the former version. It is combined with MIEV [Wiscombe, 1981] for spherical fine aerosol and T-matrix [Dubovik *et al.*, 2002a] for the non-spherical coarse aerosol to calculate the scattering properties of modes [Levy *et al.*, 2007b; Zhou *et al.*, 2009].

Furthermore, MODIS C005-L algorithm defines the aerosol models according to the geographical distribution. Five kinds of aerosol models: continental, dust, non-absorbing, neutral absorbing, and highly absorbing, are defined by slightly

modifying the results of *Dubovik et al.*, [2002b]. Moreover, aerosol optical characteristic are also redefined in MODIS new generation of algorithm according to AERONET, especially for single scattering albedo (SSA): $SSA \sim 0.95$ for the non-absorbing model, $SSA \sim 0.90$ for the neutral absorbing model, and $SSA \sim 0.85$ for the highly absorbing model [*Levy et al.*, 2007b].

Additionally, some other modifications are also made in the C005-L algorithm, such as the choice of dark target, cloud mask, snow mask. For more detailed information, please refer to relevant literatures if interested [*Levy et al.*, 2007b].

Although the aerosol products over land retrieved by MODIS C005-L algorithm have not yet been validated on a global scale, they perform better than those produced by C004-L version in their provisional validation and meet the expected accuracy levels ($\pm 0.05 \pm 0.15\tau$) defined by *Remer et al.*, [2005].

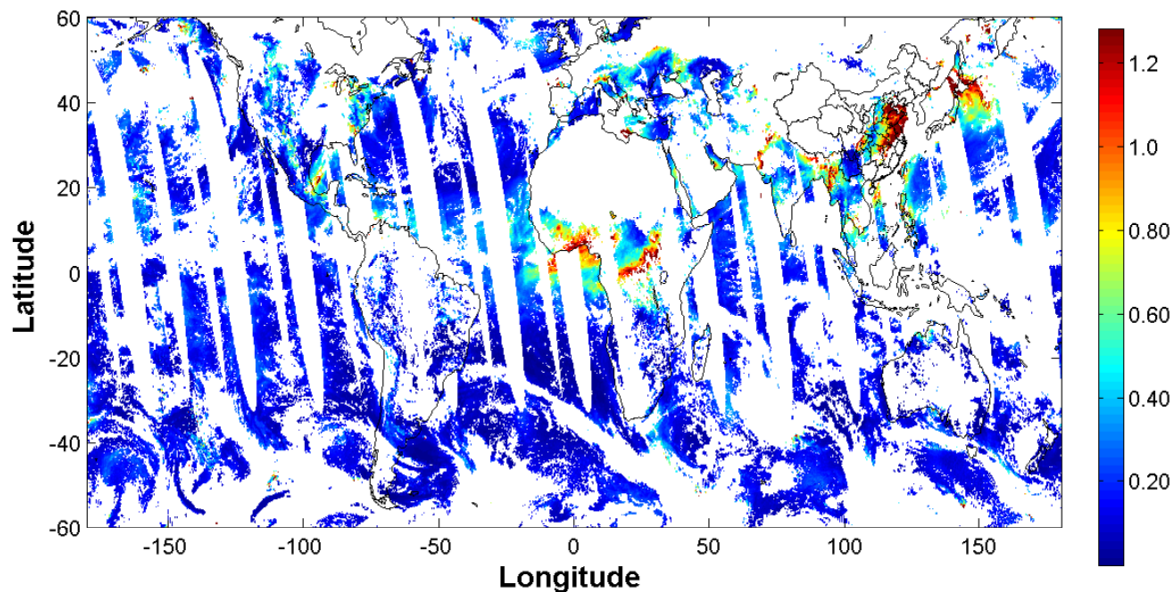


Figure 2.7: global AOD at 550 nm retrieved from MODIS/Aqua observations on April 6th, 2005.

Figure 2.7 provides the same example of AOD at 550 nm as previously shown for PARASOL (Figure 2.6) but retrieved from MODIS/Aqua on April 6th, 2005. The heavy air pollution around Beijing is also highlighted by MODIS high AOD values (up to 5.0). Compared to the Figure 2.6, MODIS AOD at 550 nm is much larger than the one from POLDER-3, although both of these two instruments show the similar patterns of aerosol distribution. This difference could be attributed to their different measuring principles and retrieval algorithm. POLDER instrument is rather sensitive the accumulation mode aerosols due to the use of the polarized measurements, while the MODIS retrievals are sensitive to the entire size distribution [Remer *et al.*, 1996, 2005].

In our study, we considered MODIS Aerosol Optical Depth at 550 nm, fine mode weighting and Angström Exponent for 470 and 670 nm over land.

2. 2. 4 Aerosol retrieval algorithm from POLDER (2-3) and MODIS over ocean

Unlike the aerosol retrieval over land, remote sensing of aerosol over ocean has fewer difficulties in separating surface contribution from the radiance at the top of Atmosphere due to the dark and uniform reflectance (except glint area). Although with the different instrument characteristics (see section 2.2.2), both of POLDER and MODIS aerosol algorithms over ocean retrieve aerosol properties from pre-computed normalized radiance tables (LUTs) compared with their measurements. The retrieval principles were described in *Deuzé et al.* [2000] and *Herman et al.* [2005] for POLDER and in the work of *Tanré et al.* [1997], *Levy et al.* [2003], and *Remer et al.* [2005] for MODIS, respectively.

The radiance at the top of the atmosphere contributed by a mixing of two modes

can be approximated by [Wang and Gordon, 1994]:

$$R_{\lambda}^T(\theta_s, \theta_v, \Phi, \delta_{\lambda}^T) = c_{\lambda} * R_{\lambda}^S(\theta_s, \theta_v, \Phi, \delta_{\lambda}^T) + (1 - c_{\lambda}) * R_{\lambda}^L(\theta_s, \theta_v, \Phi, \delta_{\lambda}^T); \quad (2.9)$$

where R_{λ}^T , R_{λ}^S , R_{λ}^L are the total, small mode, and large mode radiance, respectively (computed with the same total aerosol optical depth δ_{λ}^T), θ_s , θ_v , and Φ are the angles of the solar zenith, the viewing zenith and the relative azimuth. In addition, $c_{\lambda} = \delta_{\lambda}^S / \delta_{\lambda}^T$, where $\delta_{\lambda}^T = \delta_{\lambda}^S + \delta_{\lambda}^L$, with δ_{λ}^S and δ_{λ}^L denoting the small and large mode aerosol optical depth, respectively. Both of POLDER and MODIS aerosol retrieval algorithms use bimodal aerosol model, which mix a mode of small particles (fine mode aerosols) and a mode of large particles (coarse mode aerosols). MODIS inversion considers only large spherical particles whereas POLDER inversion's large particles consist in a mixing of spherical and non-spherical particles with respective optical depth δ_{λ}^{L-S} and δ_{λ}^{L-NS} ($\delta_{\lambda}^L = \delta_{\lambda}^{L-S} + \delta_{\lambda}^{L-NS}$). The mixture concentrations in POLDER inversions $\delta_{\lambda}^{L-S} / \delta_{\lambda}^L$ vary from 0 to 1 by step 0.25. The size distribution of spherical particles (small or large) are assumed to follow a log-normal distribution,

$$n(r) = \frac{dN(r)}{dr} = \frac{N_0}{r\sigma\sqrt{2\pi}} \exp\left[-\left(\frac{\ln(r/r_m)}{\sigma\sqrt{2}}\right)^2\right]; \quad (2.10)$$

Where N_0 is the density number, σ is the standard deviation and r_m is the modal radius. The mode of large non-spherical particles considered in POLDER inversions is the mean model given in Volten *et al.* [2001].

In addition, refractive index is required in characterizing the spherical aerosol component, to compute the scattering matrices and extinction coefficients using Mie theory. POLDER inversion consider non-absorbing aerosol models with refractive indices (with no imaginary) spectrally independent, while the refractive indices of aerosol models from MODIS inversion are wavelength-dependent and exhibit an

imaginary part. In short, POLDER inversions consider 12 fine modes and 13 coarse modes listed in Table 2.3-left, with p denoting the fraction of non-spherical particles within the coarse aerosols, and the aerosol models used in MODIS algorithm consist of 4 fine and 5 coarse modes reported in Table 2.3-right [Levy *et al.*, 2003]. The most significant differences between the LUT of POLDER and MODIS are attributed to non-spherical particles which POLDER can handle [Herman *et al.*, 2005], while the MODIS instrument is not sensitive to the particle shape [Levy *et al.*, 2003].

Table 2.3 Description of aerosol modes used to computer POLDER (Left) and MODIS (right) Look-Up Tables [Gérard *et al.*, 2005]

Small Modes	$r_m, \mu\text{m}$	m	Large Modes	m	$p \%$	$r_m, \mu\text{m}$	σ	m (466 to 865 nm)	m (1243 nm)	m (1632 nm)	m (2119 nm)	
1-S	0.04	1.35-0.0i	1-L	1.33-0.0i	0							
2-S	0.04	1.45-0.0i	2-L	1.35-0.0i	0							
3-S	0.04	1.60-0.0i	3-L	1.37-0.0i	0							
4-S	0.08	1.35-0.0i	4-L	1.33-0.0i	25	1	0.07	0.17	1.45-0.0035i	1.45-0.0035i	1.43-0.01i	1.40-0.005i
5-S	0.08	1.45-0.0i	5-L	1.35-0.0i	25	2	0.06	0.26	1.45-0.0035i	1.45-0.0035i	1.43-0.01i	1.40-0.005i
6-S	0.08	1.60-0.0i	6-L	1.37-0.0i	25	3	0.08	0.26	1.40-0.002i	1.40-0.002i	1.39-0.005i	1.36-0.003i
7-S	0.10	1.35-0.0i	7-L	1.33-0.0i	50	4	0.1	0.26	1.40-0.002i	1.40-0.002i	1.39-0.005i	1.36-0.003i
8-S	0.10	1.45-0.0i	8-L	1.35-0.0i	50							
9-S	0.10	1.60-0.0i	9-L	1.37-0.0i	50							
10-S	0.13	1.35-0.0i	10-L	1.33-0.0i	75							
11-S	0.13	1.45-0.0i	11-L	1.35-0.0i	75	5	0.4	0.26	1.45-0.0035i	1.45-0.0035i	1.43-0.0035i	1.43-0.0035i
12-S	0.13	1.60-0.0i	12-L	1.37-0.0i	75	6	0.6	0.26	1.45-0.0035i	1.45-0.0035i	1.43-0.0035i	1.43-0.0035i
			13-L	-	100	7	0.8	0.26	1.45-0.0035i	1.45-0.0035i	1.43-0.0035i	1.43-0.0035i
						8	0.6	0.26	1.53-0.001i	1.46-0.0i	1.46-0.001i	1.46-0.0i
						9	0.5	0.35	1.53-0.001i	1.46-0.0i	1.46-0.001i	1.46-0.0i

The POLDER LUT is constructed with a radiative transfer code based on successive orders of scattering [Deuzé *et al.*, 1988]. It consists of normalized total and polarized radiance (represented by Stokes parameters) at 670 and 865 nm at the top of atmosphere calculated for each pair of modes (12 fine modes \times 13 coarse modes, leading to 156 possible pairs), for a variety of geometries and a rough ocean surface [Cox and Munk, 1954] with a fixed wind speed of 5 m/s. 21 solar angles (3° to 77°), 20 viewing angles (3° to 73°) and 37 relative azimuth angles from 0° to 180° (step of 5°) are considered. The water-leaving reflectance induced by underwater scattering elements is fixed to 0.001 and 0.000 for 670 and 865 nm, respectively. The foam contribution is computed according to the Koepke's model [1984] and a constant value 0.22 of the foam reflectance. The minimum of the difference (r.m.s.) between the

simulations in LUT and the measurements gives the aerosol model (modes and small mode concentration in term of optical depth C_{865}) and the corresponding optical depth δ_{865} . Note that only a limited set of aerosol parameters is retrieved when the aerosol content is too low or the large range of viewing geometries is not available.

For MODIS LUT over ocean, it is built using the radiative transfer code of *Ahmad and Fraser* [1982]. The top-of atmosphere reflectances at six wavelengths (0.55~2.13 μm) are computed for each pair of modes (4 fine modes \times 5 coarse modes, leading to 20 possible pairs), a variety of viewing geometries, and a rough ocean surface with fixed wind speed of 6 m/s. The water-leaving radiance is assumed to be zero, except for the 550 nm channel, where the water-leaving radiance is assumed to be 0.005. As the output of the MODIS algorithm, the optimal mode pair is given by the minimized differences between simulations and MODIS measurements, as well as the associated total, small, and large mode aerosol optical depth all MODIS aerosol wavelengths.

Both of the inversions over ocean from these two instruments allow us to determine more important parameters, such as Angström exponent (Equation 1.10). Aerosol retrievals over ocean have been validated by *Deazé et al.* [2000] and *Goloub et al.* [1999; 2005] for POLDER and by *Remer et al.* [2002; 2005] for MODIS. Based on the comparison of 350 coincident measurements from POLDER-3/PARASOL and AERONET over one year, an excellent correlation was shown in the total optical depth with the correlation coefficient of 0.97 for both of 670 and 865 nm, while the POLDER Angström exponent shows more dispersion with the correlation coefficient of 0.72. *Remer et al.* [2005] demonstrated the overall high accuracy of MODIS ocean retrieval giving the correlation coefficient above 0.9 for 550, 660 and 870 nm. In this thesis, fine mode AOD derived from POLDER and MODIS total AOD over ocean are combined to characterize the distribution of coarse mode aerosol loads over East Asia.

2. 2. 5 Description of CALIOP and its aerosol retrieval algorithm

The Cloud-Aerosol Lidar with Orthogonal Polarization (CALIOP) is the primary instrument carried on the Cloud-Aerosol Lidar and Infrared Pathfinder Satellite Observations (CALIPSO), which was launched on April 28, 2006 and flew in the A-Train formation (Section 2. 2. 1). It is a space-borne two-wavelength polarization lidar providing global vertical profiles of aerosols and clouds since June 2006 [*Winker et al.*, 2003]. The technical characteristics of CALIOP are presented in Table 2.4. It has been collecting almost continuously high-resolution (333 m in the horizontal and 30 m in the vertical in low and middle troposphere) profiles of aerosols and clouds, using a three-channels receiver with a telescope of 1 meter in diameter, during both day and night portions of the orbit between 82° N and 82° S [*Winker et al.*, 2007]. One of the receiver channels measures the 1064 nm backscatter intensity and the other two channels measure orthogonally polarized components of the 532 nm backscattered signals.

Table 2.4 Key characteristics of CALIOP

Laser	Nd: YAG
Wavelengths	532 nm, 1064 nm
Pulse energy	110 mJ/channel
Repetition Rate	20.25 Hz
Receiver telescope	1.0 m diameter
Polarization	532 nm
Footprint/FOV	100 m/ 130 urad
Horizontal resolution	333m
Vertical resolution	30-60 m

On board CALIPSO, part of the A-Train constellation, CALIOP flies in a 16 day

repeat, sun-synchronous orbit with an equatorial altitude of approximately 705 km. CALIPSO data product day (red) and night orbit (blue) granules on September 23, 2006 are presented in Figure 2.8-left, and the right-hand panel of Figure 2.8 shows the segment of the CALIPSO orbit track passing over our study area highlighted by the green portion on September 23, 2006.

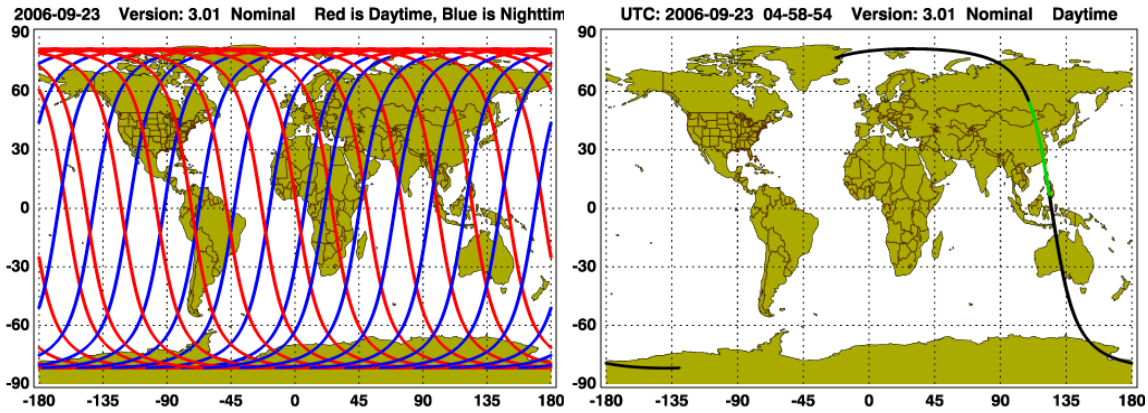


Figure 2.8 Left: Spatial coverage of the CALIOP (day in red and night in blue) orbit tracks on the September 23, 2006 (<http://www-calipso.larc.nasa.gov>); **Right:** Segment of daily orbit of CALIOP on September 23, 2006, with the green portion over-passing China in our study area..

The radiation emitted at 532 and 1064 nm by the laser beam is scattered by the atmosphere (molecules and particles) and then collected by the telescope to be transformed into an electrical signal (and then converted into a digital signal). After corrected for offset voltages, background signals, and instrument artifacts, the resulting signal could be written as:

$$P(z) = \frac{E_0 \xi}{z^2} \beta(z) T^2(z); \quad (2.11)$$

$$\text{Where } T^2(z) = \exp \left[-2 \int_0^z \sigma(z') dz' \right]; \quad (2.12)$$

And $P(z)$ is the corrected signal, z is the altitude of the scattering layer, E_0 and ξ are the average laser energy for the single-shot or composite profile and lidar system parameter, respectively; β is volume backscatter coefficient at the altitude of z , T denotes one-way transmittance from the lidar to the scattering volume at the altitude z , and σ stands for the volume extinction coefficient at the altitude of z .

The CALIOP Level 1 algorithm produces profiles of total attenuated backscatter coefficients for the 532 and 1064 nm and of the 532-nm perpendicular attenuated backscatter coefficients, which are defined, respectively, as follows:

$$\beta_{532,Total}^{att} = (\beta_{532,\parallel} + \beta_{532,\perp})T_{532}^2(z); \quad (2.13)$$

$$\beta_{532,\perp}^{att} = \beta_{532,\perp}T_{532}^2(z); \quad (2.14)$$

$$\beta_{1064,Total}^{att} = \beta_{1064,Total}T_{1064}^2(z); \quad (2.15)$$

The vertical profiles of the total attenuated backscatter coefficients at 532 and 1064 nm, as well as the 532-nm perpendicular attenuated backscatter coefficients, are used to produce science data products by Level 2 algorithm [Vaughan *et al.*, 2004]. The Level 2 algorithms and the data products are outlined in Figure 2.9 and more detail information is described by Vaughan *et al.*, [2004].

In the chapter 6 of this thesis, we analyze the CALIOP Level 2 5-km aerosol layer products briefly to characterize the vertical distribution of aerosol loads, which greatly affects the relation between satellite retrieved AOD and ground-level PM concentrations, over East Asia. The bottom panel of Figure 2.10 shows an example of aerosol layer products derived from CALIOP observations on September 23, 2006, along the green portion of CALIOP orbit track highlighted in Figure 2.8-right. As a reference, the corresponding CALIOP Level 1 products consisting of total attenuated backscatter coefficients at 532 and 1064 nm, and 532-nm perpendicular attenuated

backscatter coefficients are also presented from top to bottom in Figure 2.10.

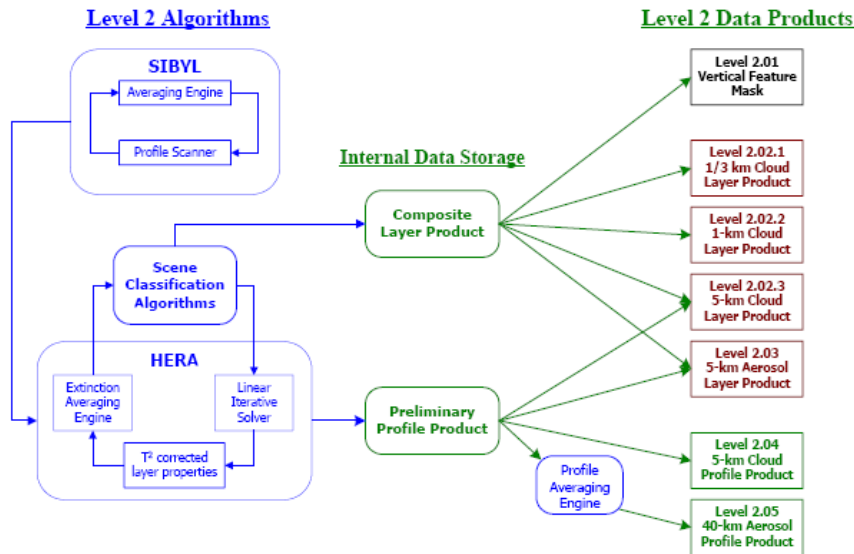


Figure 2.9 Algorithmic origination for each data product type [Vaughan et al., 2004].

The enhanced signals simultaneously appearing in three images of the vertical profiles of total attenuated backscatter coefficients at 532 and 1064 nm, as well as the 532-nm perpendicular attenuated backscatter coefficients (denoted by white boxes), outline the coarse mode, non-spherical particles (might be cirrus clouds). In contrast, enhanced signals in profiles of $\beta_{532,Total}^{att}$ but with little or no enhancement in $\beta_{532,\perp}^{att}$ profiles, combined with the slightly weaker enhancement in $\beta_{1064,Total}^{att}$ profiles, suggest heavy aerosol loads probably comprising fine and coarse mode particles (black ellipses). CALIOP Level 2 aerosol layer products also indicate the similar features in the bottom of Figure 2.10. It is also demonstrated that CALIOP have the excellent capability of detecting aerosol loads with either single or multiple layer structures. Most aerosols concentrate below 2 km, close to the surface, which might mainly originate from the local emissions. In some other cases, aerosol particles (i.e. biomass burning) might also spread above 20 km, which possibly attributed to the long-range transport of aerosols or thin cirrus clouds distinguished incorrectly.

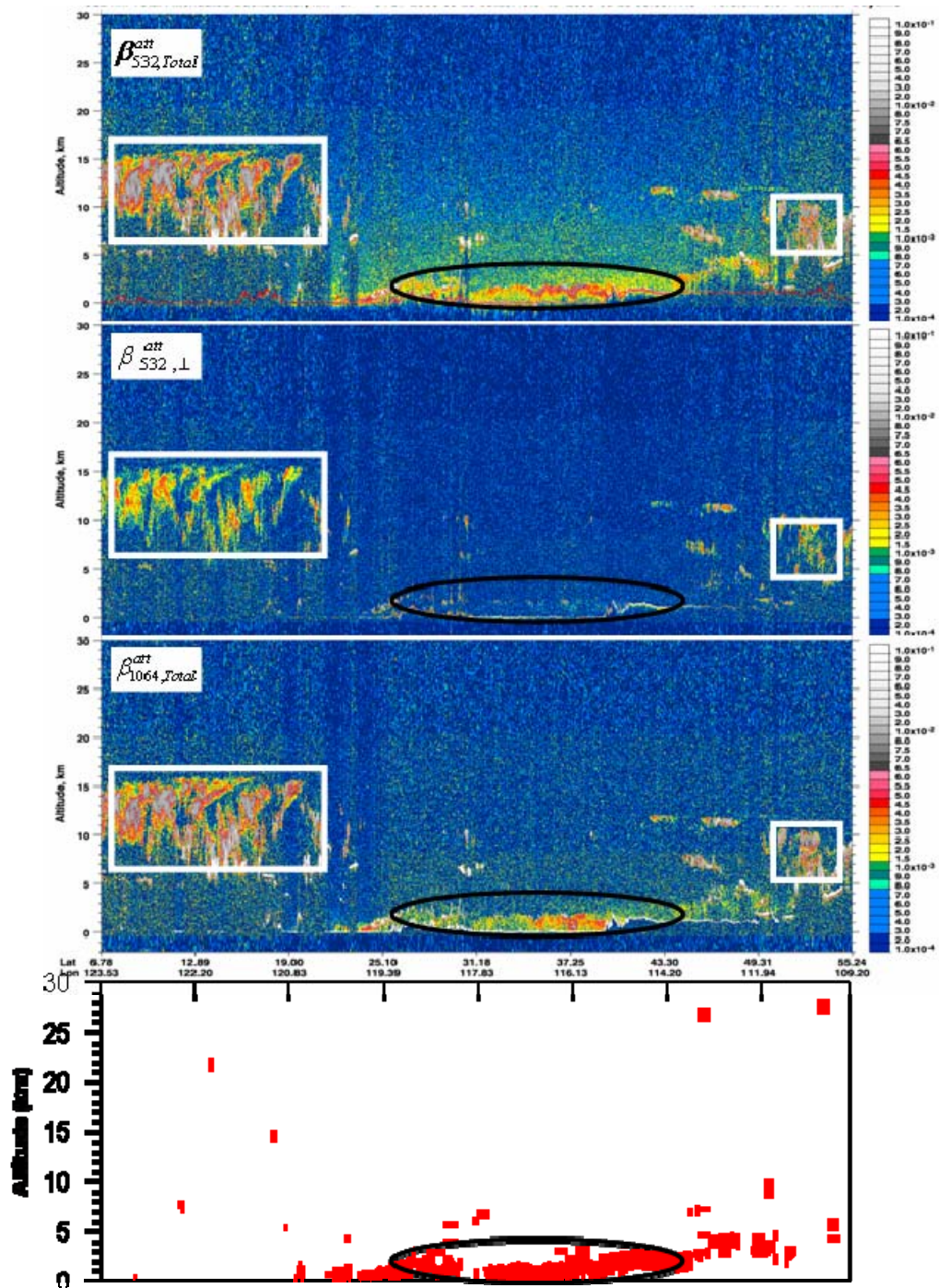


Figure 2.10 From top to bottom, profiles of 532 nm total (parallel + perpendicular) attenuated backscatter, 532 perpendicular attenuated backscatter, 1064 total attenuated backscatter (<http://www-calipso.larc.nasa.gov>) and the aerosol layer altitude (km) derived from CALIOP on September 23, 2006 along the green portion of

orbit tracks in the right panel of Figure 2.8.

2. 3 Particle concentration measurements

Atmospheric aerosols are also called Particulate Matter (PM). The PM mass concentration measured at the ground level is a common way to quantify the amount of aerosol particles in the atmosphere. It is also used as a standard to evaluate air quality by national agencies. PM monitoring is particular important for human health protection because the exposure to suspended particles can contribute to some lung and respiratory diseases and even premature death. However, most of the air-quality monitoring stations are located close to major urban areas leaving large areas without operation observations. Recently, satellite aerosol retrievals, especially with MODIS and POLDER have been shown to provide new opportunity to monitor aerosol loads at larger spatial scale [*Wang and Christopher, 2003; Kacenelenbogen et al., 2006*]. In this thesis, we attempted to apply POLDER aerosol products to estimate fine particulate mass concentration and discussed their potential in the air quality remote sensing. So, we considered PM_{2.5} (the mass concentration of particles with an aerodynamic diameter lower than 2.5 μm) in situ measurements acquired by the TEOM Series 1400a Ambient Particulate Monitor (Thermo Scientific, Waltham, NY) at several stations located around Beijing in China.

The series 1400a Monitor incorporates the patented Tapered Element Oscillating Microbalance (TEOM) technology developed in *Patashnick and Rupprecht, [1991]* to measure particulate matter mass concentrations continuously. The Series 1400a Monitor can be configured with a variety of sample inlets to measure PM₁₀, PM_{2.5}, PM₁ or total suspended particulates (TSP) concentrations with a resolution of $0.1\mu\text{g}/\text{m}^3$.

As a filter-based measurement system, the Thermo monitor continuously measures particulate mass at concentrations between 0 and several 5 g/m³ on a real-time mass monitoring basis. The instrument calculates mass rate, mass concentration, and total mass accumulation on exchangeable filter cartridges that are designed to allow for future chemical and physical analysis. This system operates on the principal that particles are continuously collected on a filter cartridge mounted on the tip of tapered hollow glass element. The element oscillates in an applied electric field. With this monitor, particle-laden air enters through an air inlet and then passes to the sensor unit containing the patented microbalance system. When mass accumulates on the filter cartridge, the resonant frequency of the element decreases, resulting in a direct measurement of inertial mass. Based upon the direct relationship between mass and frequency, the monitor's microcomputer calculates the total mass accumulation on the filter and the mass concentration in real-time. The instrument has a precision of ±5.0 µg/m³ for 10-minute averaged data, ±1.5 µg/m³ for 1-hour averages and ±0.5 µg/m³ for 24-hour averages.

A more complete description can be found in *Patashnick and Rupprecht*, [1991]. Here, we provide some formulas below used in the computation. In a spring-mass system the frequency follows the equation:

$$f = \sqrt{K/M} \quad (2.16)$$

Where f is frequency (radians/sec), K is spring rate, and M is mass in the consistent units with K . The relationship between mass and change in frequency can be expressed as:

$$\Delta m = K_o \times \left(\frac{1}{f_1^2} - \frac{1}{f_0^2} \right) \quad (2.17)$$

Where Δm is change in mass (µg), K_o is spring constant (including mass conversions), f_0

and f_1 are initial and final frequency (Hz) respectively. Additionally, mass concentration (C , $\mu\text{g}/\text{m}^3$) can be written as:

$$C = \frac{\Delta m}{Ft} \times 10^3 \quad (2.18)$$

Where Δm (μg) is the accumulated mass, F is flow rate (L/min), and t is the time (min).

Compared to other methods, the TEOM technology is higher in sensitivity, better in accurateness, although it is easily affected by the ambient humidity. In order to minimize the effects of changing ambient conditions, the sample stream is preheated to 50°C before entering the mass transducer, which results in an underestimation of the PM values by TEOM caused by the evaporation of ammonium-nitrate [Hodzic *et al.*, 2005]. In this thesis, we considered 24-h averaged fine particle mass concentrations obtained over several stations located around Beijing in China (from the beginning of 2004 to May, 2010) and attempted to establish the relationship between PM_{2.5} and POLDER AOD. Some preliminary discussions are performed focusing on the potential of POLDER in air quality remote sensing.

2. 4 Conclusion and Strategy

To sum up the above statements, we considered multi-platform, and multi-resolution databases including POLDER-3/PARASOL Level 2 aerosol retrievals, AERONET Level 1.5 aerosol inversions, MODIS/Aqua Level 2, CALIOP/CALIPSO Level 2 aerosol layer products, and ground-level PM_{2.5} concentration measurements, to characterize the aerosol loads over East Asia more comprehensively. The frame of this thesis is outlined in Figure 2.11, where the datasets are highlighted in blue boxes and the main achievements performed in this study are summarized in green boxes.

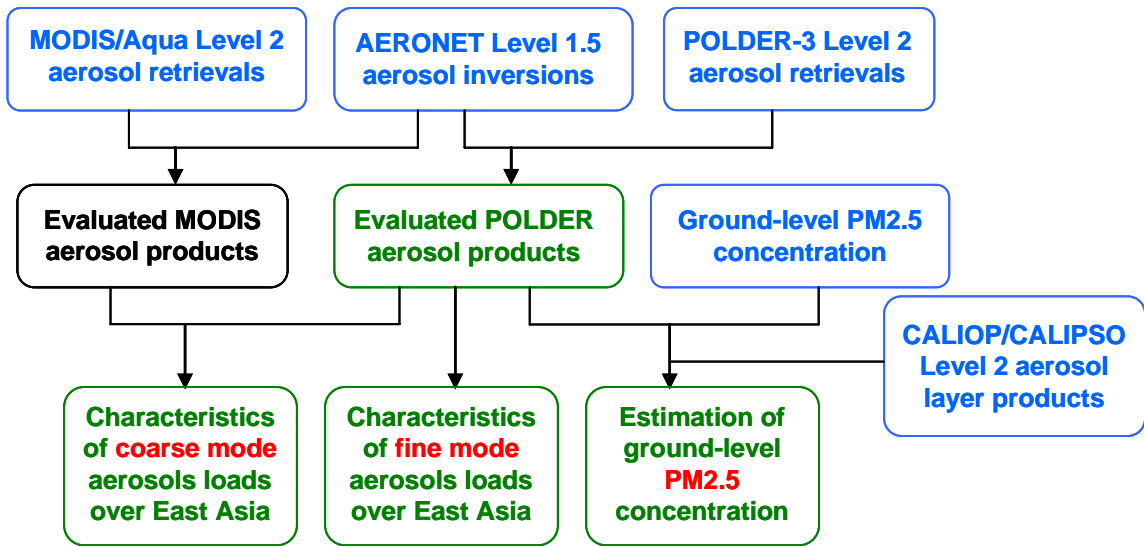


Figure 2.11 Datasets and the strategy used in thesis.

Chapter 3

Regional validation of POLDER-3 aerosol retrievals over land

As the first generation of large-field of view polarimeter, POLDER (Polarization and Directionality of Earth's Reflectances) sensors [Deschamps *et al.*, 1994] have flown on ADEOS-1 (8 months), ADEOS-2 (7 months) and PARASOL (more than five years), providing aerosol optical and microphysical properties in a unique way thanks to its directional polarized measurements at 670 and 865 nm. At the present, all of the PARASOL observations, as well as POLDER-1 and POLDER-2, have been processed by the same algorithm [Deuzé *et al.*, 2001] and more than six years of data are available for us to explore more characteristics of aerosol loads on an extended time scale. However, the quality of POLDER continent aerosol products has to be evaluated first. Considering the lack of validation of POLDER-3 continent aerosol retrievals, especially over East Asia, we performed the regional validation of POLDER-3/PARASOL aerosol retrievals over land by comparing them with AERONET inversions from 14 AERONET sites located over East Asia.

3. 1 Data collection and processing

Our primary area of interest was East Asia, defined as the area with latitude ranging from 10 ° N to 55 ° N and longitude ranging from 70 ° E to 140 ° E in this work. In order to obtain the largest amount of available ground-based data collocated by satellite retrievals, we used Level 1.5 AERONET AOD and inversions products to evaluate POLDER-3 retrievals at 865, 670 and 440 nm. When we performed this evaluation phase, we needed an as dense as possible aerosol record. For many sites, level 2 data were not available, and in order to get the most recent AERONET data

records, we had to use level 1.5 AOD and inversions products. Nevertheless, to keep the best quality data we applied additional filters on the data, explained hereinafter. Figure 3.1 showed the area we focused on and the 14 AERONET sites (6 sites in China; 2 sites in Thailand and Japan; one site in India, Vietnam, South Korea and Mongolia respectively) considered in our analysis, providing more than 250 days with available data during the period from March 2005 to June 2008. More descriptive information for each site was presented in Table 3.1.

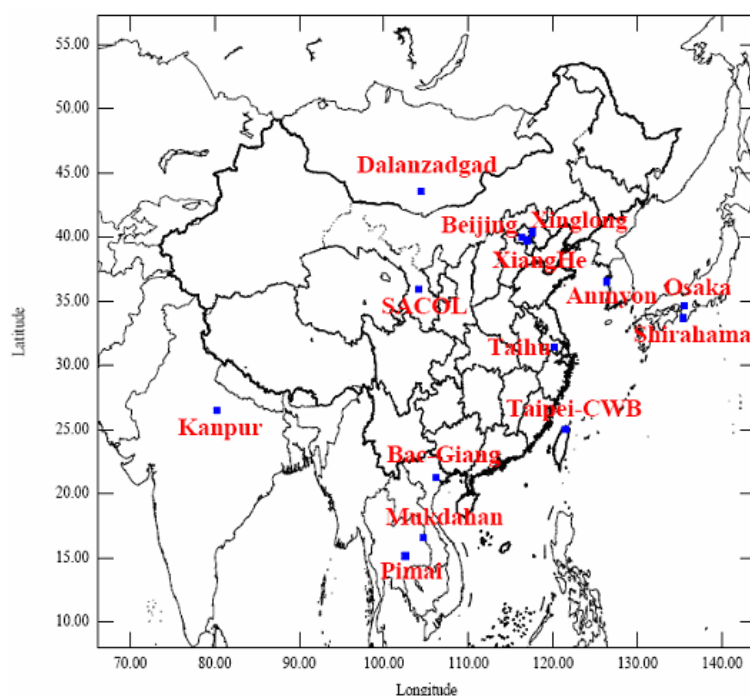


Figure 3.1: Map of the study area including the locations of the 14 AERONET sites (filled blue squares) in East Asia.

3. 1. 1 AERONET data and processing method

In a recent study performed over Beijing and XiangHe AERONET sites, *Fan et al.* [2008] demonstrated a good agreement between POLDER-3 and a fraction of the fine mode AOD (particle radius $\leq 0.3 \mu\text{m}$). Based on this previous work that was limited

to two sites and a 15-month time period, we evaluated POLDER-3 AOD over land more comprehensively and systematically over 14 different sites located in East Asia over a period of 40 months from March 2005, to June 2008.

Table3.1: *Geographic of 14 AERONET/PHOTONS sites considered in this paper.*

Sites	Latitude (° N)	Longitude (° E)	Elevation (m)	Country
Beijing	39.9	116.4	90	China
SACOL	35.9	104.1	1960	China
Taihu	31.4	120.2	20	China
Taipei_CWB	25.0	121.5	26	China
XiangHe	39.7	116.9	36	China
Xinglong	40.4	117.6	970	China
Anmyon	36.5	126.3	47	South Korea
Bac_Giang	21.3	106.2	15	Vietnam
Dalanzadgad	43.6	104.4	1470	Mongolia
Kanpur	26.5	80.2	123	India
Mukdahan	16.6	104.7	166	Thailand
Pimai	15.2	102.5	220	Thailand
Osaka	34.6	135.6	50	Japan
Shirahama	33.7	135.4	10	Japan

In analyzing AERONET data, we adopted a methodology similar to *Fan et al.* [2008]. Several filters were considered and applied to the data in order to detect and keep the more stable atmospheric conditions for comparing satellite and ground-based data. We first selected AERONET AOD level 1.5 data matching satellite overpass time within +/- 30 minutes with four AOD observations available (AOD observation every 15 minutes). Then, we computed the ratio between the temporal standard deviation, $\sigma(\tau_{total}^{AER})$, and the average AOD, τ_{total}^{AER} , over the four values, keeping the information only when the ratio was lower than 0.20. Additionally, the sky error and the solar zenith angle of the almucantar were also considered in order to make further improvement on the data quality. We did not considered the AERONET inversion

products when sky radiance fitting error was larger than 5% and the solar zenith angle less than 45 degree. Finally, knowing that we would have to compute fine mode AOD from the retrieved size distribution and refractive indexes, we considered the two following additional criteria. When calculating the fine mode AOD from AERONET inversions products, we rejected data with real part of the complex refractive index reaching the rather non realistic value of 1.6 (maximum considered in AERONET retrievals). Moreover, we selected inversion products at times (inversion time) as close as possible to the satellite overpass time. However, time differences between the satellite overpasses and the first available inversion products were sometimes more than 2 hours. Therefore, to protect from the impact of a possible atmospheric change, we considered only inversion products when the Angström exponent, α , remained stable ($\Delta\alpha < 0.1$). Moreover, to account for possible changes in AOD with stable α values, we introduced specific correction given by Eq.3.1.

Fan et al. [2008] established for Beijing AERONET site at a 0.3 μm particle radius threshold, for fine mode definition consistent with POLDER retrievals. Assuming this value all over East Asia, we computed the fine mode AOD, $\tau_{\text{fine}(r \leq 0.3 \mu\text{m})}^{\text{inv}}$, from size distribution and refractive index, assuming spherical particles. As mentioned previously, we accounted for the possible temporal variation of AOD between inversion and satellite-overpass times, using the following equation:

$$\tau_{\text{fine}(r \leq 0.3 \mu\text{m})}^{\text{AER}} = \tau_{\text{fine}(r \leq 0.3 \mu\text{m})}^{\text{inv}} \times \left(\frac{\tau_{\text{total}}^{\text{AER}}}{\tau_{\text{total}}^{\text{inv}}} \right)_{\alpha} \quad (3.1)$$

Where $\tau_{\text{total}}^{\text{AER}}$ is the total AOD averaged within ± 30 min around the satellite overpass time, $\tau_{\text{total}}^{\text{inv}}$ is the total AOD measured at the inversion time, $\tau_{\text{fine}(r \leq 0.3 \mu\text{m})}^{\text{AER}}$ is the estimated fine mode AOD truncated at 0.3 μm at overpass time and $\tau_{\text{fine}(r \leq 0.3 \mu\text{m})}^{\text{inv}}$ is the

fine mode AOD computed at inversion time.

3. 1. 2 POLDER level 2 aerosol products and processing method

POLDER Level 2 aerosol retrievals over land consist of AOD at 865 nm (τ_{865nm}^{Sat}) and Ångström exponent (α^{Sat}) at 20 km \times 20 km spatial resolution. POLDER-1, -2 and -3 data were processed using the same algorithm described by *Deuzé et al.* [2001]. The inversion scheme is based on a “Look-Up Table” approach, assuming spherical absorbing particles with monomodal size distribution and a given refractive index. Retrievals analysis demonstrated [*Deuzé et al.*, 2001] that the refractive index can not be retrieved reliably, therefore an average refractive index of 1.47-0.01i estimated from *Dubovik et al.* [2002] climatology was considered. The retrieved aerosol parameters τ_{865nm}^{Sat} and α^{Sat} correspond to the aerosol model and average refractive index that give the best agreement between measured and simulated polarized radiances at 670 and 865 nm. Since the POLDER algorithm over land relies only on polarized radiances measured at 670 and 865 nm that are known to be mainly sensitive to small particles, the retrieved aerosol parameters are related to the smaller fraction of the accumulation mode. Ångström exponent was not studied as such in our study, but was used to derive the AOD at shorter wavelength (670 and 440 nm) following Eq. 3.2:

$$\tau_{\lambda}^{Sat} = \tau_{865}^{Sat} \times \left(\frac{\lambda}{865}\right)^{-\alpha^{Sat}} \quad (3.2)$$

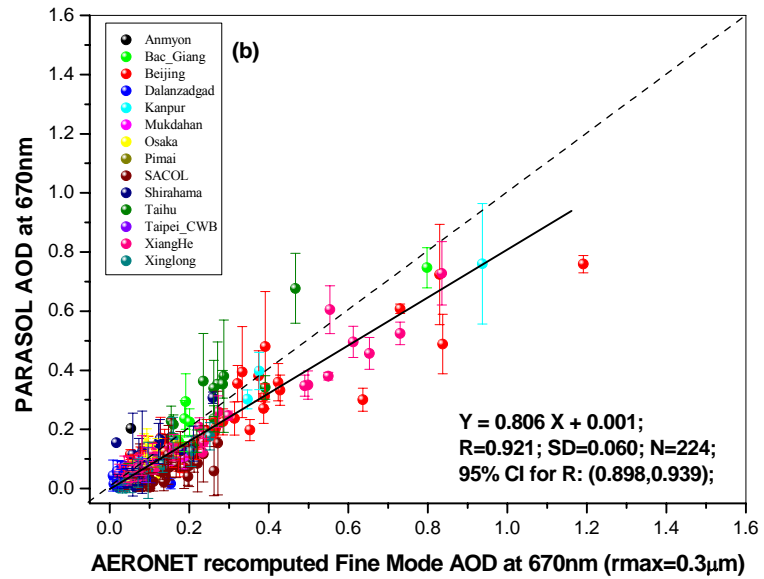
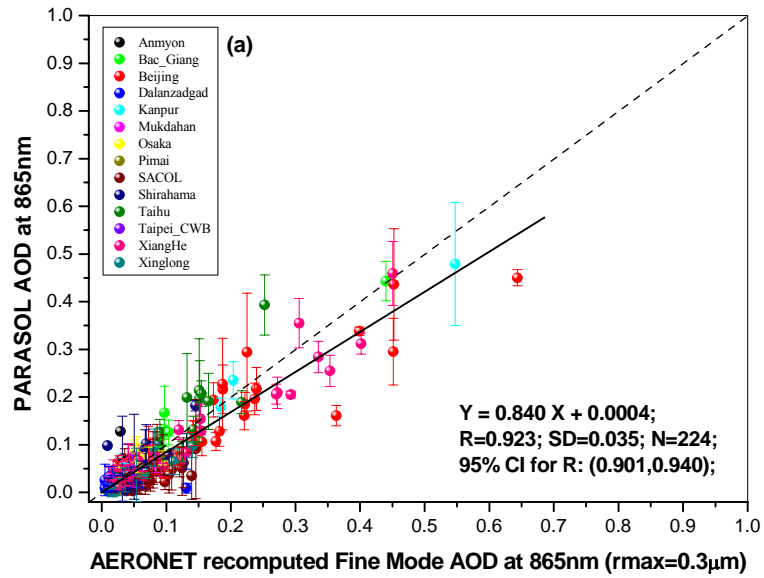
Due to calibration uncertainty in the POLDER-3 blue polarized channel, this channel cannot be used for retrieval. However, since the 440 nm channel has been shown to be useful for some air quality monitoring [*Kacenenbogen et al.*, 2006], we also derived AOD at 440 nm by extrapolation using Eq. 3.2, knowing that this extrapolation would bias the AOD due to the non-linearity of Angström exponent for

fine particles, particularly for aged fine mode pollution or smoke, which commonly occur in East Asia [Eck *et al.*, 1999]. Hence, in our work, we use AERONET data to evaluate POLDER-3 retrievals first of all at 865 nm (τ_{865}^{Sat}) and 670 nm (τ_{670}^{Sat}), but we also considered the extrapolated AOD at 440 nm (τ_{440}^{Sat}) in this exercise. These parameters have been averaged over a $0.5^\circ \times 0.5^\circ$ size box centered on each sun-photometer site. Moreover, the standard deviation within this box is provided to estimate the spatial variability around the sun-photometer location. The AERONET and POLDER-3 aerosol retrievals are then matched in both time and space to evaluate POLDER-3 aerosol retrievals over East Asian land surfaces. Results of these comparisons are presented and discussed in the following section.

3. 2 Results and Discussion

Comparisons of POLDER-3 AOD against $\tau_{fine(r \leq 0.3 \mu m)}^{AER}$ are shown in Figure 3.2a, 3.2b and 3.2c respectively for 865, 670 and 440 nm channels. The error bars on the Y-axis represent the spatial standard deviation computed over the $0.5^\circ \times 0.5^\circ$ size window. Similar comparison for 440 nm is presented without error bars since the standard deviation was very similar to that of 865 and 670 nm. Our results demonstrated overall good agreement between POLDER AOD and $\tau_{fine(r \leq 0.3 \mu m)}^{AER}$. The correlation coefficients are 0.92, with the 95% Confidence Intervals (CI) from 0.90 to 0.94, for both of 865 and 670 nm. For 440 nm, the correlation coefficient is 0.908 and the corresponding 95% CI is 0.88–0.93. The slopes, calculated by the robust regression method based on iteratively reweighted least squares, are 0.84, 0.81 and 0.7 for 865, 670 and 440 nm, respectively. The observed decrease of the slope with wavelength can very likely be explained by extrapolation validity as well as limitations in the retrieval assumptions such as departure between modeled and true absorption, particle shape and residual

surface contribution.



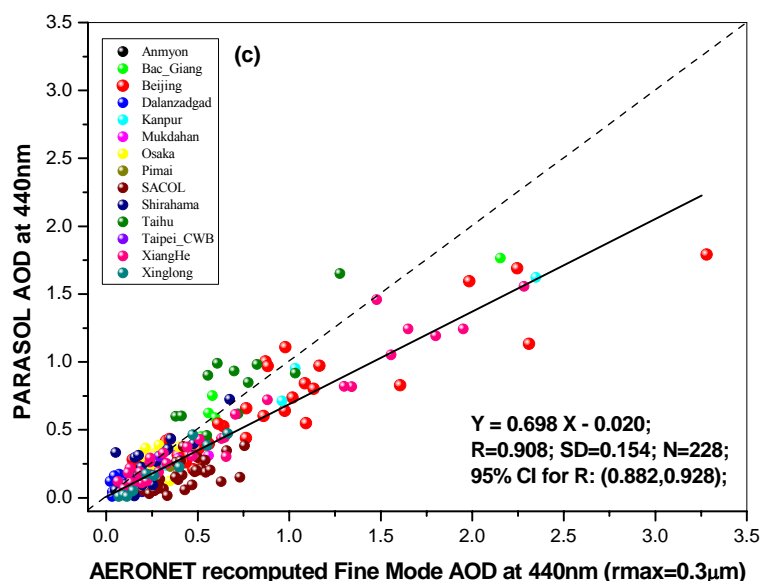


Figure 3.2: Comparisons between POLDER-3 AOD and AERONET recomputed fine mode AOD ($r \leq 0.3 \mu\text{m}$) at 865 nm (a), 670 nm (b) and 440 nm (c) over 14 sites located in East Asia from March 2005 to June 2008. POLDER-3 AOD at 670 and 440 nm were computed from POLDER-3 AOD at 865 nm and the corresponding Ångström exponent. Error bars in (a) and (b) show spatial variation of POLDER pixels.

More detailed information (site by site) from robust regression is provided for the 865 nm channel in Table 3.2. In order to insure the reliability of regression results, we skip 4 sites having less than 5 days with available data, including Kanpur (4 days), Mukdahan (4 days), Pimai (4 days) and Taipei_CWB (2 days). Averaged AERONET and satellite AOD for each site are presented in the second and third columns in Table 3.2, along with the RMS indicating daily variation. All statistical data are arranged in order of increasing averaged AERONET AOD in order to partially reflect the aerosol pollution level for each site. For most of the sites, the averaged POLDER-3 AOD is rather comparable with the ground-based AOD. The results of robust regression analysis are also presented in Table 3.2, where R, together with its 95% Confidence Interval in the fifth column, represents the correlation coefficient and N represents the

number of days with both satellite and ground-based data. The SD provided in the sixth column of Table 3.2 is actually the residual standard deviation, suggesting the degree of dispersion from the actual data to the linear regression line.

Table 3.2: *Statistics and robust regression analysis between PARASOL AOD and fine mode AOD from AERONET measurements at 865 nm (March 2005 to June 2008)*

Site	Mean Value		Robust Regression					
	AERONET	PARASOL	R	95% CI for R	SD	slope	intercept	N
Dalanzadgad	0.01± 0.01	0.02 ± 0.01	0.16	(-0.42, 0.65)	0.01	0.38	0.01	13
Anmyon	0.04 ± 0.01	0.04 ± 0.01	0.84	(0.40, 0.97)	0.01	0.77	0.01	9
Osaka	0.05 ± 0.02	0.05± 0.03	0.61	(0.12, 0.86)	0.02	0.97	0.00	14
Shirahama	0.05 ± 0.03	0.05 ± 0.04	0.72	(0.46, 0.88)	0.03	0.98	0.00	25
Xinglong	0.06 ± 0.04	0.04 ± 0.04	0.93	(0.73, 0.98)	0.01	0.78	- 0.01	10
SACOL	0.07 ± 0.03	0.03 ± 0.02	0.67	(0.44, 0.82)	0.02	0.56	-0.01	37
XiangHe	0.13 ± 0.13	0.11 ± 0.11	0.96	(0.93, 0.98)	0.03	0.85	0.00	32
Beijing	0.13 ± 0.13	0.11 ± 0.10	0.93	(0.89, 0.96)	0.04	0.73	0.01	52
Taihu	0.14 ± 0.06	0.17 ± 0.09	0.87	(0.60, 0.97)	0.05	1.27	0.00	12
Bac_Giang	0.15 ± 0.14	0.17 ± 0.14	0.97	(0.78, 1.00)	0.03	0.95	0.03	6

For nine sites out of ten, the correlation coefficients (R) are better than 0.6 and the majority of slopes are close to one. Nevertheless, there are three sites with 95% CI for R wider than 0.5, which probably were induced by the few number of available data.

For Dalanzadgad site, the correlation coefficient of 0.16 shows no strong correlation between POLDER-3 retrievals and AERONET inversions. The main explanation may be attributed to the very low level of AOD over this site, which is located in the Gobi areas of Mongolia, together with restrictively limited AOD range. The atmosphere is generally quite clear and clean except during dust events that are estimated to occur 30 times per year [Mandakh *et al.*, 2002; Qian *et al.*, 2006]. The multi-annual AERONET total AOD at 865 nm measured over Dalanzadgad was only

0.07; this is much lower than the total AOD recorded over Beijing, which was 0.41. In most cases, dust events generating mainly coarse non spherical particles are very weakly polarizing light making therefore these particles almost non detectable with POLDER current retrievals. The distribution of blues dots in Figure 3.2 also partly reflects the particular characteristic of aerosols over this site.

3. 3 Conclusions

In this chapter, we evaluated POLDER-3 against AERONET AOD values, based on 14 AERONET/PHOTONS sites located over several countries of East Asia. Results show a good agreement between space and ground-based fine mode AOD (particle radii less than or equal to $0.30 \mu\text{m}$). We observed that 9 AERONET stations out of ten have correlation coefficients above 0.6 and 4 sites above 0.9. POLDER retrievals are shown to underestimate this fine mode AOD by 16 %, 20 % and 30% for 865, 670 and 440 nm respectively. Nevertheless, good correlations were observed over most of the AERONET sites considered in this paper, thus confirming the high quality of the POLDER aerosol retrievals, as well as their capacity to detect the fine part of aerosol loads.

These results indicate that POLDER aerosol products over land are quite relevant for analyzing spatial and temporal distributions of fine particles over East Asia. This analysis is developed in the next chapter.

Chapter 4

Characteristics of aerosol loads over East Asia from POLDER observations

East Asia is an important source of both natural and anthropogenic aerosols due to its geographical characteristics and the rapid growth of its economy. However, our knowledge on the spatiotemporal distributions of aerosols over this area is still limited due to the lack of long-term and large-coverage observations [Choi *et al.*, 2009; Li *et al.*, 2002; Xu *et al.*, 2004; Park *et al.*, 2005; Li *et al.*, 2008]. China, centrally located in East Asia, shows higher emissions of both natural and anthropogenic aerosols. The mean total AOD in China is about twice the global continental mean value [Li *et al.*, 2002]. Beijing, the political and cultural center of China, is even recognized as one of the world's 10 most polluted cities, and also shares the distinction of being the world's most polluted capital with Mexico City. During the last 30 years, Beijing has been experiencing severe aerosol pollution predominantly caused by rapid economic development, population expansion and urbanization, as well as some secondary problems such as increasing traffic density, a high consumption of coal, flourishing construction activities and dust storms from deserts [Sun *et al.*, 2004; Chan *et al.*, 2008].

As an indicator of air quality, Aerosol Optical Depth in Beijing has been revealed to reach its maximum during summer because of atmospheric stagnation events that are typically associated with high temperatures [Fan *et al.*, 2006; Xia *et al.*, 2006, 2007]. According to the previous studies, the severe aerosol pollution in Beijing is not only a result of internal emission sources within Beijing, but also the atmospheric pollution of

surrounding Provinces [Xu *et al.*, 2002, 2003, 2005, 2006]; this is particularly true during summer due to a combination of southerly winds and the topography of the surrounding regions [He *et al.*, 2009]. Numerical simulations have also suggested that 34% of PM_{2.5} [Streets *et al.*, 2007] and 40% of PM₁₀ [Chen *et al.*, 2007] in summer over urban Beijing could be generated by regional emissions. In order to improve the air quality in Beijing and ensure a healthier atmosphere for athletes and spectators during the 2008 summer Olympic Games, China introduced extensive provisions and enforced emission reductions in Beijing and its surrounding areas before and during the event. Such an effort provided a unique opportunity to study the anthropogenic contribution to the atmospheric aerosol loads.

We, therefore, considered POLDER-3 retrievals from March 2005 to February 2009 in order to characterize aerosols patterns over East Asia as well as seasonal variability first. And then, we focused our analysis on aerosol variability during the summer in Beijing and its surrounding Provinces, which are termed “North China” in this article.

4. 1 Characteristics of POLDER AOD distribution over East Asia

4. 1. 1 Spatial distribution patterns of aerosol loads from POLDER

In order to provide a first overview of the aerosol distribution over this very large region, we show in Figure 4.1a a four year POLDER-3 averaged AOD. Information on the percentage of days with available aerosol retrievals is also given in Figure 4.1b. Percentages lower than 100% are due to cloud cover (e.g., the whole area, especially Southeast Asia and the southern part of China), to topographic features of the underlying surface (e.g., the Tibetan Plateau) or to missing data (the white color in the inland areas). Moreover, to aid interpretation, locations of several typical areas

mentioned below are marked in Figure 4.1c.

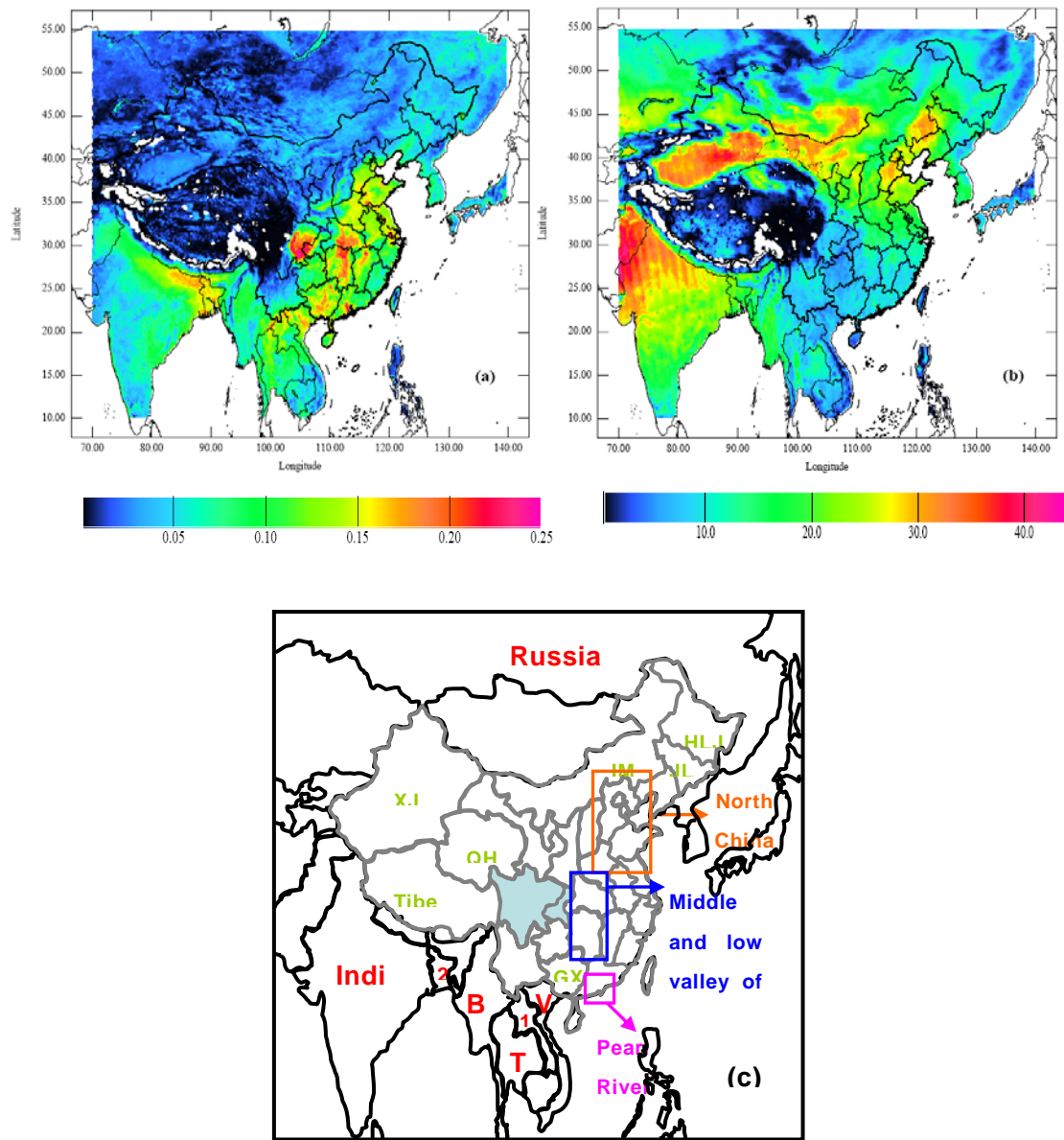


Figure 4.1: (a) Map of averaged AOD at 865 nm and (b) pixel frequency based on PARASOL observation over a four-year period (March 2005-February 2009). The frequency is calculated as the number of days with successful PARASOL aerosol retrievals in clear sky divided by the total number of calendar days during the study period. (c) Illustration of typical areas mentioned in this paper, where the Sichuan Basin is presented with a shadow. Country names are given in red, including red “1”

and “2” stand for Laos and Bangladesh respectively, while the names of provinces in China (gray boundaries) are written in light green.

As shown in Figure 4.1a, the highest average AOD mostly appears in the Sichuan basin and the south-eastern region of China, particularly around the middle and lower valley of the Yangtze River, the Delta of the Pearl River and the North China Plain which are densely populated, highly industrialized and economically developed. Additionally, there are also several other areas with high AOD value, such as the south-Himalaya region in India and the areas around the border between China and Laos. According to our study, the maximum of POLDER-3 AOD value over East Asia has been estimated as 0.25; whereas, the mean value is 0.05. Excluding the very clear regions over the Tibetan Plateau and the north-west part of East Asia which are beyond the scope of this study, the low AOD values primarily appear over Northeast China, including Heilongjiang (HLJ), Jilin (JL) Province and inner-Mongolia (IM).

Similar patterns have also been demonstrated by *Luo et al.* [2001] based on the analyses of total AOD retrieved from a network of 46 solar radiation stations as well as with MODIS total AOD within August 2000 to April 2003 period [*Li et al.*, 2003].

However, there are some areas with high AOD derived from MODIS in the western part of Tibet, the Tarim Basin of Xianjiang (XJ) and the Qaidam Basin in Qinghai Province (QH) mentioned by *Li et al.* [2003] that are not highlighted by POLDER. This difference is likely related to the specificity of the POLDER-3 retrievals over land, which is not sensitive to the coarse mode fraction characterizing dust particles occurring in these regions. There is another visible feature in the Sichuan Province where the highest AOD, appearing in the east, contrasts sharply with the lowest values retrieved in the west part of the province. This remarkable difference is likely due to the unique topography of Sichuan Province. The elevation in the west part

is almost 10 times higher than the elevation in the east. The terrain with higher elevation certainly limits aerosol transport and therefore exhibits lower AOD.

4. 1. 2 Seasonal variability of POLDER AOD over East Asia

A more precise examination of the seasonal variation of aerosol patterns is presented in Figure 4.2 in which the four seasons: spring (MAM), summer (JJA), autumn (SON), and winter (DJF) are separated. The white color in the inland regions again represents areas in which the valid retrievals were not obtained.

In spring (Figure 4.2a), the highest AOD values mostly appear in the Sichuan Basin, the Pearl River Delta in China, the areas around Stanovoy Range in Russia (the north of Heilongjiang Province in China) and Southeast Asia, especially in the northern part of Laos and its surrounding areas in Burma (B), Thailand (T) and Vietnam (V), which nearly link up with the high AOD value area in the southern Guangxi Province (GX) of China. The high AOD values in Sichuan Basin seem consistent with its high population density and its unique topography benefiting the retention and accumulation of aerosol pollutants [*Li et al.*, 2003], while the high values over Southeast Asia and Russia are very likely due to slash-and-burn farming and forest fires [*Kim et al.*, 2004; *Murdiyarto et al.*, 2007; *Padoch et al.*, 2007; *Damoah et al.*, 2004; *Lee et al.*, 2005; *Kanaya et al.*, 2003]. Along with local aerosol emissions, fine mode particles generated by the biomass burning in Southeast Asia may be transported to the south of China following the dominant westerly wind during the spring; this is likely the cause of the high AOD in Guangxi Province and the Pearl River Delta [*Li et al.*, 2003; *Kim et al.*, 2007].

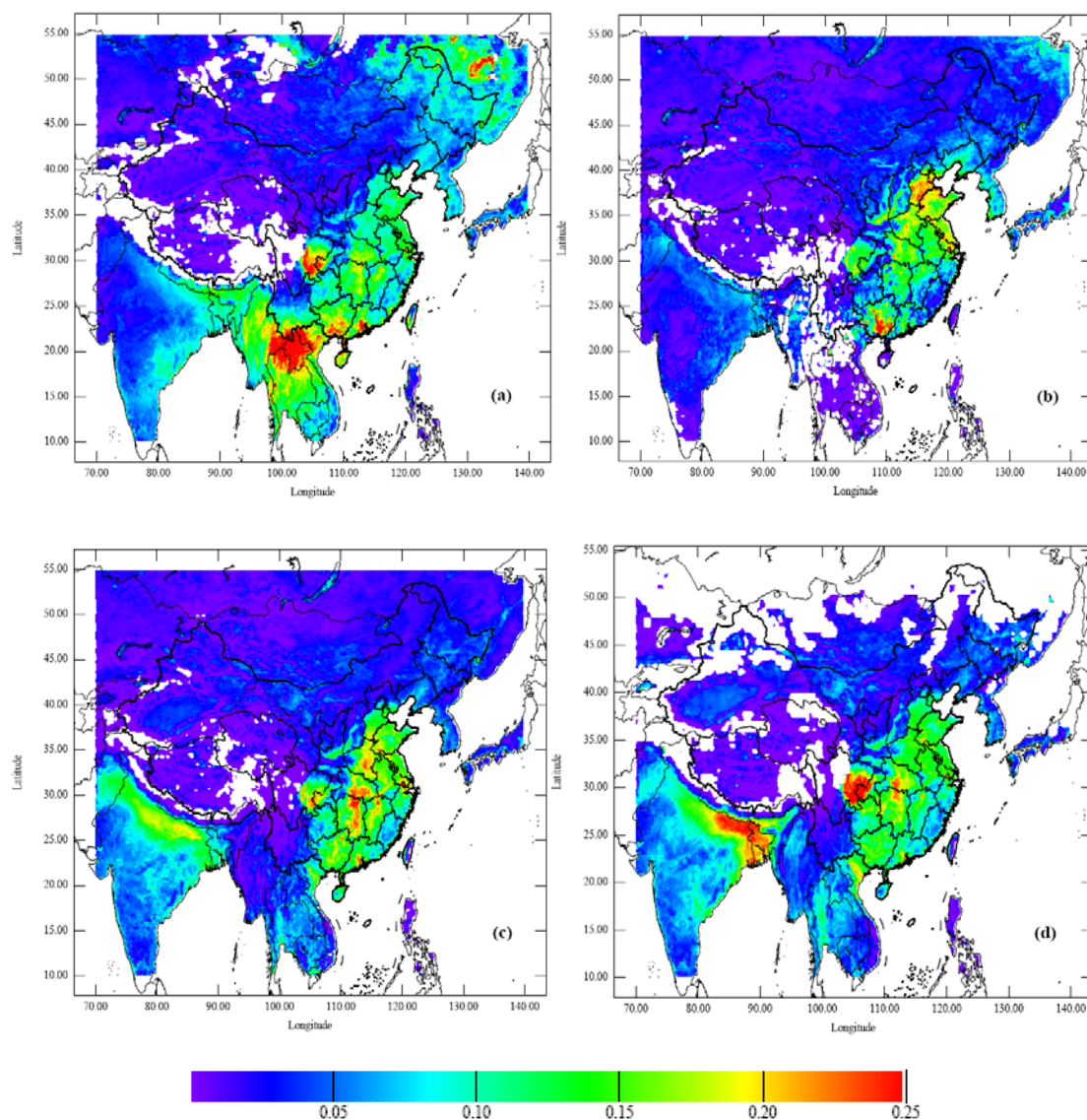


Figure 4.2: Spatial distribution characteristics of POLDER-3 AOD at 865 nm over East Asia for spring (a: MAM), summer (b: JJA), autumn (c: SON), winter (d: DJF).

In summer (Figure 4.2b), though, the AOD values significantly decrease around Sichuan Basin, we observed an increase of AOD in the eastern part of China, especially around the border of Shandong and Hebei, likely due to anthropogenic pollution. The decreasing AOD trends in the Sichuan Basin are possibly associated with the wet deposition caused by the frequent rainfall, which wash out the majority of

ambient respirable suspended particulates and shorten their lifetime. High AOD values detected in spring in Southeast Asia is barely visible in summer because of the reduced amount of aerosol retrievals resulting from the heavy cloud cover during the monsoon period. Additionally, the strong rainfall, together with the high cloud cover over Southeast Asia during summer, prevents the biomass burning and also washes out pollution. In contrast, most of southern Guangxi Province still has high AOD during this time due to the aerosol emissions from the heavy industrialized areas and the relatively stagnant conditions over this region.

In autumn (Figure 4.2c), AOD slightly increase in Eastern and Southern China, the Sichuan Basin and the region from the north part of India to the south of Himalaya Mountains, but decreases in Guangxi Province of China.

During the winter (Figure 4.2d), AOD values increase and reach their maxima in the Sichuan Basin, the north-eastern part of India along the Himalaya Mountains and Bangladesh. In the Sichuan Basin, the observed AOD increase can be explained by poor dispersion conditions and heavy local industrial and vehicle emissions. Near the base of the Himalaya Mountains in Northern India and Bangladesh, a large AOD, possibly related to the pollution accumulation due to temperature inversion in the boundary layer, is observed. During the winter, cold air flows from the mountains down to the plains making the air near the ground cooler than air above it. This probably traps aerosols from agricultural fires and cities near the ground [*Marshall et al.*, 2005; *Di Girolamo et al.*, 2004].

4. 1. 3 Results and Discussion

Based on the above analysis, we conclude that aerosol patterns detected by POLDER-3 over East Asia are clearly linked with human activities. Most of the

regions characterized by large AOD values are located in Southeastern China and Northeastern India, areas characterized by developed industries and rapid economic growth. The north part of Southeast Asia and the Stanovoy Range in Russia only exhibit a high AOD during spring, when representative aerosol emissions are dominated by biomass burning activities.

Seasonal fluctuations in POLDER-3 AOD vary between different geographical locations. For example, South Central China and the northeastern region of India along the Himalaya Mountains reach their maximum AOD during winter, while the maxima AOD in Southeast Asia and the Stanovoy Range in Russia occur during spring. The North China Plain reaches its maximum of AOD in summer, while in southern China (the middle and lower valley of the Yangtze River) the highest AOD occurs in autumn. The main factors controlling regional variability are the difference in both local emissions and seasonal meteorological conditions in the different geographical regions [Kaufman *et al.*, 2002].

4. 2 Year-by-year evolution of summer aerosol loads in North China region

In the following analysis, we investigate inter-annual AOD variation from 2003 to 2009 as seen by POLDER instruments. More precisely, our area of interest, “North China”, includes all regions of China within the limits 32°N-42°N in latitude and 110°E-120°E in longitude (Figure 4.3a), including Beijing (population 11.5 million, Figure 4.3b) and Tianjin (9.3 million) Municipalities [National Bureau of Statistics of China (NBS), 2004]. Surrounding Provinces, including Hebei, Shandong, Shanxi and Henan, which are heavily populated, urbanized and industrialized, are also included. In the areas surrounding Beijing, emission controls on stationary sources and vehicles are not as stringent as in Beijing itself, and emissions rates are therefore higher. Rural biomass burning has also been identified as an important contributor to fine PM

concentrations in Beijing [Duan *et al.*, 2004; Streets *et al.*, 2007]. Emissions from these nearby sources, as well as more distant ones, are subject to chemical reactions during transport on prevailing winds, forming secondary species that enter the entire region and are added to the local pollution of Beijing [Han *et al.*, 2005; Hatakeyama *et al.*, 2005; Luo *et al.*, 2000; Mauzerall *et al.*, 2000].

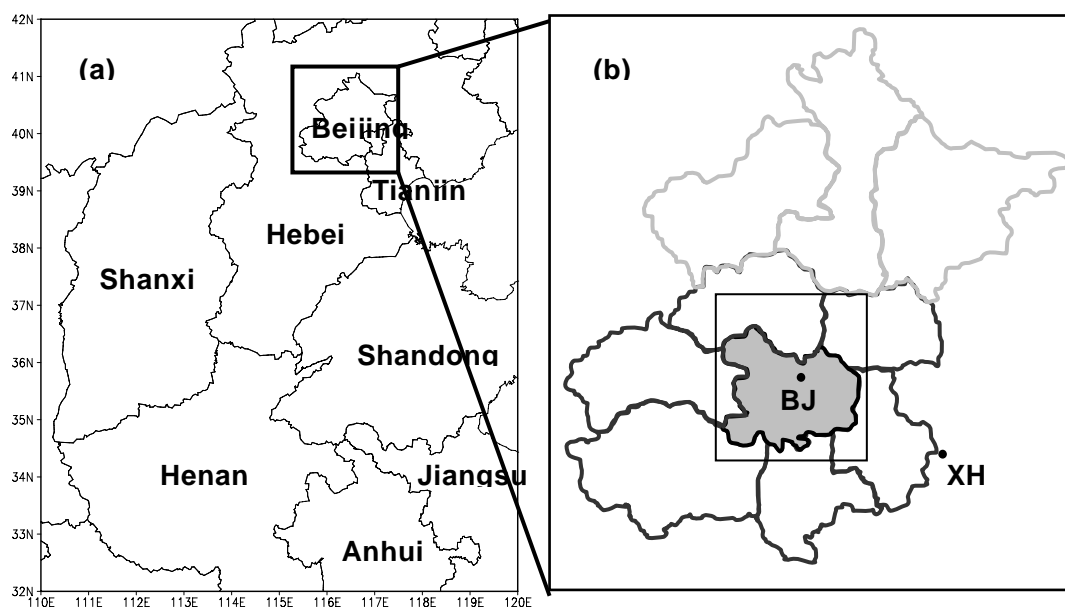


Figure 4.3: Study area referred to as “North China” in this paper (a) and the map of Beijing (b) showing main urban districts (gray shaded area), interior suburban districts (dark gray boundary), the far north districts and counties (light gray boundary) and the locations of Beijing and XiangHe sites (black points). The box in Figure 5b highlights the Beijing City defined and analyzed in this paper.

4. 2. 1 Inter-annual variability of summer aerosol loads over North China

Utilizing both POLDER-2 (2003) and POLDER-3 (2005-2009), we averaged, over the North China area, the AOD at 865 nm from June to August for each available year.

The results are presented in Figures 4.4a-f. Moreover, complementary statistical parameters such as median, mean, standard deviation, first and third quartiles, as well as the maximum and minimum, are given in Figure 4.5.

A significant inter-annual variation in AOD can be observed in both Figure 4.4 and 4.5. The maximum AOD is observed in 2003 (0.19), whereas the minimum AOD, which was roughly half of the maximum (0.10), occurred in 2006. The summer of 2008 appears to have been a moderately polluted season, and was followed in 2009 by a new minimum AOD (0.08).

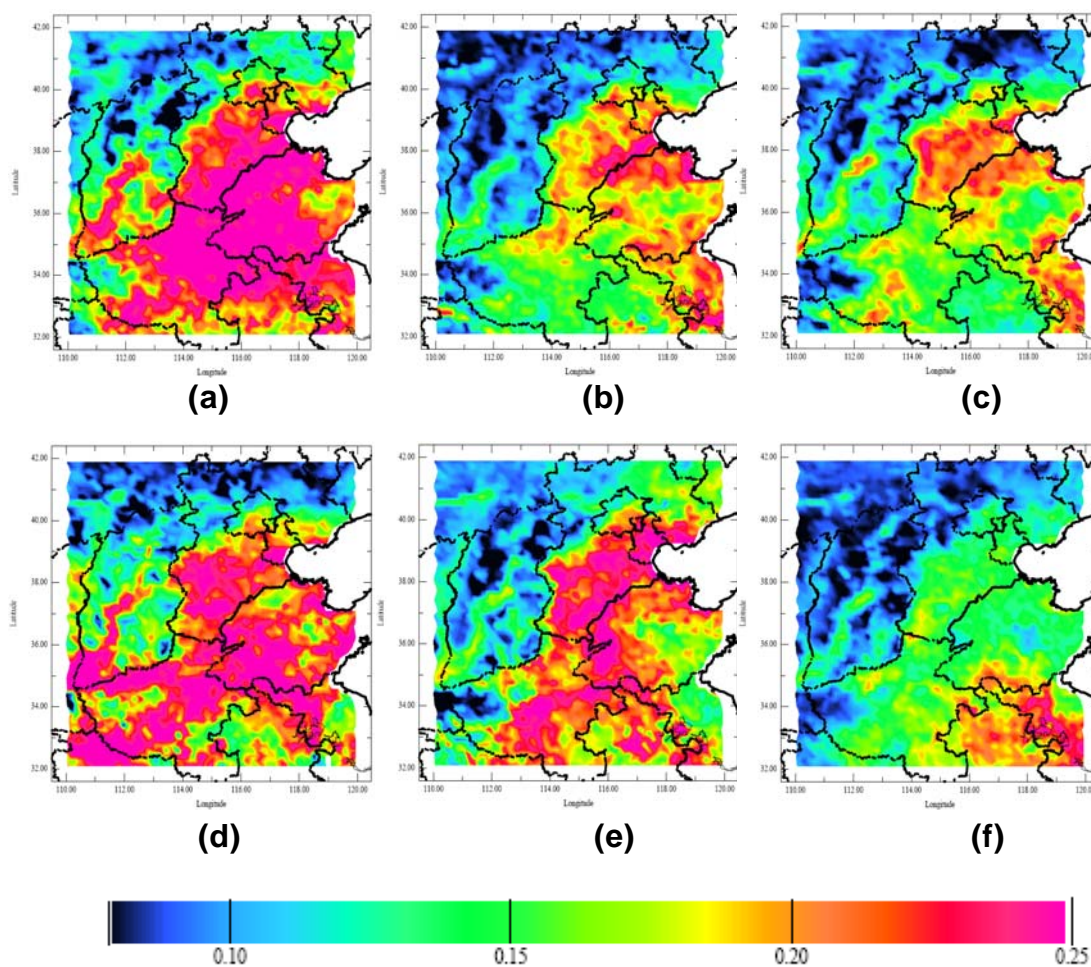


Figure 4.4: Spatial distribution characteristics of POLDER AOD at 865 nm over

North China in the summer of 2003 (a), and from 2005 to 2009 (b-f).

A similar trend was observed upon investigation of the regions covered with high AOD values (Figure 4.4a-f). During the summer of 2003, high AOD values, covering almost the entire Shandong Province, are linked with those measured over the Southern Hebei Province, Beijing and Tianjin municipality, the northeast region of Henan Province, as well as the northern Anhui and Jiangsu Province. The strip of plains in Shanxi Province between the Taihang (East) and Lüliang (West) Mountains also shows a higher AOD in the summertime. During the summers of 2005 and 2006, the area covered with AOD values greater than 0.20 decreased significantly and was mainly localized along the border of Hebei and Shandong Provinces, Tianjin municipality and the border area between Shandong and Jiangsu Provinces. However, the surface covered with higher AOD levels expands greatly into the southwest regions during the summer of 2007, indicating another heavy polluted season. In the seasons following, emission control strategies are enforced in Beijing and its surrounding Provinces to ensure better air quality for the 2008 Olympic Games. The area covered with AOD values larger than 0.20 decreased slightly in the summer of 2008 when compared to 2007. The area covered with high AOD values decreased again in the summer of 2009, where high AOD values only appeared over the north part of Anhui and Jiangsu Provinces.

Over all, our analysis indicate that the fine mode AOD in North China is quite variable with the extreme values separated by a factor of nearly 2 between years. In addition, our results suggest that the summer of 2008 was a moderately polluted season.

Furthermore, differences observed between the third and the first quartiles in Figure 4.5, as well as the standard deviations, are quite large, indicating the high level

of spatial variability of AOD.

As shown in Figure 4.4a-f, the high AOD values predominantly appear over the southeast plains of our analyzed area, where many large urban centers with dense populations and developed industries are distributed, whereas the plateau and mountains in the northwest typically exhibit AOD values lower than 0.10. The plateau and mountains with high elevations presumably restrict the spreading of aerosol pollution. The same explanation can be given for the low AOD in the northwest part of Beijing City, which contrasts with the high values in the main southeast urban regions.

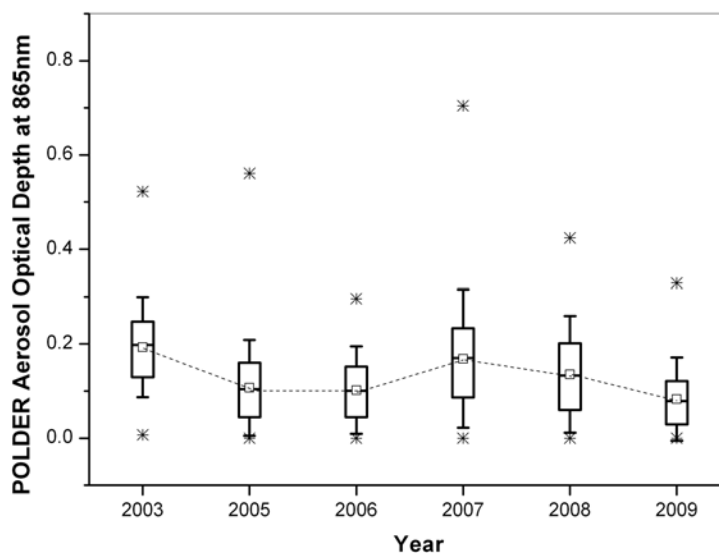


Figure 4.5: Box plots of averaged POLDER AOD at 865 nm in the summer of 2003 and 2005-2009 over North China. In each box, the central bar is the median, and the lower and upper limits are the first and the third quartiles, respectively. The error bars on the Y-axis indicate 1.5 times the spatial variation (SD). The associated maxima and minima are indicated by asterisk symbols. The square symbols indicate mean values.

To obtain a more detailed picture of the aerosol variability in North China during the summer months, we investigated the inter-annual evolutions of monthly mean of

AOD at 865 nm for June, July and August separately in Figure 4.6. Results in Figure 4.6 demonstrate that June is the month with the highest AOD value, as well as demonstrating the highest level of AOD variability. In July, the variability of AOD generally appears to be similar to that of June, but with reduced amplitude. It should be noted that AOD for both June and July start increasing in 2006 and do not decrease until 2009. In 2008, AOD for both June and July still show an increase, whereas a decreasing trend was observed for the summer as a whole, as shown in Figure 4.5. August shows a significantly different inter-annual AOD variation. The monthly mean AOD of August increases continuously from 2003 until 2008, when it appears strongly decreased. Moreover, in contrast to June and July, the mean AOD increased in August of 2009. The inter-annual contrasts observed over North China region for June, July and August can be explained by the relative contributions of complex processes such as stagnant synoptic meteorological patterns, secondary aerosol formation, hygroscopic growth of aerosols and smoke aerosols by regional biomass burning [Kim *et al.*, 2007].

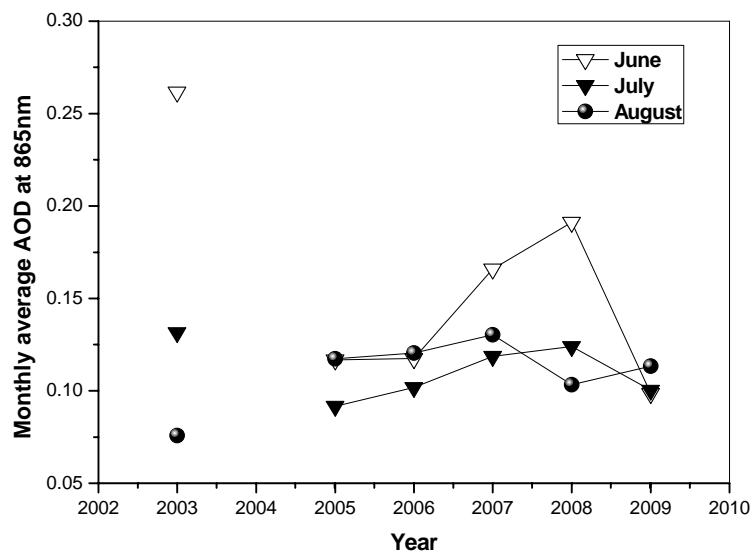


Figure 4.6: Inter-annual evolutions of monthly POLDER Aerosol Optical Depth at 865 nm in June (hollow triangle), July (filled triangle) and August (filled circle) over the whole of

North China from 2003 to 2009.

4. 2. 2 Year-by-year evolution of aerosol loads focusing on Beijing City

In this section, we focused on smaller scale analysis, specifically Beijing City, which is defined by a $0.5^\circ \times 0.5^\circ$ size area centered on the Beijing AERONET site (Latitude: 39.98° N, Longitude: 116.38° E). At this new scale of analysis, ground-based total AOD and fine mode AOD as measured and derived from AERONET data again, served as a reference (Figure 4.7).

Considering the sparse available data obtained in the summer of 2008 over Beijing site, we also include the XiangHe AERONET site (Latitude: 39.75° N, Longitude: 116.96° E), which has been in operation since 2005 and is located about 70 km southeast of Beijing. This site is classified as a rural area with respect to surface cover; however, AOD and other aerosol properties (size distribution, absorption) over the XiangHe site are nearly the same as those over Beijing site [Eck *et al.*, 2005; Xia *et al.*, 2005], though the surface properties are different. Combining these two sites enhances the reliability of our comparison. Our study area, covering the core city districts of Beijing, is highlighted with a box in Figure 4.3b, along with the locations of AERONET sites of Beijing and XiangHe. As described previously, we use AERONET level 1.5 products in order to obtain more data. The ground-based parameters plotted in Figure 4.7 result from an averaging of the XiangHe and Beijing sites. The mean AOD from each site is weighted by the number of available observation from each site.

As shown in Figure 4.7, both POLDER AOD values and ground-based fine mode AOD generally follow very similar year-to-year evolution to total AOD provided by AERONET. A very slight decrease in the fine mode AERONET AOD can, however, be

observed in 2008, whereas the POLDER-3 AOD slightly increases along with the total AOD.

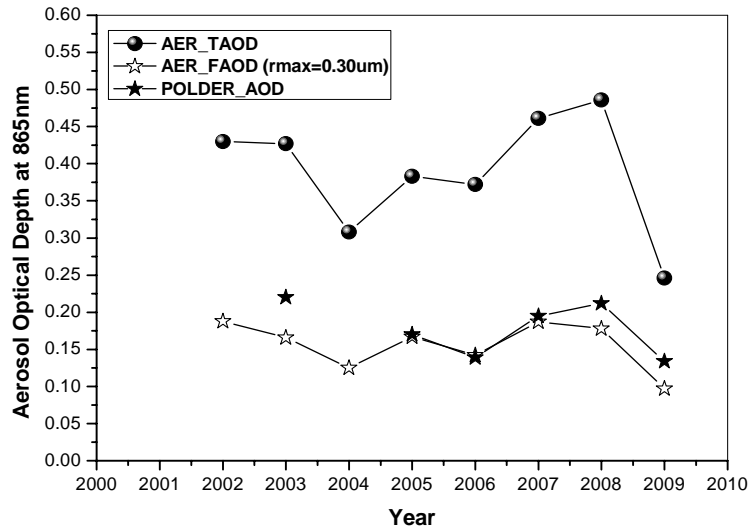


Figure 4.7: Year-to-year evolutions of AOD at 865 nm from POLDER observations (filled pentagram) and AERONET measurements around Beijing areas considering both Beijing and XiangHe ground-based sites during summer months, where the total and fine mode AOD are represented in filled circles and hollow pentagams, respectively.

The good agreement between AOD variability as detected by POLDER and ground-based one demonstrates the potential of POLDER for monitoring aerosols. Moreover, the combination of POLDER, demonstrated to be sensitive to a fraction of the fine mode aerosol, and MODIS, known to be sensitive to the entire size distribution [Remer *et al.*, 1996, 2005], could enable derivation of aerosol coarse mode optical depth, in the context of the A-Train observatory.

More detailed information for June, July and August over Beijing City are presented separately in Figure 4.8 for both total AOD and fine mode AOD. As shown in Figure 4.8, monthly POLDER AOD, as well as monthly AERONET total AOD and

fine mode AOD, varies strongly. Specifically regarding AERONET, the maximum total AOD was detected in the June of 2008, while the minimum was detected in the August of 2004 (the next is the June of 2009, more recently). The maximum fine mode AOD appeared in June 2002 (the June in 2007 next) and the minimum appeared in June 2009.

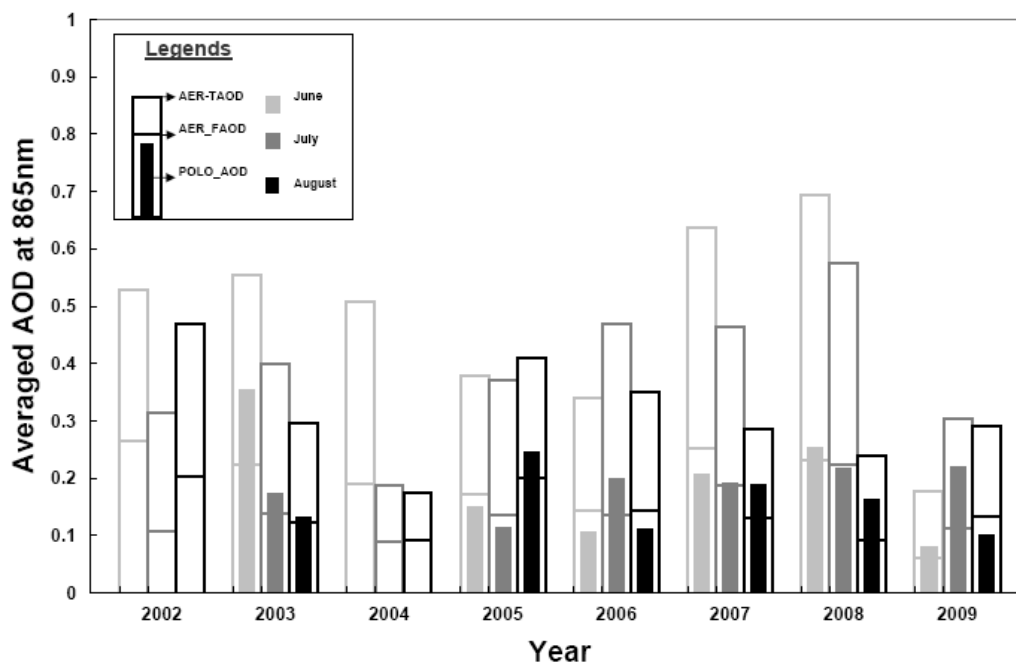


Figure 4.8 Inter-annual evolutions of monthly averaged AOD at 865 nm from POLDER (inner bar) observations in June (light grey), July (dark grey) and August (black) as well as the associated total (hollow bar) and fine mode AOD (short line) from AERONET measurements for the available years from 2002 to 2009 over Beijing City.

The lack of available POLDER data in 2002 and 2004 may partially bias the comparison of year-to-year evolution with AERONET AOD. Nevertheless, the monthly POLDER AOD in summertime showed a maximum in June 2003 and a minimum in June 2009.

However, for the fine mode AOD, the aerosol data did not show such clear pattern. Focusing on the years around the Olympic Games (2007-2009), we observed that the AERONET total AOD in August varied in a trend opposite to that of June and July. The total AERONET AOD decreased very slightly from 2007 to 2008 and then increased from 2008 to 2009. The decrease of total AOD in 2008 has also been observed with MODIS [Cermak *et al.*, 2009]. For the fine mode fraction, the agreement between POLDER and AERONET are good for June and July 2008, whereas our results show that POLDER AOD were an over estimation of the AERONET values in August. Finally, both ground-based and satellite fine mode AOD values are consistent and clearly detect the strong AOD decrease in 2009 compared to 2008.

4. 3 Conclusions

In this study, we addressed distribution and variability of aerosols over East Asia based on the POLDER-2 (2003) and -3 (2005-2009) datasets. Special attention was paid to AOD variability during summer months over North China and Beijing City.

The analysis of POLDER-3 AOD from March 2005 to February 2009 highlights the characteristics and seasonal variation of aerosol distribution over East Asia, strongly suggesting that human activities may be the main source of fine mode aerosols. Indeed, all areas with relatively high values of AOD are regions characterized by dense population and rapid growth of economic, such as Sichuan Basin, the middle and lower valley of the Yangze River, the North China Plain in China and the northern India. Significant seasonal variation of aerosol distribution was clearly observed by POLDER-3. The occurrence of high spots with heavy fine mode aerosol loads over Southeast Asia and the forest zone in Russia were found only during spring seasons. For South-Central China (*i.e.*, the Sichuan Basin) and Northeastern India along

Himalaya, the maximum AOD occurs in winter, while the maximum AOD of the North China Plain occurs in summer. However, Southern China (specifically the middle and lower valley of the Yangtze River) presents its highest AOD in autumn.

Based on six years of observations from POLDER-2 (2003) and POLDER-3 (2005-2009), we analyzed the year-to-year evolution of fine mode aerosol loads in the region of North China and Beijing City, with a special interest in the impact of emission control strategies implemented over Beijing and its surrounding areas for the 2008 Summer Olympic Games. In the North China region, the level of fine mode aerosol load observed by POLDER decrease slightly during the summer 2008 compared with 2007 and then further decrease strongly in the summer 2009. However, POLDER data showed a different variability over Beijing City during the summer of 2008, with slightly higher levels of AOD than in 2007. The most striking feature shown by the POLDER dataset for both North China and Beijing is that the lowest level of fine mode aerosol loads was recorded in the summer of 2009. This characteristic was confirmed over the Beijing area through analysis of ground-based aerosol data.

Here, we show that June is, in general, the most polluted month of the summer, and is characterized by the largest amplitude of inter-annual variations. A similar year-to-year trend is shown for July; aerosol loads in August, however, vary differently.

Finally, our analysis over East Asia demonstrates the potential of the POLDER dataset for monitoring fine mode AOD, and complements other aerosol records from both ground and space.

Chapter 5

Comparative analyses and fusion of POLDER and MODIS observations

Despite minor constituents of the atmosphere, aerosol particles play a crucial role in the climate system and the hydrologic cycle [*Ramanathan et al.*, 2001]. However, large uncertainties in the quantification of their effects remain due to their large variability in aerosol type, size, optical and chemical properties. Additionally, the short lifetime of these particles and their various origins leads to a highly inhomogeneous distribution within the atmosphere.

In order to better understand and accurately quantify the effects of aerosols, a large panel of instruments has been developed to characterize the optical and physical properties of tropospheric aerosols and their temporal and spatial distributions [*Kaufman et al.*, 2002]. Ground-based Sun photometers within the AERONET network are well suited to observe continuously the atmosphere in key locations but at coarse spatial resolution [*Dubovik et al.*, 2002b]. Only satellite observations provide daily and global measurements (typically one image per cloudless day for aerosol remote sensing sensors).

In recent decades, more and more instruments devoted to monitoring aerosols have been successfully launched such as POLDER [*Deschamps et al.*, 1994] on board ADEOS-1, -2 and PARASOL spacecrafts and MODIS [*Salomonson et al.*, 1989] on Aqua or Terra spacecrafts. Nevertheless, each instrument has its own characteristics leading to different strategies of retrieving aerosol properties and to different accuracies in these retrievals. Therefore, more information will be archived if we

integrate these different approaches, either the inter-comparison between results from different sensors [Myhre *et al.*, 2004; Gérard *et al.*, 2005; Kokhanovsky *et al.*, 2007] or using simultaneous information about aerosol provided by different instruments. POLDER and MODIS on Aqua, members of the A-Train constellation (PARASOL got off the train in December of 2009), flew in the same formation and obtain nearly the simultaneous observations. They are both developed to monitor the atmosphere by measuring the solar radiation reflected by the Earth-atmosphere system but using different techniques. POLDER perform multi-directional and polarized measurements in nine spectral channels (from 443 to 1020nm), whereas MODIS measures radiances in only one direction and with no polarization but in more spectral channels (from 415 nm to 14.235 μm). Furthermore, MODIS has a higher resolution at nadir from $250 \times 250 \text{ m}^2$ to $1 \times 1 \text{ km}^2$, depending on channel, than POLDER, which has a spatial resolution of $6 \times 7 \text{ km}^2$. This better resolution combined with the capability to perform thermal measurements results in a higher sensitivity to the presence of clouds for MODIS compared to POLDER. More information about these two instruments and their retrieval algorithms have been described in Chapter 2. Obviously, these two sensors have different advantages, which are somehow complementary, so combining POLDER multi-directional and polarized measurements with MODIS multispectral information should be particular attractive.

In this chapter, we firstly evaluated the coincident POLDER-3/PARASOL and MODIS/Aqua aerosol retrievals over land with the corresponding AERONET inversions, and then analyzed the distribution patterns of coarse mode aerosol loads as well as their seasonal variability over East Asia ($10 - 55^\circ \text{ N}$; $70 - 140^\circ \text{ E}$) by linking POLDER-3 and MODIS near pixels in time and in space.

5. 1 Data collection description and methods

Similar to the evaluation of POLDER-3/PARASOL aerosol products performed in the chapter 3, we considered level 1.5 ground-based measurements from the same 14 AERONET sites located in East Asia (Figure 3.1), including both fine mode and total AOD at 550 and 670 nm. The satellite aerosol retrievals evaluated in this chapter consist of fine mode AOD derived from POLDER-3/PARASOL and MODIS/Aqua and total AOD provided by MODIS at the same wavelengths. For the validation of satellite aerosol products, we considered the dataset from March, 2005 to June, 2008, while four whole years of POLDER-3 and MODIS aerosol retrievals (5th March, 2005 to 4th March, 2009) are combined to analyze the distribution characteristics of coarse mode aerosols. The processing procedure for the AERONET aerosol inversions has been described very thoroughly in Chapter3. Fine mode AOD ($r \leq 0.30 \mu\text{m}$) at 550 and 670 nm were computed considering the same filters and averaged within ± 30 min around satellite overpass time. Likewise, the satellite aerosol retrievals were also averaged over an area of $50 \times 50 \text{ km}^2$ centered at the AERONET sites to agree with ground measurements in space. More detailed information could be found in the chapter 3. Here, we only briefly introduce the coincidence between POLDER-3 and MODIS, which is the first step to combine the observations from these two different instruments.

For the level 2 aerosol products, POLDER-3 has a spatial resolution of $20 \times 20 \text{ km}^2$, lower than for $10 \times 10 \text{ km}^2$ MODIS. However, the combination of the two aerosol retrievals is performed by matching POLDER-3 and MODIS super-pixels both in time (± 5 min) and space. In addition, only super-pixels that are fully cloud-free at the individual pixel scale, according to the cloud screening provided by both instruments, are considered.

Regarding temporal coincidence, both platforms (PARASOL and Aqua) flew in the same A-Train formation during our study period and have very close ascending node local passing time (about 13:30 LT). PARASOL and Aqua are considered to observe nearly the same target due to the interval less than 3 min between their overpass times. So, we consider POLDER-3 and MODIS to be coincident in time. For the spatial coincidence, we project the given MODIS pixels to the POLDER reference grid according the following equations:

$$lin = NINT[6 \times (90 - lat) + 0.5]; \quad (5.1)$$

$$N_i = NINT[1080 \times \cos(lat)]; \quad (5.2)$$

$$col = NINT\left[1080.5 + \frac{N_i}{180} \times lon\right]; \quad (5.3)$$

Where lat and lon are the *latitude* and *longitude* of the given MODIS pixel, lin and col are the corresponding number of *row* and *column* of the given MODIS pixel projected in the POLDER reference grid, $NINT$ stands for *nearest integer*. All the MODIS pixels with the same number of *row* and *column* are averaged to match POLDER-3 super-pixel.

5. 2 Results and discussions

The main purpose in this chapter is to explore the potential of POLDER in atmospheric monitoring and expand the application prospect of POLDER aerosol products. Based on the results of the chapters above, POLDER is demonstrated to be sensitive to the accumulation mode aerosols and has excellent capability to characterize the distribution of fine mode aerosol loads. Knowing that MODIS is sensitive to the entire size distribution of aerosol particles [Remer *et al.*, 1996, 2005], combining POLDER-3 and MODIS observations should provide some interesting information, such as the distribution of coarse mode aerosol. In order to assure the

quality of satellite aerosol retrievals, we performed the validation of POLDER-3 and MODIS aerosol products firstly.

5. 2. 1 Evaluation of satellite aerosol retrievals

5. 2. 1. 1 Fine mode Aerosol Optical Depth at 550 and 670 nm

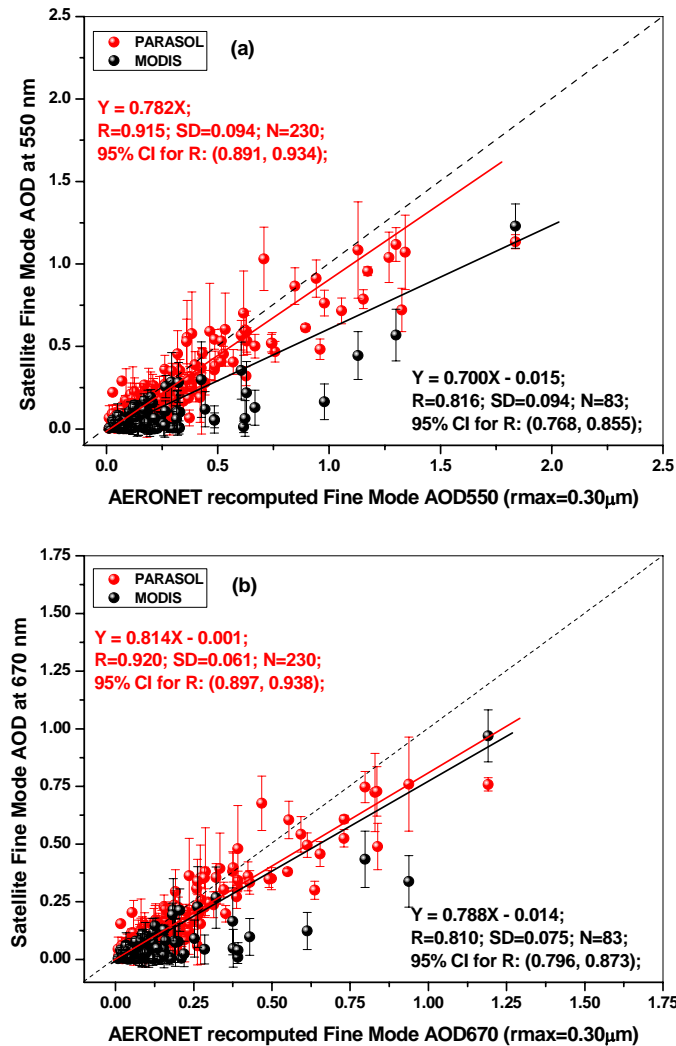


Figure 5.1 Comparisons between POLDER-3 AOD (red) and MODIS fine mode AOD (black) versus AERONET recomputed fine mode AOD ($r \leq 0.3 \mu\text{m}$) at 550 nm (a), 670 nm (b) over 14 sites located in East Asia from March 2005 to June 2008. POLDER-3 AOD at 670 and 550 nm were computed from POLDER-3 AOD at 865 nm and the

corresponding Ångström exponent. Error bars in (a) and (b) show spatial variation of POLDER pixels.

Comparisons of POLDER-3 AOD and MODIS fine mode AOD, computed from MODIS AOD and Fine mode fraction (FMF), against $\tau_{fine(r \leq 0.3 \mu m)}^{AER}$ are shown in Figure 5.1a and 5.1b respectively for 550 and 670 nm channels. The error bars on the Y-axis represent the spatial standard deviation computed over the $50 \times 50 \text{ km}^2$ size window. As demonstrated in the chapter 3, POLDER AOD shows a good agreement with $\tau_{fine(r \leq 0.3 \mu m)}^{AER}$. The correlation coefficients are 0.92, with the 95% Confidence Intervals (CI) from 0.89 to 0.93 for 550 nm and from 0.90 to 0.94 for 670 nm. The slopes, calculated by the robust regression method based on iteratively reweighted least squares, are 0.782 and 0.814 for 550 and 670 nm, respectively. The observed decrease of the slope with wavelength can very likely be explained by extrapolation validity as well as limitations in the retrieval assumptions such as departure between modeled and true absorption, particle shape and residual surface contribution.

For the fine mode AOD derived from MODIS aerosol retrievals, the results from robust regression analysis are not so good as POLDER. The correlation coefficients are about 0.81, with the 95% CI from 0.77 to 0.85 for 550 nm and from 0.80 to 0.87 for 670 nm. The slopes are 0.70 and 0.79 for 550 and 670 nm respectively. However, the number of available MODIS data is much less than POLDER-3, and most of the fine mode AOD derived from MODIS are close to 0, corresponding to the clear cases when the satellites retrievals have low reliability. Therefore, large uncertainties exist in the regression results.

In short, POLDER-3 shows a higher sensitivity to the accumulation aerosol compared to MODIS, although both POLDER-3 and MODIS underestimate the fine

mode AOD. POLDER-3 AOD seems more close to the actual fine mode AOD measured by ground-based instrument. Consequently, combining POLDER-3 with MODIS should provide more information than considering only MODIS aerosol retrievals, although it also provides the information about fine mode aerosols.

5. 2. 1. 2 Total Aerosol Optical Depth at 550 and 670 nm

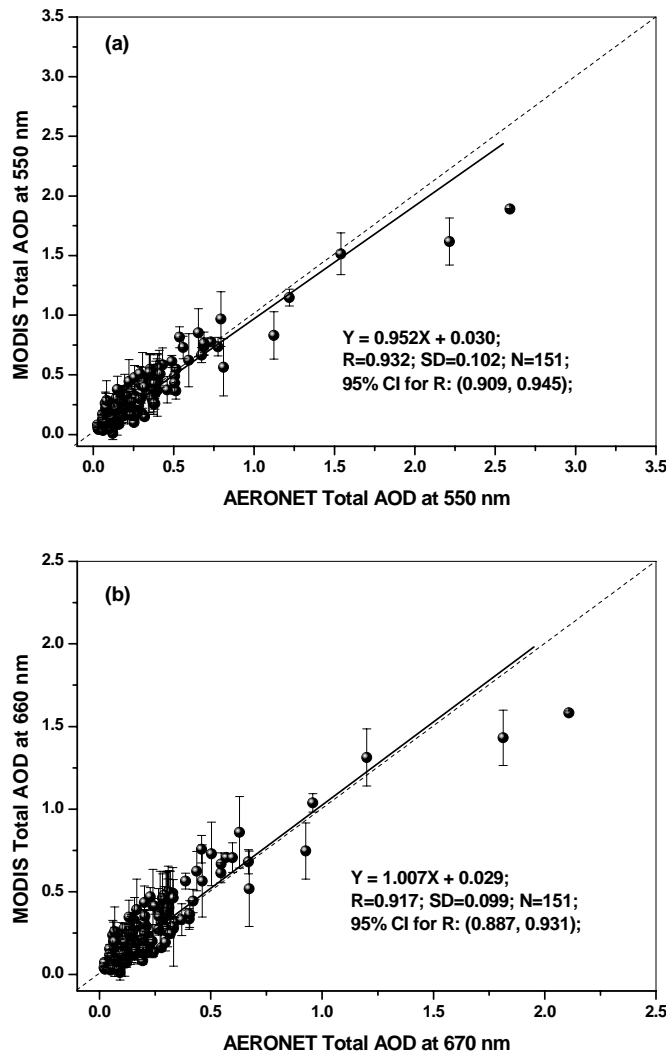


Figure 5.2 Comparisons of total AOD between MODIS and AERONET at 550 nm (a) and 660 nm (b) over 14 sites located in East Asia from March 2005 to June 2008. Error bars in (a) and (b) show spatial variation of MODIS pixels.

The correlation between MODIS total AOD and AERONET total AOD are presented in Figure 5.2. MODIS total AOD is shown to be quite coincident with AERONET measurements. The correlation coefficients are 0.93, with the 95% CI from 0.91 to 0.94, and 0.92 with the 95% CI of 0.89-0.93, for 550 and 670 nm respectively. The slopes are very close to 1 (0.95 for 550 nm and 1.01 for 670nm), indicating that MODIS has great capability to monitor the total aerosol loads.

Based on the robust regression analysis above:

$$AOD_{PAR}^{550} = 0.782 \times AOD_{AER}^{f550}; \quad (5.4)$$

$$AOD_{MOD}^{t550} = 0.952 \times AOD_{AER}^{t550} + 0.03; \quad (5.5)$$

5. 2. 2 Combination of POLDER-3 and MODIS observations

Based on the evaluation of satellites aerosol retrievals over land in the last section, we computed coarse mode AOD and fine mode fraction (Equation 5.6 and 5.7) from POLDER-3 and MODIS aerosol retrievals and analyze the distribution patterns of coarse mode aerosols, as well as their seasonal variability, considering satellite aerosol products of four years (03/05/2005 – 03/04/2009). The coarse mode AOD and the fine mode fraction are defined as followed:

$$AOD_{coarse}^{550} = AOD_{MOD}^{t550*} - AOD_{PAR}^{550*} = AOD_{MOD}^{t550} / 0.952 - AOD_{PAR}^{550} / 0.782; \quad (5.6)$$

$$Ratio_{fine}^{550} = \frac{AOD_{PAR}^{550*}}{AOD_{MOD}^{t550*}} = \frac{AOD_{PAR}^{550} \times 0.952}{AOD_{MOD}^{t550} \times 0.782} = 1.217 \times \frac{AOD_{PAR}^{550}}{AOD_{MOD}^{t550}}; \quad (5.7)$$

Where AOD_{PAR}^{550*} and AOD_{MOD}^{t550*} stand for the corrected fine mode AOD retrieved by POLDER and the total AOD from MODIS respectively.

Besides the satellite aerosol retrievals over land, we also considered the aerosol

retrievals over ocean (fine mode AOD from POLDER and total AOD from MODIS). Generally, remote sensing of aerosol is more accurate and informative over ocean due to the dark and uniform reflectance (except glint area). Therefore, we computed the coarse mode AOD and fine mode fraction over ocean according to Equations 5.6 and 5.7, assuming that the satellite aerosol retrievals over ocean have the high quality as the ones over land. Furthermore, some pixels appear with larger corrected POLDER-3 AOD than the corrected MODIS AOD probably due to the retrieval errors or corresponding to the cases dominated by fine mode aerosols. Such pixels are rejected when we make average of multi-year satellite observations.

5. 2. 2. 1 Spatial distribution patterns of coarse mode aerosols and the fine mode fraction

In order to provide an overview of the aerosol loads distribution over this very large region, we compute four-year average of POLDER-3, MODIS AOD and the difference between the corrected satellite retrievals (the coarse mode AOD) at 550 nm. The results are shown in Figure 5.3a, 5.3c and 5.3e, respectively. In the mean time, information on the percentage of days with available POLDER-3 and MODIS aerosol retrievals is also given in Figure 5.3b and 5.3d. Moreover, a four-year averaged Fine Mode Fraction (the ratio of corrected POLDER-3 AOD to the corrected MODIS AOD) is also presented in Figure 5.3f. Percentages lower than 100% in Figure 5.3b and 5.3d are due to cloud cover (e.g., the whole area, especially Southeast Asia and the southern part of China), to topographic features of the underlying surface (e.g., the Tibetan Plateau) or to missing data (the white color in the inland areas). However, a clear difference is indicated in the regions of Xinjiang and Qinghai when comparing Figure 5.3b with 5.3d. For POLDER, this region has more available data compared to other regions, while no MODIS aerosol products are retrieved over these regions. It is

probably related to the different retrieving principle of these two instruments.

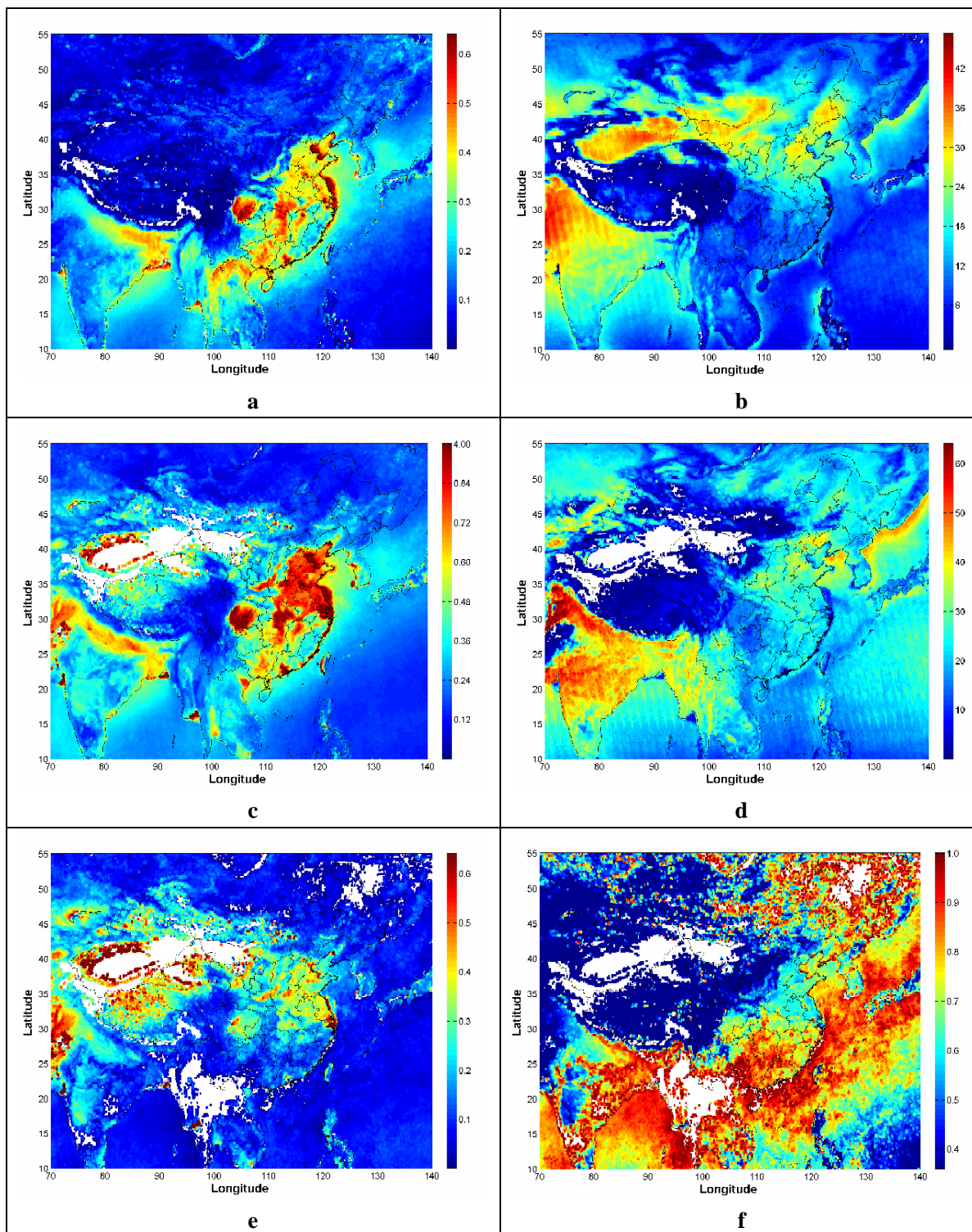


Figure 5.3 Map of averaged AOD at 550 nm from POLDER-3 (a) and MODIS (c) and

the corresponding pixel frequency based on POLDER-3 (b) and MODIS (d) observations over a four-year period (March 2005-March 2009). The frequency is calculated as the number of days with successful PARASOL aerosol retrievals in clear sky divided by the total number of calendar days during the study period. (e) and (f) show the distribution of coarse mode aerosol and fine mode fraction, respectively.

The relatively homogeneous surfaces (desert or sandy land) contribute little to the polarized reflectance. They are advantageous to the POLDER aerosol retrieving, combined with frequent cloudless sky over these regions. However, the high reflectance of these bright surfaces makes the aerosol retrieving from MODIS a difficult task.

In addition, locations of several typical areas mentioned below are the same as the ones marked in Figure 4.1c in chapter 4.

Similar characteristics are shown in Figure 5.3a by the averaged POLDER-3 AOD at 550nm, compared to Figure 4.1a, which presents the spatial distribution of averaged POLDER-3 AOD at 865nm during the same study period. The highest average AOD mostly appears in the Sichuan basin and the south-eastern region of China, particularly around the middle and lower valley of the Yangtze River, the Delta of the Pearl River and the North China Plain which are densely populated, highly industrialized and economically developed. Additionally, there are also several other areas with high AOD value, such as the south-Himalaya region in India and the areas around the border between China and Laos. According to our study, the maximum of POLDER-3 AOD value at 550 nm over East Asia has been estimated as 1.05; whereas, the mean value is 0.14. Excluding the very clear regions over the Tibetan Plateau and the north-west part of East Asia which are beyond the scope of this study, the low AOD values primarily appear over Northeast China, including Heilongjiang (HLJ), Jilin (JL)

Province and inner-Mongolia (IM).

Averaged MODIS AOD at 550 shows some different characteristics in Figure 5.3c, although its pattern looks alike substantially. Besides the regions with high AOD in Sichuan Basin and the south-eastern region of China, especially Shandong Province and its surround provinces, some high values of MODIS AOD also appear in the Taklimakan Desert of Xinjiang (XJ), the western part of Tibet, the Qaidam Basin in Qinghai Province (QH) and the Thar Desert in Pakistan and the west of India, although the central area of these regions have less available data due to the bright surface. Such features have also been highlighted by *Li et al.* [2003] and *Luo et al.* [2001]. According to the Figure 5.3e, these regions are dominated by the coarse mode aerosol, in terms of dust aerosols, which exceed the sensitivity of POLDER. Likewise, there are also some regions with high POLDER AOD, but not be highlighted by MODIS, such as the areas around the border between China and Laos in Southeast Asia. Referring to the Figure 5.3e and 5.3f, a new blank appears in this area resulting from rejecting the pixels with larger corrected POLDER-3 AOD than the corrected MODIS AOD. It means that the POLDER-3 AOD in this region is extremely close to the MODIS AOD, maybe a little larger due to the retrieval errors. Namely, fine mode aerosols are absolutely dominant in this region. Another similar case appears in the Northeast of China. Statistically, there are 8.03% of pixels are rejected because of the larger corrected POLDER-3 AOD than the corrected MODIS AOD. Some of these pixels are associated with the cases dominated by fine mode aerosols, without ruling out some cases induced by only retrievals errors.

As shown in Figure 5.3e and 5.3f, coarse mode aerosol always distribute in the deserts and sand lands, such as the Taklimakan Desert of Xinjiang (XJ), the western part of Tibet, the Qaidam Basin in Qinghai Province (QH) and the Thar Desert in Pakistan and the west of India. Additionally, some areas around Shandong Province in

the east of China also exhibit high values of coarse mode. In contrast, fine mode aerosols generally appear in the southeastern and northeastern of China, India and Southeast Asia, as well as the areas around the sea-land interface, such as the Bay of Bengal, East Sea and South Sea. Therefore, we deduce that the coarse mode aerosols mostly originate from the natural sources, such as deserts, while the fine mode aerosols are mainly produced from the anthropogenic sources, and could probably transfer to the sea areas. Moreover, the fine mode aerosols emitted from population center in East Asia Dominates the averaged aerosol optical influence over most areas (the fine mode fraction above 0.8), including the sea areas around the sea-land interfaces in our study regions.

Regarding to the aerosol retrievals over ocean, good continuities of satellite retrieved AOD are shown in Figure 5.3a, 5.3c, 5.3e, and 5.3f. Compared to other sea areas, the regions around the sea-land interface generally exhibit heavier aerosol loads, especially the bay areas. As shown in Figure 5.3f, the fine mode fraction is up above 0.9 around the sea-land interfaces. It implies that the dominative particles over these areas are the anthropogenic aerosols (fine mode) transferred from the inland areas, rather than the sea salts (coarse mode) originated from the sea areas.

5. 2. 2. 2 Seasonal variation of coarse mode AOD over East Asia

In order to acquire more information and characterize aerosol loads more precisely, an examination of the seasonal variation of aerosol patterns is presented in Figure 5.4 in which the four seasons: spring (a-c: MAM), summer (d-f: JJA), autumn (g-i: SON), and winter (j-l: DJF) are separated. The white color in the inland regions again represents areas in which the valid retrievals were not obtained.

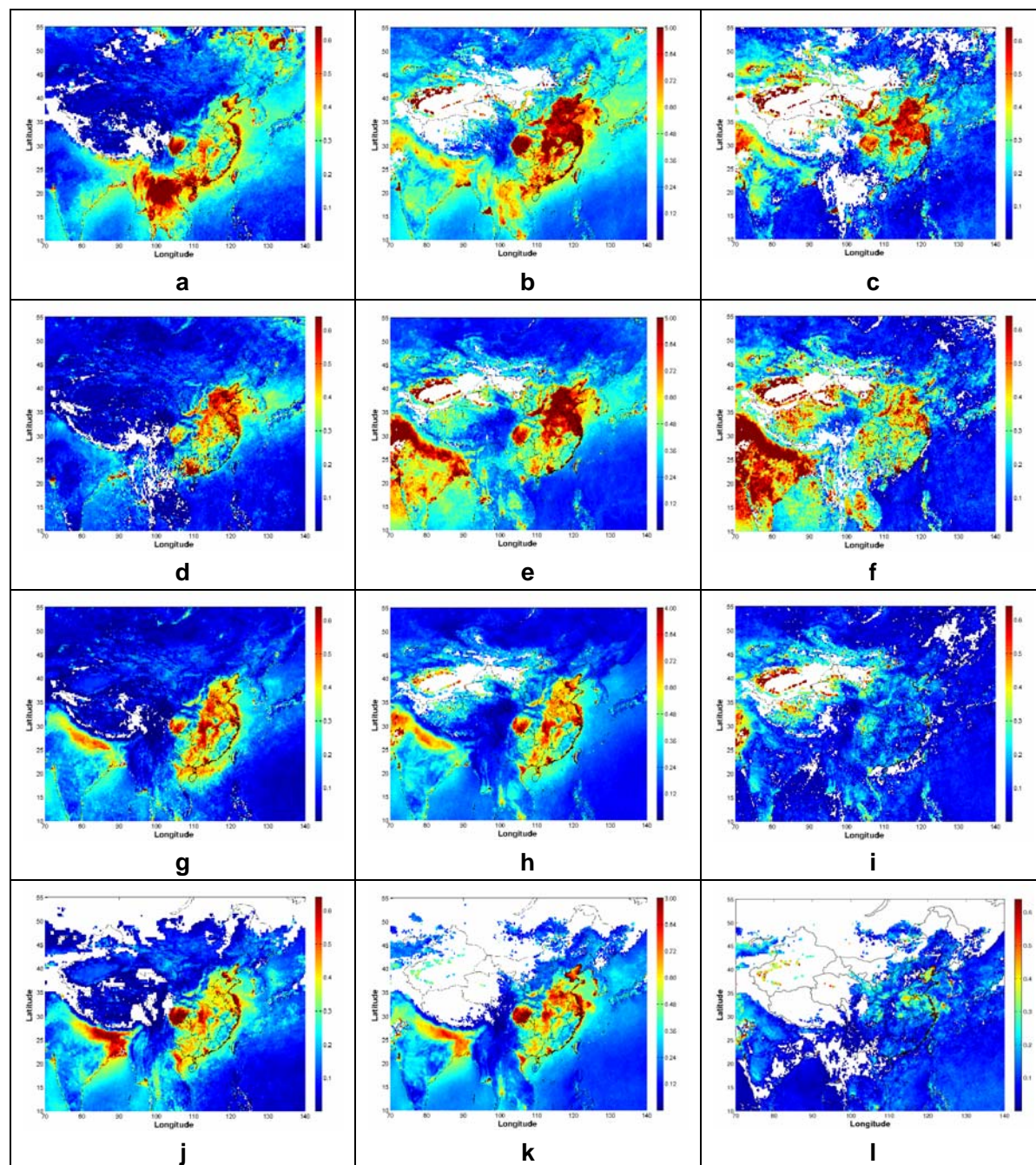


Figure 5.4 Spatial distribution characteristics of POLDER-3(a-d-g-j), MODIS (b-e-h-k) and coarse mode AOD (c-f-i-l) at 550 nm over East Asia for spring (a-c: MAM), summer (d-f: JJA), autumn (g-i: SON), winter (j-l: DJF).

The three columns (a-d-g-j, b-e-h-k and c-f-i-l) show the characteristics of aerosol loads derived from POLDER-3, MODIS, and the combination of these two sensors,

corresponding to fine mode, total and coarse mode aerosols, respectively. The extra blanks in the map of coarse mode aerosols (Figure 5.4c, -f, -i, -l), compared to the map of fine mode and total aerosols, are attributed to the rejection of the pixels with larger corrected POLDER-3 AOD than MODIS. The percentages of the rejected pixel for spring (Figure 5.4c), summer (Figure 5.4f), autumn (Figure 5.4i) and winter (Figure 5.4l) are 11.76%, 4.99%, 10.5% and 15.92%, respectively. Generally, such blanks mainly appears clearly in the Southeast Asia and the northeast of China, probably related to the extreme cases of fine mode aerosols, such as biomass burning [Kim *et al.*, 2004; Murdiyarso *et al.*, 2007; Padoch *et al.*, 2007; Damoah *et al.*, 2004; Lee *et al.*, 2005; Kanaya *et al.*, 2003]. Nevertheless, some of pixels are rejected because of the larger retrieval uncertainties of these two sensors, as described in the last section.

Seasonal variability of small particles represented in Figure 5.4a, 5.4d, 5.4g and 5.4j by POLDER-3 is very coincident with the description in the chapter 4. Similar to POLDER-3 AOD₈₆₅ in Figure 4.2, POLDER-3 AOD₅₅₀ exhibits seasonal fluctuations varying between different geographical locations. For example, the maxima AOD₅₅₀ in Southeast Asia and the Stanovoy Range in Russia occur during spring, the northeastern region of India along the Himalaya Mountains reaches their maximum AOD during winter. The North China Plain reaches its maximum of AOD in summer, while in southern China (the middle and lower valley of the Yangtze River) the highest AOD occurs in autumn. Over all, heavier aerosol loads (fine mode) seems to always appear in the southeastern of China, the region with dense population and developed economy compared to the other areas of China. The main factors controlling regional variability are the difference in both local emissions and seasonal meteorological conditions in the different geographical regions [Kaufman *et al.*, 2002].

As shown in Figure 5.4b, -e, -h, -k, total AOD₅₅₀ derived from MODIS generally present a similar distribution patterns as POLDER-3 AOD (Figure 5.4a, -d, -g, -j) in

different seasons in the southeastern of China. However, the deserts or sand lands in the Xinjiang of China always exhibit the higher values of total AOD throughout the year, which is not highlighted by POLDER-3. Furthermore, MODIS detect a heavy aerosol loads in India in summer (Figure 5.4e), while POLDER-3 present the lowest value of AOD in this region (Figure 5.4d) compared to the other three seasons. Additionally, the regions with high POLDER-3 AOD values in the Southeast Asia in Figure 5.4a is not highlighted in the map of MODIS AOD in spring (Figure 5.4b). The differences between the maps of POLDER-3 and MODIS AOD are mainly caused by the different characteristics of these two instruments and their retrieval algorithm. Referring to the distribution of coarse mode aerosols (Figure 5.4c, -f, -I, -l), we deduce that the heavy aerosol loads in Xinjiang throughout the year and in India in summer are mainly dominated by coarse mode aerosols, such as dust particles. The high values of POLDER-3 AOD in the Southeast Asia in spring are attributed to the fine mode aerosols, such as biomass burning, as explained in the last section.

For the coarse mode aerosols, Figure 5.4c,-f, -i, and 5.4l show the seasonal variability of the spatial distribution patterns clearly. In the view of the whole study area in this thesis, the heaviest coarse mode aerosol loads appear in summer, while the northern China exhibits the highest AOD (above 4.0) in spring. Generally, the coarse size-related particle nomenclature is connected to particle source processes. Unlike the fine particles below roughly 1 μm , which are mainly secondary in nature or result from combustion process, the coarse particles with diameters large than 1 μm are mainly primary in nature and result from the surface of the Earth (sea, land, and vegetation). In the case of China (especially the North China), some studies showed that the mineral dust transported from the Gobi Desert and Taklimakan Desert is a dominated source for coarse mode aerosol, occurring during spring and fall [Sun *et al.*, 2004; Zhang *et al.*, 2006]. Moreover, spring has been demonstrated to be the season with

most frequent dust storms in China, making up to more than 80% of the annual dust storm frequency [Liu *et al.*, 2004; Goudie and Middleton, 1992; Littmann, 1991; Qian *et al.*, 2002; Xuan *et al.*, 2000; and Zhang *et al.*, 1997]. Therefore, we deduce that China, precisely in North China, presents the highest AOD of coarse mode aerosols in spring (Figure 5.4c) mostly due to the contribution of the mineral dust transported from the deserts or sandy lands in the northwestern of China. Additionally, summer is shown to be the season with the second highest frequency of dust in China [Wang *et al.*, 2007; Huang *et al.*, 2007], and this can partially explain the relatively higher coarse mode AOD appearing in summer over China (Figure 5.4f). As for the heavy coarse mode aerosol loading distributing throughout the India in summer, we can attribute it to the highest frequency of dust storms occurring in Indo-Gangetic basin in monsoon season, when dusts are transported by southwesterly summer winds from the western Thar Desert [Sikka, 1997; Dey *et al.*, 2004]. In autumn and winter, most areas exhibit less heavy loads of coarse mode particles, except the deserts or sand lands such as Taklimakan Desert in Xinjiang and Thar Desert in western India and eastern Pakistan.

Regarding to the aerosol retrievals over ocean, we firstly observe good continuities of the fine mode, total and coarse mode AOD. The areas around the sea-land interface always exhibit the higher values of POLDER-3 and MODIS AOD, except in summer. These higher AOD values are related to the transfer of aerosol loads from the inland, while the lower AOD in the sea areas around the southeast coast of China is probably attributed to the East Asian Monsoon, which affects China and blows from southeast to northwest in summer. Moreover, combined with the maps of POLDER-3 and MODIS AOD, the low values of coarse mode aerosols (Figure 5.4c, -f, -I, -l) over the sea areas along the southeast coast of China in spring, autumn and winter, demonstrated that the aerosol loads in these areas are dominated by anthropogenic aerosols originated from the inland areas.

5. 3 Conclusions

Both of POLDER and MODIS have excellent capabilities to monitor the aerosol loads, although these two instruments have their own characteristics. In this chapter, we firstly evaluate the fine mode AOD from POLDER-3 and MODIS, as well as the total MODIS AOD at 550 and 670 nm by comparing them with the coincident AERONET inversions. The good agreements demonstrated the high sensitivities of POLDER and MODIS to the fine mode fraction and the entire size distribution separately.

Based on the results of robust regression, we define the correction factors for both of POLDER and MODIS AOD, and then analyze the spatial distribution patterns of coarse mode aerosol loads, as well as their seasonal variability, by combining the corrected POLDER and MODIS AOD over land and ocean. Considering four years of POLDER-3 and MODIS aerosol retrievals, we acquire the maps of averaged AOD at 550 nm derived POLDER-3, MODIS, as well as the coarse mode AOD and the fine mode fraction. The spatial distribution patterns of aerosol loads are shown to be very close related with aerosol types and their sources. Fine mode aerosols detected by POLDER generally concentrate in the areas with dense populations or the developed industries, which indicate that fine mode aerosols mostly originate from the anthropogenic sources over East Asia. In contrast, the distribution of coarse mode particles, derived as the difference between the corrected POLDER-3 and MODIS AOD, is mainly associated with the natural sources, besides the human activities. The following analyses of seasonal variability of aerosol loads also provide the similar results.

Concluded from the analyses in this chapter, both POLDER and MODIS show excellent capabilities in monitoring aerosol loads, although they are sensitive to

different fractions of size distribution. Combining the observations from these two instruments provides some information interesting and is helpful for us to distinguish fine and coarse mode aerosol loads and determined their probable sources. Some further researches could be done in this direction.

Chapter 6

Feasibility study of air quality remote sensing from POLDER observations

Atmospheric aerosols also called Particulate Matter (PM) affect the Earth's radiative balance by interacting with the solar and thermal radiation [Anderson *et al.*, 2003]. Aerosols, especially fine particle matter (PM_{2.5}, with diameters less than 2.5 μm), also reduce the visibility and induce respiratory diseases when the submicron sized aerosols penetrate the lungs thereby affecting air quality and health [Krewski *et al.*, 2000]. Additionally, health effects associated with particle exposure has shown no apparent threshold at lower concentration [Smith *et al.*, 2002]. Therefore, monitoring aerosol particles has caused an increasing concern in the world during recent years.

Several ground measurement networks have been established to monitor aerosols for different purpose including AERONET [Holben *et al.*, 2001] and the interagency Monitoring of Protected Visual Environment (IMPROVE) network [Malm *et al.*, 1994]. Most of these networks provide continuous measurements well calibrated, but they are limited in space scales, especially when the pollution is induced by the long-range transport of aerosol pollutants. In contrast, satellite remote sensing, which provide reliable repeated measurement with large spatial coverage, has already been demonstrated to be well suit for a daily monitoring of the aerosol loads and their transport patterns [Kaufman *et al.*, 2002; King *et al.*, 1999; Chu *et al.*, 2003]. Aerosol Optical Depth (AOD) retrieved by satellite can be proportional to PM when the vertical profiles and aerosol types are relatively stable. Many previous studies estimated PM_{2.5} concentrations from satellite observations based on the relationship

established between the ground-level $PM_{2.5}$ concentration and total column Aerosol Optical Depth [Chu *et al.*, 2003; Wang and Christopher, 2003; Liu *et al.*, 2005]. Motivated by this, some other studies [Liu *et al.*, 2004; Van Donkelaar *et al.*, 2006; Choi *et al.*, 2009] successfully estimated ground-level $PM_{2.5}$ mass concentration via the combination of a global chemical transport model and satellite-based AOD data in a cost-effective manner. POLDER, a new generation of polarimeter providing multi-spectral, multi-directional and polarized measurements, has been proved sensitive to the small particles with radii less than $0.30\ \mu\text{m}$ and to have an excellent capability in aerosol monitoring. Kacenelenbogen *et al.* [2006] has successfully defined a threshold for the air quality category (AQC) assessment and presented a map of $PM_{2.5}$ concentration over France estimated from POLDER-2 satellite data.

In this chapter, we attempt to estimate AQC over China, precisely over Beijing and its surrounding provinces (limited by the $PM_{2.5}$ concentration data we can acquire) from POLDER aerosol retrievals. We investigate the capability of POLDER measurements in assessing air quality and emphasize that many factors might affect the estimation accuracy. Finally, the diurnal variation of $PM_{2.5}$ concentration and aerosol vertical distribution from CALIOP space-borne lidar aboard CALIPSO are briefly analyzed preparing for possible improvements in the further study in coming days.

6. 1 Dataset description and methods

The data used in this study includes the POLDER-3/PARASOL AOD (Level 2) over land, Aerosol layer height with a vertical resolution of 60 m from CALIOP/CALIPSO, and particulate matter data collected at 10 sites in the North China, precisely over the provinces around Beijing (Figure 6.1). The $PM_{2.5}$ mass concentrations are measured using the Tapered-Element Oscillating Microbalance (TEOM) instrument with an accuracy of $\pm 5\ \mu\text{g m}^{-3}$ for 10 minute-averaged data and

$\pm 1.5 \mu\text{g m}^{-3}$ for hourly averages. The operational principle of this instrument has been introduced in Chapter 2. Three different kinds of particulate matter data are available depending on the different sites and periods. Some geographical information about the $\text{PM}_{2.5}$ monitoring sites and their available data types, as well as the corresponding time range, are presented in Table 6.1. The blue bars in the fourth column correspond to the 10-minute averaged data, while the violet bar stands for the daily averages and the orange bar corresponds to the hourly averages.

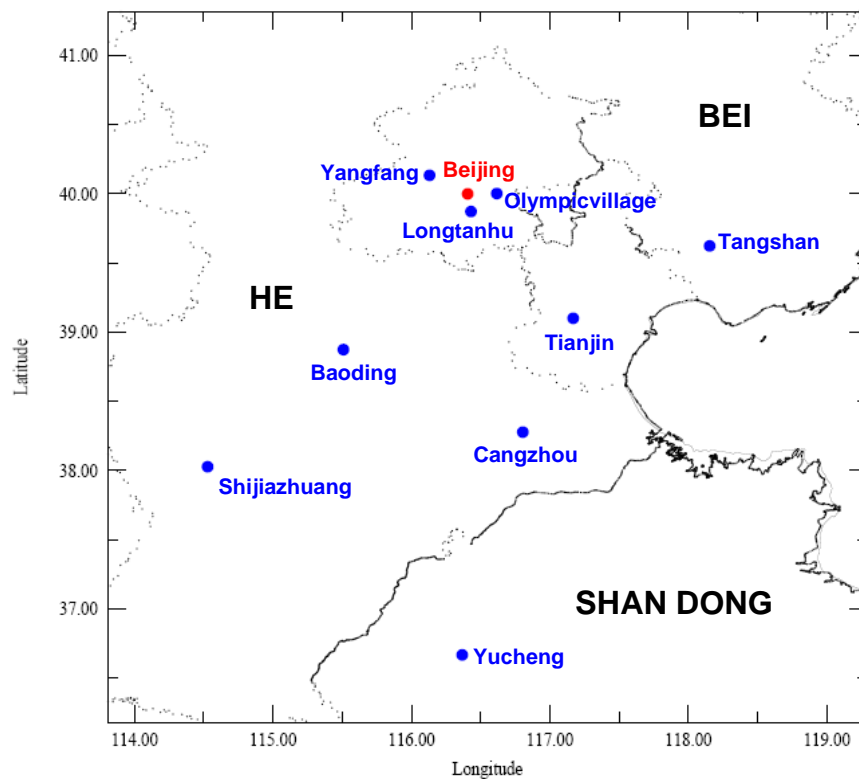


Figure 6.1 Study area with locations of the 10 $\text{PM}_{2.5}$ sites over Beijing and its surrounding area.

The POLDER-3 AOD at 440 nm considered in this chapter is extrapolated from the retrievals at 865 and 670 nm, and averaged over an area of $0.5^\circ \times 0.5^\circ$ centered in the $\text{PM}_{2.5}$ monitoring sites to match it with ground-based $\text{PM}_{2.5}$ measurements. According to the results of the evolution of POLDER aerosol retrievals over land in

Chapter 3, POLDER AOD at 440 nm is very coincident with fine mode AOD (radius less than 0.30 μm) from AERONET inversions (correlation coefficient $R=0.91$), although with an underestimation of 30%. Here we consider the shorter wavelength of 440 nm, rather than 670 and 865 nm, mainly because of its higher sensitivity to small particles.

Table 6.1 Geographical information of $\text{PM}_{2.5}$ monitoring sites considered in this study and the distribution of the available $\text{PM}_{2.5}$ data, where the blue bars correspond to the 10-minute averaged data, the violet bar corresponds to the daily averages and the orange bar corresponds to the hourly averages.

Site	Latitude, Longitude ($^{\circ}$ N, $^{\circ}$ E)	Elevation (m)	Time Period					
			20050305	20070801	20071014	20071231	20090501	20100525
Baoding	38.9, 115.5	25		Blue bar				
Beijing	39.6, 116.2	50	Violet bar				Orange bar	
Cangzhou	38.3, 116.8	15		Blue bar				
Longtanhu	39.9, 116.4	42		Blue bar				
Olympicvillage	40.0, 116.4	41		Blue bar				
Shijiazhuang	38.0, 114.5	70		Blue bar				
Tangshan	39.6, 118.2	35		Blue bar				
Tianjin	39.1, 117.1	7		Blue bar				
Yangfang	40.1, 116.1	58		Blue bar				
Yucheng	36.7, 116.4	37		Blue bar				

According to Table 6.1, the continuous and long time-ranged measurements are only provided over Beijing site (March 2005—31st December, 2007 and 1st May, 2009— 25th May, 2010). Hence we firstly examine the monthly variation and year-by-year evolutions of $\text{PM}_{2.5}$ and POLDER AOD at 440 nm in different seasons using the co-located dataset covering about four years over Beijing site. Then, we explore the relationship between POLDER-3 column AOD and 24 hourly mean $\text{PM}_{2.5}$ concentrations measured at the surface considering all the available data over ten

locations listed in Table 6.1. Finally, we discuss the factors that affect the correlation between satellite-derived AOD and $PM_{2.5}$ mass, and especially analyze the diurnal variation of $PM_{2.5}$ concentration and aerosol vertical distribution over East Asia from CALIOP/CALIPSO.

6. 2 Results and Discussions

Aerosol Optical Depth (AOD) is a measure of atmospheric extinction through a vertical column of atmosphere as seen by the space-borne sensors. Generally, a higher AOD value indicates higher column aerosol loading and therefore low visibility. In contrast, $PM_{2.5}$ mass is indicative of the mass of dry particles near the surface, which is also related to the aerosol loading and used to evaluate air quality. Significant temporal correlation between the ground –level $PM_{2.5}$ concentration and total column AOD has been demonstrated by many previous studies [*Chu et al.*, 2003; *Wang and Christopher*, 2003; *Liu et al.*, 2005]. In this section, we compare the variations of $PM_{2.5}$ and satellite-derived AOD on various time scales (monthly, seasonal and yearly) and then establish a relationship between these two parameters in order to explore the potential of using POLDER AOD product for air quality studies.

6. 2. 1 Monthly variation and year-by-year evolutions of POLDER AOD and $PM_{2.5}$ in different seasons over Beijing sites

Figure 6.2 shows the monthly mean distribution of $PM_{2.5}$ and POLDER AOD for the periods 05/03/2005—31/12/2007 and 01/05/2009—25/05/2010 over Beijing site. On the whole, monthly mean $PM_{2.5}$ concentration is always above $50.0\mu\text{g}\text{m}^{-3}$ in the twelve months. According to the standard of air quality category (AQC) defined by United States Environment Protection Agency (EPA) (Table 6.2), the AQC over Beijing is worse than moderate, on average, throughout the year. The $PM_{2.5}$ has peak

values of $76.04\mu\text{gm}^{-3}$ during winter (DEC-JAN-FEB), and has the smaller values of around $52.22\mu\text{gm}^{-3}$ in spring (MAR-APR-MAY) and autumn (SEP-OCT-NOV). Summer (JUN-JUL-AUG) exhibits the second highest $\text{PM}_{2.5}$ values of $69.15\mu\text{gm}^{-3}$ in July. The monthly mean POLDER AOD at 440 nm varies in a slightly different pattern. The highest AOD value appears in summer (0.74 in August), while the lowest AOD presented in winter (0.41 in December).

Table 6.2 AQI and its Corresponding 24 hourly Mean $\text{PM}_{2.5}$ (μgm^{-3}) and Air Quality Category (AQC).

	AQI						
	0~50	51~100	101~150	151~200	201~300	301~400	401~500
24 hrm $\text{PM}_{2.5}$	0~15.4	15.5~40.4	40.5~65.4	65.5~150.4	150.5~250.4	250.5~350.4	350.5~500.4
AQC	Good	Moderate	USP	Unhealthy	Very Unhealthy	Hazardous	Hazardous

USP denotes unhealthy conditions for special groups such as elderly and children.

The higher values of $\text{PM}_{2.5}$ during the winter is most likely due to the increased emissions from heating source coupled with low boundary layer height (BLH) and meteorological conditions that limit dispersion [Sun *et al.*, 2004; Guinot *et al.*, 2007]. While the large $\text{PM}_{2.5}$ values from July to September probably result from the enhanced photolysis during the summer months. In the spring and autumn, the lower $\text{PM}_{2.5}$ concentrations are attributed to the increased BLH providing better dispersion and deposition conditions and strong spring winds [Zhao *et al.*, 2009] focusing on our study periods which covering the years with less dust events (2005 and 2007). However, the unimodal pattern shown by POLDER AOD with a significant peak in summer is possibly due to the hygroscopic effect which could be largest in summer when relative humidity is higher.

In order to examine the temporal variation further of both $\text{PM}_{2.5}$ and POLDER

AOD, we analyze their year-by-year evolutions dividing the data into four seasons defined as follows: spring (March-May), summer (June-August), autumn (September-November) and winter (December-February). Different fluctuations of seasonal averaged $PM_{2.5}$ and POLDER AOD are shown in Figure 6.3, where we have only one month with available data in the winter of 2007 (December) and the spring of 2009 (May).

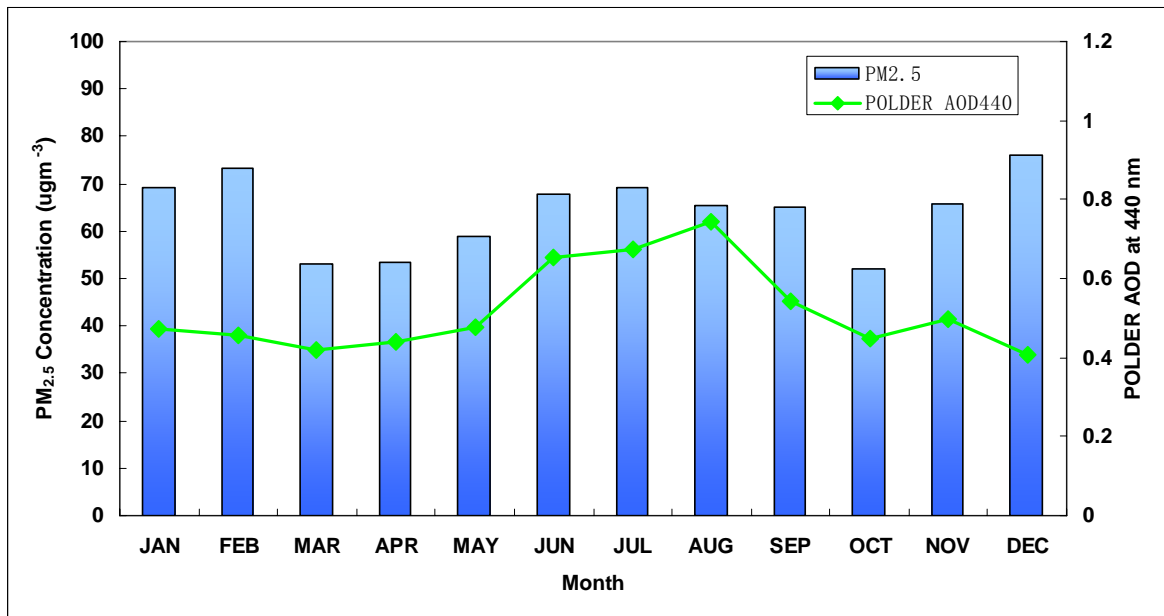


Figure 6.2 Monthly variation of $PM_{2.5}$ and POLDER AOD at 440 nm over Beijing site considering the co-located dataset covering 05/03/2005—31/12/2007 and 01/05/2009—25/05/2010.

Based on our analyses, the annual averaged $PM_{2.5}$ mass concentrations are 64.22, 74.15, 69.09, and 52.01 $\mu\text{g m}^{-3}$ in the year of 2005, 2006, 2007 and 2009, respectively, with standard deviation (SD) of 10.43, 6.72, 18.12 and 12.26 $\mu\text{g m}^{-3}$. The year of 2010, which have available data only in spring, is not considered. The annual averaged POLDER AOD follows the $PM_{2.5}$ trends very well, with the largest value of 0.54 (SD=0.15) in 2006, and the smaller value of 0.47 in 2009 (SD=0.07). Both of $PM_{2.5}$

concentration and POLDER show an increase and reach maxima in 2006 compared to the year of 2005. Then in 2007, these two parameters begin to decrease slightly and are reduced to their minima in 2009. Although the $PM_{2.5}$ concentration decreases a lot in 2009 compared to 2006, the annual averaged $PM_{2.5}$ concentrations are always higher than $52\mu\text{g}\text{m}^{-3}$, indicating the poor air quality corresponding to the AQC of USP in Beijing.

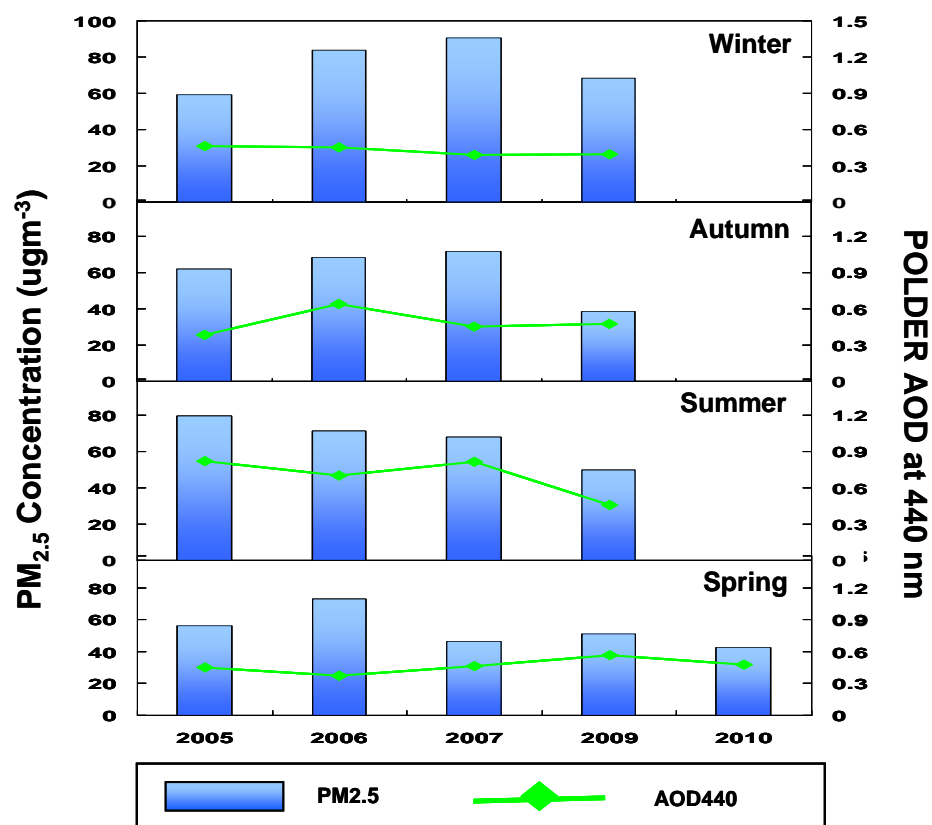


Figure 6.3 Year-by-year evolutions of $PM_{2.5}$ and POLDER AOD at 440 nm in different seasons.

As shown in Figure 6.3, the highest values of $PM_{2.5}$ concentration mostly occur in winter, except the year of 2005 exhibiting the highest $PM_{2.5}$ in the summer. The observed lower concentration in the winter of 2005 likely results from the combination of abundant precipitation and strong, clean northerly winds, which could remove

significant amounts of $PM_{2.5}$ from the urban air of Beijing [Zhao *et al.*, 2009]. Whereas, for the POLDER AOD, the highest values mostly appear in summer, excluding the year of 2009, which presents its maximum in the spring. As is mentioned above, seasonal averaged POLDER in the spring of 2009 is actually the monthly mean value of the May in this year, which might induce some deviation. Focusing on the yearly evolutions of $PM_{2.5}$ and POLDER AOD computed for the given season, we observe the fluctuations varying in different patterns depending on the different seasons. For example, the highest concentration of spring appears in 2006 because of the frequent dust events (11 events for the spring of 2006, while 4 and 3 dust events occurred in the spring of 2005 and 2007) [Zhao *et al.*, 2009]. Such features are not revealed for other seasons. Therefore, we conclude that yearly fluctuations in $PM_{2.5}$ and POLDER AOD in urban areas, such as Beijing, are mostly dominated by annual variability in both emissions and meteorological conditions.

6. 2. 2 The relation between POLDER AOD and ground-level $PM_{2.5}$ concentrations

Figure 6.4 shows the comparison between POLDER AOD at 440 nm and the 24 hourly mean of ground-level $PM_{2.5}$ for ten sites located in Beijing and its surrounding areas considering all the available data from March 2005 to the May of 2010 (Table 6.2). The linear correlation coefficient (R) is 0.521, suggesting that the $PM_{2.5}$ mass which is indicative of near surface values is still reflected in the POLDER column AOD data. The percentage of $PM_{2.5}$ values less than $40\mu g m^{-3}$ is only about 35% with almost 50% of the 24 hourly mean $PM_{2.5}$ values greater than $65\mu g m^{-3}$ indicating that heavy air pollutions attack this urban area very frequently and lower the air quality significantly.

Since the air quality is classified as several categories based on the 24 hourly

averaged $PM_{2.5}$ concentrations (Table 6.2), we derive a simple empirical relation between POLDER AOD and AQI categories by dividing the 24-hr mean $PM_{2.5}$ into 20 bins in $20\mu\text{gm}^{-3}$ intervals referring to the method provided in *Wang et al.* [2003]. The bins with available data of less than five days are not considered in order to assure the reliability of the bin-averaged values. As shown in Figure 6.4, the correlation between bin-averaged POLDER AOD and $PM_{2.5}$ concentration (big black dots) is very high, with the linear correlation coefficient larger than 0.95. To some extent, it implies a possibility to estimate $PM_{2.5}$ and then assess the air quality from POLDER aerosol retrievals. The regression equation is: $AOD_{\text{POLDER}} = 0.005 PM_{2.5} + 0.173$.

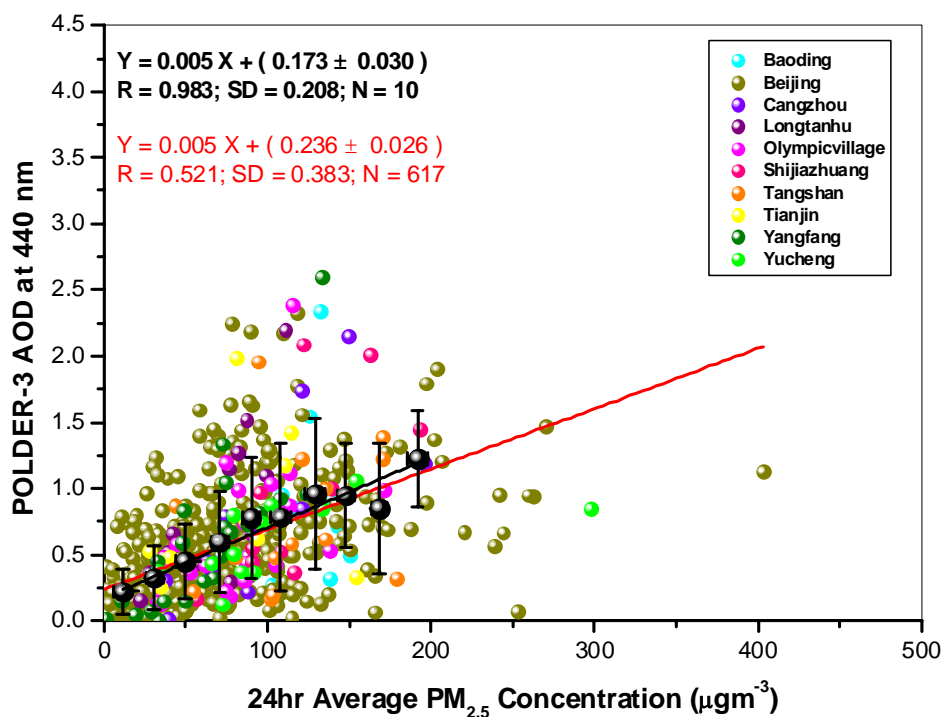


Figure 6.4 Regression line between daily POLDER-3 derived AOD at 440nm and 24hr mean $PM_{2.5}$ concentration measured at the ground (Color dots, $AOD_{\text{POLDER}} = 0.005 PM_{2.5} + 0.236$, $R=0.521$, $N=617$, $SD=0.383$) over Beijing and its surrounding provinces from Mar. 2005 to the May of 2010 and considering the mean values of each bin (Black dots: $AOD_{\text{POLDER}} = 0.005 PM_{2.5} + 0.173$, $R=0.983$, $N=10$, $SD=0.208$).

Based on the equation above, the $PM_{2.5}$ derived from POLDER AOD is quantitatively used to estimate the air quality categories (see color bar in Figure 6.5). The overall accuracy shown in Figure 6.5 is about 36.3%, with 57%, 30%, 20%, 42%, 42%, and 20% of cases are rated correctly for the six Air Quality categories (from good to hazardous). Obviously, it is not very practicable for North China to estimate the $PM_{2.5}$ concentration from satellite derived AOD only by establishing a simple empirical linear relation between them simply. The unsatisfactory accuracy partially indicates the complexity and particularity of aerosol loads in the areas of Beijing and its ambient provinces. More research and some new strategies are needed for air quality remote sensing over this region.

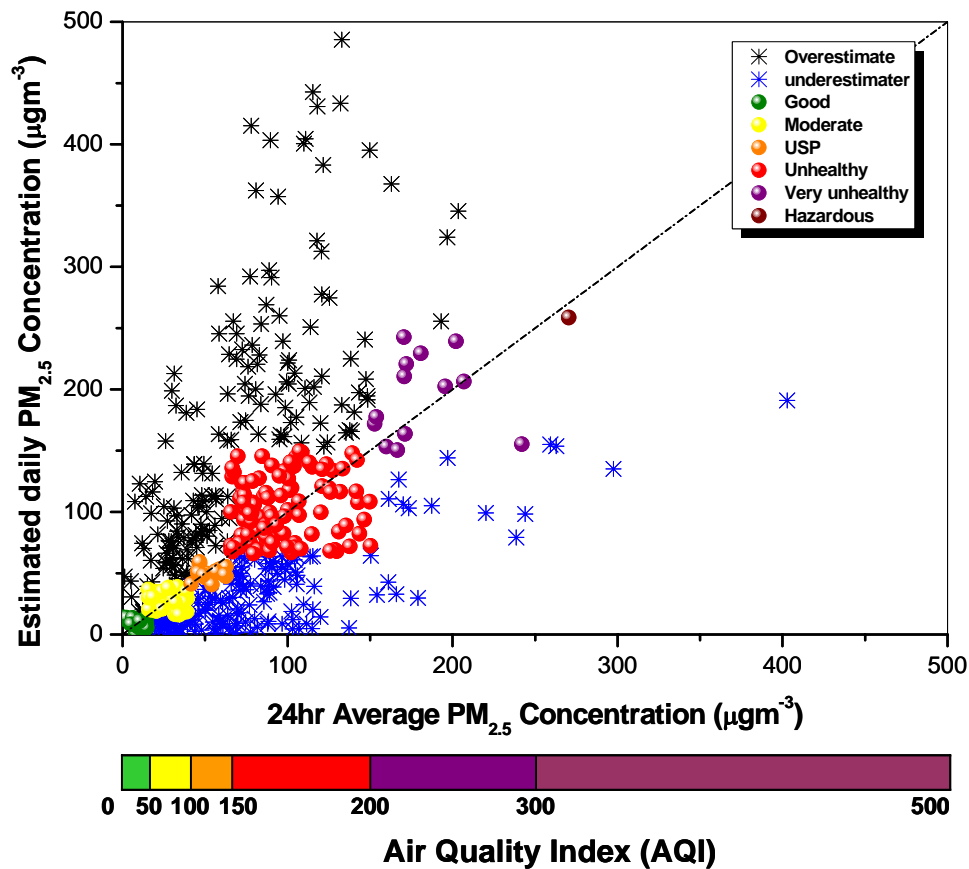


Figure 6.5 AQI derived from POLDER AOD data and its accuracy for each category, where the colored dots concentrating around the diagonal line correspond to the

cases estimated correctly, and the black asterisks represent the overestimated $PM_{2.5}$ concentrations, while the blue ones denote the underestimated $PM_{2.5}$.

Compared to the previous studies which assessed the air quality categories successfully using the similar methods [Wang *et al.*, 2003; Kacenenbogen *et al.*, 2006], we deduce that the regional differences in aerosol characteristics (such as aerosol type, component, vertical distribution and temporal and spatial variability etc.) and meteorological conditions contribute largely to the poor accuracy in our study. Both of two successful cases are performed over the regions, with excellent air quality rated as good to moderate, in United States and Europe. Heavy air pollutions are extremely rare in their concerned areas, but occur very frequently in China. The $PM_{2.5}$ values are very diffuse covering a large range from 0 to above $500\mu\text{gm}^{-3}$, posing difficulties in determining the critical threshold as defined by Kacenenbogen *et al.*, [2006]. Furthermore, the temporal variability of aerosol loads in Beijing is also quite different from the results in Jefferson Country, provided by Wang *et al.*, [2003]. Further discussions are performed revolving the main factors affecting the relation between $PM_{2.5}$ and POLDER AOD in the next section.

6. 2. 3 Main factors and possible improvements

The $PM_{2.5}$ concentration and satellite derived AOD have notable differences, although both of them monitor aerosol loading and are considered as general indicators of air quality. Generally, satellite derived AOD could be considered as a function of the aerosol mass concentration, mass extinction efficiency, hygroscopic growth factor (a function of relative humidity), and effective scale height that is mainly determined by the vertical distribution of aerosols [Kaufman and Fraser, 1983]. In addition, the errors in time-space matching between ground-level $PM_{2.5}$ values and satellites derived AOD also contribute to deviation of the estimated $PM_{2.5}$, besides the retrieval errors in

satellite aerosol retrieval and measuring errors in $PM_{2.5}$ contents. Here in this thesis, we examine the diurnal variations of $PM_{2.5}$ mass which might affect the time matching of ground measurements in different seasons over Beijing, and present roughly some analyses of vertical distribution of aerosol loads over East Asia considering the products of space-borne lidar CALIOP aboard CALIPSO.

6. 2. 3. 1 Diurnal variation of $PM_{2.5}$ concentration over Beijing

The averaged diurnal variations in $PM_{2.5}$ concentration in different seasons over Beijing site are shown in Figure 6.6a. Pronounced diurnal variations of $PM_{2.5}$ are observed with different daily patterns depending on the seasons. Coincident with Figure 6.2, winter usually exhibits the largest $PM_{2.5}$ values (daily average is $84.60 \mu\text{g m}^{-3}$) due to the increased emission from heating and the low boundary layer height, as well as decreased precipitation [Sun et al., 2004], followed by summer with daily averaged $PM_{2.5}$ of $65.70 \mu\text{g m}^{-3}$, while the $PM_{2.5}$ concentration in spring and autumn are relatively lower (50.24 and $41.70 \mu\text{g m}^{-3}$ for spring and autumn respectively).

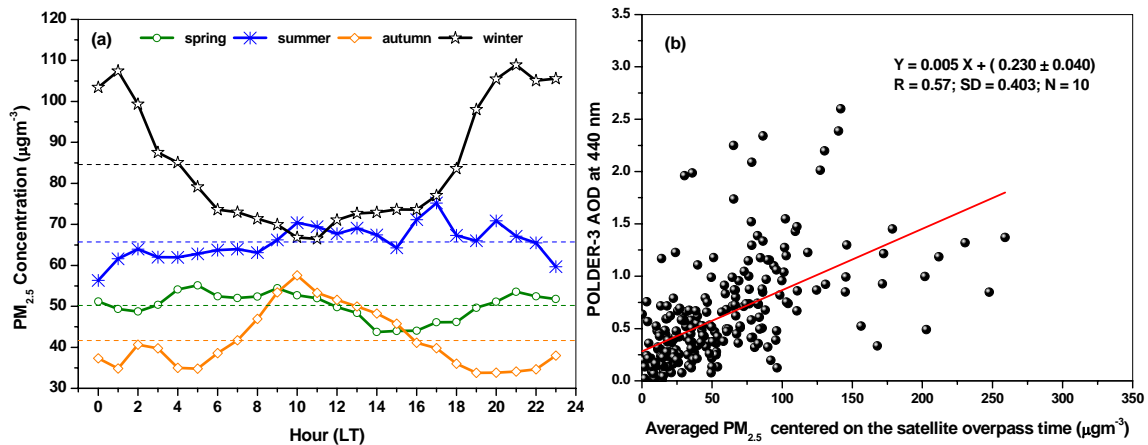


Figure 6.6 (a) Diurnal variations (in Local Time, LT) of $PM_{2.5}$ over Beijing sites in different seasons with dash lines denoting the daily averaged $PM_{2.5}$ contents; and (b) The regression line between daily PARASOL derived AOD at 440nm and averaged ground-level $PM_{2.5}$ concentration measured centered on the satellite overpass time

(red line: $AOD_{POLDER} = 0.005 PM_{2.5} + 0.230$, $R=0.57$, $N=236$, $SD=0.408$).

Seasonal variability in diurnal evolutions of $PM_{2.5}$ is also presented significantly in Figure 6.6a. The fluctuation of daily $PM_{2.5}$ in spring and summer is more gently compared to autumn and winter. In spring, $PM_{2.5}$ concentrations display a slight bimodal pattern with peaks in the morning hours and between 20:00 and 24:00, with a minimum around noon. The morning peak might be attributed to enhanced anthropogenic emission during rush hour. The variations of $PM_{2.5}$ concentrations after sunrise are mainly affected by the development of boundary layer. The decrease following the morning peak is probably due to the dilution of pollutants resulting from the increased Boundary Layer Height (BLH). Similar bimodal pattern could also be observed in summer, but with higher amplitudes than spring. The peak values appear during the rush hours in the morning and evening are 70.41 and $75.18\mu\text{gm}^{-3}$ around 10:00 and 18:00 respectively. Unlike in spring, the $PM_{2.5}$ concentration almost remain unchanging after the morning peak to afternoon due to the higher BLH for a longer time in the afternoon of summer [Guinot *et al.*, 2006; Miao *et al.*, 2008]. In the autumn, the $PM_{2.5}$ contents also show two peaks, including a slight fluctuation around 2:00 and 3:00 a.m. and a high peak in the rush hours caused by anthropogenic activity. The $PM_{2.5}$ concentration in winter varies in a very different pattern from the other seasons. The BLH generally decreases early in the afternoon due to the reduced solar radiation, resulting in a noon time minimum of $PM_{2.5}$ concentration. The combination of decreased BLH and wind speed coupled with increased source activity during the afternoon rush hour contribute to the highest $PM_{2.5}$ contents during the evening hours. At night, the $PM_{2.5}$ concentration decreases because of the reductions in source activity and removal of particles by dry deposition, although the BLH is lowest [Zhao *et al.*, 2009].

Over all, the diurnal variation of $PM_{2.5}$ concentration is related to the synthetic

effects of local source emission and transport, BHL, wind speed, relative humidity and gas-particle transfer, and varies differently depending on the season. Consequently, the mean $PM_{2.5}$ concentration centered on the satellite overpass time (13:00-14:00) is proposed to be considered, instead of the 24 hourly mean $PM_{2.5}$ values, in deriving relation between POLDER AOD and $PM_{2.5}$. According to Figure 6.6a, the averaged $PM_{2.5}$ concentration centered on the satellite overpass time seems comparable with the 24 hourly mean $PM_{2.5}$ in spring, summer and autumn, but In winter, it is much lower and overestimated. The comparison between POLDER AOD and averaged $PM_{2.5}$ concentration also demonstrate possibility of improvement in this term with the higher correlation coefficient of 0.57 (Figure 6.6b).

6. 2. 3. 2 Aerosol vertical distribution from CALIOP

As already stated in our previous description, the vertical extents detected by satellites and the ground-based instruments measuring $PM_{2.5}$ are significantly different. Satellite derived AOD characterize aerosol loads in the entire column, while $PM_{2.5}$ concentrations reflect the aerosol at ground level. Therefore, the vertical structure of aerosol layer is considered as one of the key factors affecting the relation between satellite derived AODs and ground-level $PM_{2.5}$ concentrations.

Cloud-Aerosol Lidar with Orthogonal Polarisation (CALIOP), as primary instrument carried by the Cloud-Aerosol Lidar and Infrared Pathfinder Satellite Observations (CALIPSO) satellite, is a space-borne two-wavelength polarization lidar and acquires global data since 2006 [Winker *et al.*, 2007]. CALIOP provides high resolution vertical profiles of aerosols, and is able to discriminate aerosol layers and detects the layer top and base altitude [Kim *et al.*, 2008]. In this section, we derive the altitude of aerosol layers defined as $(H_{top} + H_{base})/2$ during daytime from CALIOP/CALIPSO level 2 aerosol layer products over East Asia covering the period

of 13/06/2006-31/12/2008, where H_{top} and H_{base} denote the top and base altitudes (km) of the given aerosol layer respectively. And then make some statistical analysis of aerosol vertical distribution information.

Generally, the occurrence probabilities of cases with different number of aerosol layers are shown in Figure 6.7a, as well as their seasonal variability presented in Figure 6.7b. We can find that the number of aerosol layer remains less than 3 in most cases (85.85%) and the monolayer aerosol is always with the highest probability except in the spring.

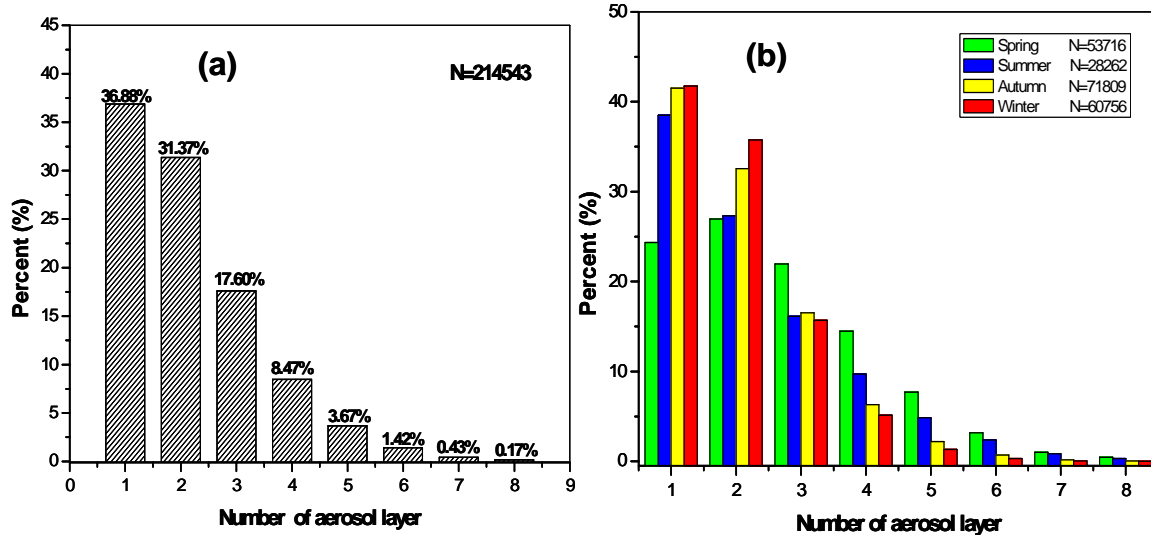


Figure 6.7 (a) Probability of the cases with different number of aerosol layers (1 to 8) for all the CALIOP data from 13/06/2006 to 31/12/2008; (b) Probability for the different cases in different seasons (b).

Focusing on the cases with only one layer, we analyze the probability distribution of aerosol layer altitude (km) (Figure 6.8) and reveal that most aerosol layers locate below 2 km (81.09%) and the highest probability appears around 0.75 km. (the mean altitude is 1.419 km, SD=1.306). Figure 6.9 presents the variation of Aerosol Layer Altitude with Latitude in different seasons. Significant seasonal variability of aerosol

vertical distribution could be observed. Compared to the dispersed distribution in spring and summer, aerosol particles concentrate below 2 km in autumn and winter. The concentration belt of particles around 1 km is interrupted (around 30-35 ° N) due to the combination of the clean air and the lack of available CALIOP aerosol products over the Tibetan Plateau.

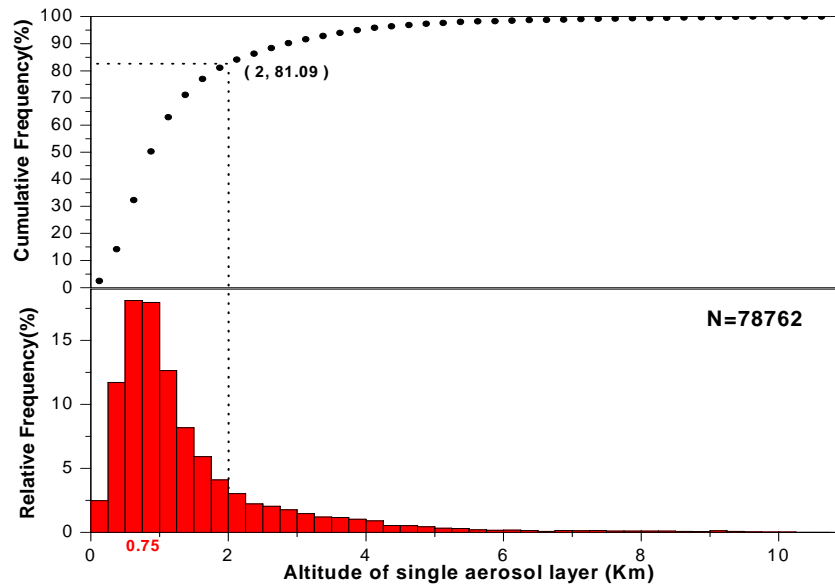


Figure 6.8 Probability distribution of Aerosol Layer Altitude for the cases with only one layer.

According to the rough analysis of the aerosol vertical distribution derived from CALIOP observations, we conclude that aerosol loading mostly appears with less than 3 layers and is concentrated below 2 km, although with significant seasonal and regional variability. The high frequency of the single-layer aerosol loads close to the surface implies the possibility to estimate $PM_{2.5}$ concentration from satellite derived AOD, while the seasonal and regional variability induces the complexity and increases the difficulty in air quality remote sensing. We should also emphasize that accuracy of the aerosol vertical distribution retrieved from CALIOP appears limited during

daytime, especially in the condition with clouds, although it is able to discriminate aerosol layer as well as to detect the layer top and base altitude particularly during night-time under cloud-free conditions. Therefore, the combination of space-borne CALIOP observation and the simultaneously ground-based lidar measurements will be very helpful to provide full and accurate information on the vertical distribution of aerosols [Kim *et al.*, 2008].

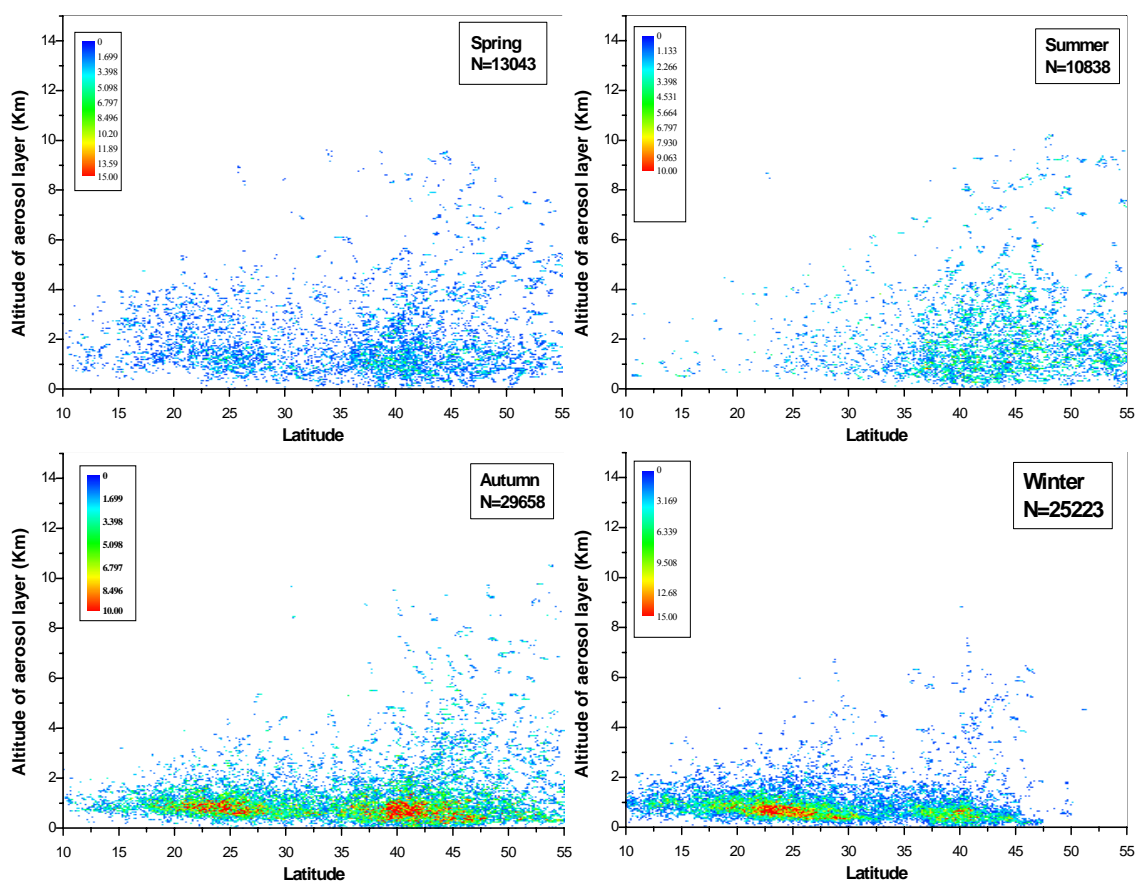


Figure 6.9 The variation of Aerosol Layer Altitude with Latitude in different seasons focusing on the cases with only one layer.

6.3 Conclusions

The good agreement between POLDER AOD440 and ground-based AERONET inversions ($R=0.91$ in Figure 3.2b) proves the high sensitivity of POLDER to fine mode particles, which enlightens us to apply POLDER aerosol retrievals in assessing air quality via the indicator of $PM_{2.5}$ concentration. The correlation coefficient between POLDER AOD440 and daily fine particles mass concentration ($PM_{2.5}$) rises up to 0.98 from 0.52 by arranging the coincident points by bins. A linear relationship is established between $PM_{2.5}$ and POLDER AOD440 according to the regression analysis. However, the accuracy of estimated Air Quality Categories, based on this empirical relationship, is barely satisfactory due to the own characteristics of aerosols loads over East Asia.

Actually, in most of cases, the relationship between these two parameters is not linear and affected by some other factors, such as vertical structure of aerosol loads, aerosol type, meteorological effects, diurnal effects, and so on [*Kaufman and Fraser, 1983*]. The complexity of aerosol loading over East Asia, especially over Beijing and its surrounding areas [*Roger et al., 2009*] increases the difficulty in estimating $PM_{2.5}$ concentration from satellite derived AOD. Therefore, we characterize the diurnal variation of $PM_{2.5}$ concentration and the vertical distribution information from the observations of CALIOP aboard CALIPSO with in hope of improving the accuracy in estimation of $PM_{2.5}$ from POLDER AOD440 in the further study. We also emphasis that more factors should be included to establish the relationship between ground-level $PM_{2.5}$ content and AOD derived from POLDER-3 more accurately.

Chapter 7 Conclusions and Perspectives

7.1 Conclusions

In this dissertation, we analyzed the characteristics of aerosol loads over East Asia considering POLDER aerosol retrievals combined with other databases, such as ground-based sun photometers measurements and $PM_{2.5}$ concentrations, MODIS aerosol products, and space-borne lidar (CALIOP) observations. The analyses performed in this thesis not only improve our knowledge about the aerosol optical properties over East Asia, but also can be considered an expansion of the applications of POLDER aerosol retrievals.

Based on the regional validation of POLDER aerosol products, we analyze the spatial distribution patterns of aerosol loads and their seasonal variability from the individual POLDER-3 observations, and by combining the observations from POLDER and MODIS sensors, respectively. Furthermore, the inter-annual variation during 2003-2009 periods of summer fine-mode AOD over North China, in particular the Beijing City region, was also analyzed for the contribution to evaluating the regional impact of emission reduction enforced in Beijing during the 2008 Olympic Summer Games. In the chapter 6, we discussed the potential of POLDER to assess air quality and provide some preliminary results, consider also the lidar measurements from CALIPSO. Our analyses are concluded as follows:

- 1) POLDER shows a distinct sensitivity to anthropogenic aerosols ($R=0.92$), which are known as one of the main air pollutants influencing the climate, environment and human health. Current POLDER aerosol retrievals (polarization-only) over land are proved to be an efficient tool to investigate the characteristics of

aerosols distribution.

- 2) The combination of POLDER and MODIS method which is sensitive to the entire size distribution provides more useful information of both fine mode and coarse aerosols with a larger spatial coverage potentially, and is helpful for us to distinguish fine and coarse mode aerosol loads and determined their probable sources.
- 3) POLDER aerosol retrievals have great potential for air quality application, combine with other database such as regular meteorological data (e.g., RH) and vertical distribution information provide by CALIOP.

7.2 Perspectives

Our further work will concentrate on the continuation of current studies performed in this thesis. Firstly, Fine and coarse modes AOD distributions will be derived and analyzed over different regions (industrial, potentially impacted by dust transport, etc.) of China from combination of POLDER and MODIS Aqua products. And then, another strategy relying on the Atmospheric Chemistry Transport Models (such as EOS-CHEM, WRF-CHEM) will be applied in the estimation of PM_{2.5} from space-borne POLDER observations. Additionally, future PARASOL retrievals over land [Dubovik *et al.*, 2010] and next generation of space-borne polarimeters (USA, France, China, and Japan) will enhance our knowledge and provide adequate tools for our further study.

Bibliography

Ackerman, S. A., K. I. Strabala, W. P. Menzel, R. A. Frey, C. C. Moeller, and L. E. Gumley (1998): Discriminating clear sky from clouds with MODIS, *J. Geophys. Res.*, 103(D24), p 32139–32140.

Ackerman, A.S., Toon, O.B., Taylor, J.P., Johnson, D.W., Hobbs, P.V., and Ferek, R.J. (2000): Effects of aerosols on cloud albedo: Evaluation of Twomey's parameterization of cloud susceptibility using measurements of ship tracks, *Journal of the Atmos., Sci.*, 57, 2684 – 269.

Ahmad, Z., and R. S. Fraser (1982), An iterative radiative transfer code for ocean-atmosphere system, *J. Atmos. Sci.*, 39, 656– 665.

Anderson, T.L., Charlson, R.J., Schwartz, S.E., Knutti, R., Boucher, O., Rodhe, H., and Heintzenberg, J. (2003): Climate forcing by aerosols – A hazy picture, *Science*, 300, 1103-1104.

Aitchinson J. and J. A. C. Brown, The lognormal distribution function, *Cambridge University Press*, Cambridge, 176 pages, 1957.

Andreae, M.O., and Rosenfeld, D. (2008): Aerosol-cloud-precipitation interactions. Part 1: The nature and sources of cloud-active aerosols. *Earth-Science Reviews*, 89, 13–41.

Angström, A., (1929): On the atmospheric transmission of sun radiation and on dust in the air. *Geogr. Ann.*, 11, 156-166.

- Angström, (1964): The parameters of atmospheric turbidity, *Tellus*, 16, 64–75, 1964.
- Belward, A.S., J.E. Estes, K. D. Kline, 1999: The IGBP-DIS global 1-km land-cover data set discover: A project overview, *Photogramm. Eng. Rem. Sensing*, 65, 1013–1020.
- Bond, T.C., and R.W. Bergstrom (2006): Light absorption by carbonaceous particles: an investigative review, *Aerosol Science and Technology*, 40(1), 27–67.
- Bodhaine, B. A., Wood, N. B., Dutton, E. G., Slusser, J. R.(1999): On Rayleigh Optical Depth Calculations, *J. Atmos. and Ocean. Tech.*, 16, 1854-1861.
- Bréon, F.-M., and S. Colzy (1999), Cloud detection from the spaceborne POLDER instrument and validation against surface synoptic observations, *J. Appl. Meteor.*, 36, p 777-785.
- Cermak, J., and Knutti, R. (2009), Beijing Olympics as an aerosol field experiment, *Geophys. Res. Lett.*, 36, L10806, doi: 10.1029/2009GL038572.
- Chan, C. K., Yao, X. H. (2008), Air pollution in Mega Cities in China – a Review, *Atmos. Environ.*, 42, 1-42.
- Chandrasekhar, S., (1950): Radiative Transfer, *Clarendon Press*, London.
- Charlson, R. J., Schwartz, S. E., Hales, J. M., Cess, R. D., Coakley, J. A., Hansen, J. E., Hofman, D. J. (1992), Climate forcing by anthropogenic aerosols, *Science*, 255, 423–430.
- Chen, D. S., Cheng, S. Y., Liu, L., Chen, T., et al. (2007), An integrated MM5-CMAQ modeling approach for assessing trans-boundary PM10 contribution to the host

- city of 2008 Olympic summer games – Beijing, China, *Atmos. Environ.*, *41*, 1237–1250, doi:10.1016 /j.atmosenv.2006.09.045.
- Choi, Y.-S., R. J. Park, and C. H. Ho (2009), Estimates of ground-level aerosol mass concentrations using a chemical transport model with Moderate Resolution Imaging Spectroradiometer (MODIS) aerosol observations over East Asia, *J. Geophys. Res.*, *114*, D04204, doi: 10.1029/2008JD011041.
- Chowdhary, J., B. Cairns, M.I. Mishchenko, et al., (2005): Retrieval of aerosol scattering and absorption properties from photopolarimetric observations over the ocean during the CLAMS experiment, *J. Atmos. Sci.*, *62*, 1093–1117.
- Chu, D.A., Kaufman, Y.J., Zibordi, G., Chern, J.D., Mao, Jietai, Li, Chengcai and B.N. Holben (2003): Global monitoring of air pollution over land from the Earth Observing System-terra Moderate Resolution Imaging Spectroradiometer (MODIS), *J. Geophys. Res.*, *108*, D21, 4661, doi: 10.1029/2002JD003179.
- Colbeck, I. (2008): Environmental Chemistry of Aerosols, Blankwell Publishing Ltd. ISBN: 978-1-405-13919-9.
- Cox, C., and W. Munk (1954), Measurements of the roughness of the sea surface from photographs of the Sun’s glitter, *J. Opt. Soc. Am.*, *44*, 838–850.
- Curier, R.L., Veefkind, J.P., Braak, R., Veihermann, B., Torres, O., and de Leeuw, G., 2008: Retrieval of aerosol optical properties from OMI radiances using a multiwavelength algorithm: Application to western Europe. *J. Geophys. Res.*, *113* doi:10.1029/2007JD008738.
- Damoah, R., Spichtinger, N., Forster, C., James, P., Mattis, I., Wandinger, U., Beirle,

S., Wagner, T., and Stohl, A. (2004), Around the world in 17 days – hemispheric-scale transport of forest fire smoke from Russia in May 2003, *Atmos. Chem. Phys.*, 4, 1311-1321.

Dave J V. (1970): Intensity and polarization of radiation emerging from a plane-parallel atmosphere containing mono-dispersed aerosols. *Applied Optics*, 9(12): 2673—2687.

Deirmendjian, D., Electromagnetic scattering on spherical polydispersions, *American Elsevier*, Pub, New York, 290 pages, 1969.

Deschamps, P. Y., Bréon, F. M., Leroy, M., Podaire, A., Bricaud, A., Buriez, J. C., and Seze, G. (1994), The POLDER mission: instrument characteristics and scientific objectives, *IEEE Trans. Geosc. Remote Sensing*, 32, 598-615.

Deuzé, J.L. (1974), Etude de la polarisation du rayonnement par les milieux diffusants, application à la polarisation localisée de Vénus, *thèse, Université des Sciences et technologies de Lille*.

Deuzé J.L., F.M. Bréon, P.Y. Deschamps, C. Devaux, M. Herman, A. Podaire, and J.L. Roujean (1993), Analysis of the POLDER (Polarization and Directionality of Earth's Reflectances) Airborne Instrument Observations over Land Surfaces, *Remote Sens. Environ.*, 45, p 137-154.

Deuzé, J. L., P. Goloub, M. Herman, A. Marchand, G. Perry, S. Susana, and D. Tanré (2000), Estimate of the aerosol properties over the ocean with POLDER, *J. Geophys. Res.*, 105, 15,329–15,346.

Deuzé, J. L., Bréon, F.M., Devaux, C., Goloub, P., Herman, M., Lafrance, B., et al.

- (2001). Remote sensing of aerosols over land surfaces from POLDERADEOS-1 polarized measurements, *J. Geophys. Res.*, *106*, 4913 – 4926.
- Dey, S., S. N. Tripathi, R. P. Singh, and B. N. Holben (2004), Influence of dust storms on the aerosol optical properties over the Indo-Gangetic basin, *J. Geophys. Res.*, *109*, D20211, doi:10.1029/2004JD004924.
- Di Girolamo, L., T. C. Bond, D. Bramer, D. J. Diner, F. Fettinger, R. A. Kahn, J. V. Martonchik, M. V. Ramana, V. Ramanathan, and P. J. Rasch (2004): Analysis of Multi-angle Imaging SpectroRadiometer (MISR) aerosol optical depths over greater India during winter 2001-2004, *Geophys. Res. Lett.*, *31*, L23115, doi: 10.1029/2004GL021273.
- Duan, F., Liu, X., Yu, T., Cachier, H. (2004), Identification and estimate of biomass burning contribution to the urban aerosol organic carbon concentrations in Beijing, *Atmos. Environ.*, *38*, 1275–1282.
- Dubovik, O. and M. D. King, (2000): A flexible inversion algorithm for retrieval of aerosol optical properties from Sun and sky radiance measurements," *J. Geophys. Res.*, *105*, 20 673 - 20 696.
- Dubovik, O., A. Smirnov, B. Holben, et al., (2000): Accuracy assessments of aerosol optical properties retrieved from Aerosol Robotic Network (AERONET) sun and sky radiance measurements. *J. Geophys. Res.*, *105* (D8), 9791 - 9806.
- Dubovik O, Holben B N, Lapyonok T, Sinyuk A, Mishchenko M I, Yang P and Slutsker I. (2002a): Non-spherical aerosol retrieval method employing light scattering by spheroids. *Geophys. Res. Lett.*, *29*(10): 1415, doi: 10.1029/2001GL014506

- Dubovik, O., Holben, B. N., Eck, T. F., Smirnov, A., Kaufman, Y. J., King, M. D., Tanré, D., and Slutsker, I. (2002b), Variability of absorption and optical properties of key aerosol types observed in worldwide locations, *J. Atm. Aci.*, *59*, 590-608.
- Dubovik, O., A. Sinyuk, T. Lapyonok, B. N. Holben, M. Mishchenko, P. Yang, T. F. Eck, H. Volten, O. Munoz, B. Veihelmann, W. J. van der Zande, J-F Leon, M. Sorokin, and I. Slutsker, (2006): Application of spheroid models to account for aerosol particle nonsphericity in remote sensing of desert dust. *J. Geophys. Res.*, *111*, doi: 10.1029/2005JD006619.
- Eck, T. F., Holben, B. N., Reid, J.S., Dubovik, O., Smirnov, A., O'Neil, N.T., Slutsker, I. and Kinne, S. (1999), Wavelength dependence of the optical depth of biomass burning, urban, and desert dust aerosols. *J. Geophys. Res.*, *104*, D24, 31333–31349.
- Eck, T. F., Holben, B. N., Dubovik, O., Smirnov, A., Goloub, P., Chen, H. B., et al. (2005), Columnar aerosol optical properties at AERONET sites in central eastern Asia and aerosol transport to the tropical mid-Pacific. *J. Geophys. Res.*, *110*, D06202, doi: 10.1029/2004JD005274.
- Fan, X. H., Chen, H. B., Goloub, P., Xia, X. A., Zhang, W. X., Chatenet, B. (2006), Analysis of column-integrated aerosol optical thickness in Beijing from AERONET observations, *China Particuology*, *40(6)*, 330–335.
- Fan, X. H., Goloub, P., Deuzé, J. L., Chen, H. B., Zhang, W. X., Tanré, D., Li, Z. Q., (2008), Evaluation of PARASOL aerosol retrieval over North East Asia, *Remote Sens. Environ.*, *112*, 697-707.
- Favez, O., Sciare, J., Cachier, H., Alfaro, S.C., and Abdelwahab, M.M. (2008):

- Significant formation of water-insoluble secondary organic aerosols in semi-arid urban environment, *Geophys. Res. Lett.*, 35, L15801, doi:10.1029/2008GL03446.
- Forster, P., et al. (2007), Changes in atmospheric constituents and in radiative forcing, In: Climate change 2007: The physical science basis, Contribution of working group 1 to the fourth assessment report of the IPCC, *Cambridge University Press, Cambridge, UK and New York, NY, USA*.
- Gatebe, C.K., M.D. King et al., (2001): Sensitivity of off-nadir zenith angles to correlation between visible and near-infrared reflectance for use in remote sensing of aerosol over land, *IEEE Trans. Geosci. RemoteSens.*, 39(4), 805–819.
- Gérard, B., J.-L. Deuzé, M. Herman, Y. J. Kaufman, P. Lallart, C. Oudard, L. A. Remer, B. Roger, B. Six, and D. Tanré (2005), Comparisons between POLDER 2 and MODIS/Terra aerosol retrievals over ocean, *J. Geophys. Res.*, 110, D24211, doi:10.1029/2005JD006218.
- Goloub, P., Tanré, D., Deuzé, J.L., Herman, M., Marchand, A., Breon, F.-M. (1999): Validation of the first algorithm applied for deriving the aerosol properties over the ocean using the POLDER/ADEOS measurements, *IEEE Trans. Geosci. and Remote Sens.*, Vol.37, n.3, pp.1586-1596.
- Goloub, P., M. Herman, J.L. Deuzé, P. Lallart (2005): Validation of POLDER-2 basic aerosol parameters over ocean, submitted to *Rem. Sens. Environ.*
- Gorchakov, G.I., (1966): Light scattering matrices of atmospheric air, *Izv. Akad. Nauk SSSR, Fiz. Atmos. Okeana*, 2, 595–605.
- Goudie, A. S., and N. J. Middleton (1992): The changing frequency of dust storms

through time, *Clim. Change*, 20, 197–225.

Gras, J. L. (1991): Southern hemisphere tropospheric aerosol microphysics, *J. Geophys. Res.*, 96(D3), p 5345–5356.

Grassl, H., (1971): Determination of aerosol size distributions from spectral attenuation measurements. *Appl. Opt.*, 10, 2534-2538.

Guinot, B., Cachier, H., Sciare, J., Tong, Y., Wang, X., Yu, J. (2007): Beijing aerosol: atmospheric interactions and new trends. *J. Geophys. Res.*, 112, D14314.
doi:10.1029/2006JD008195.

Guinot, B., Roger, J., Cachier, H., Wang, P., Bai, J., Yu, T. (2006): Impact of vertical atmospheric structure on Beijing aerosol distribution. *Atmos. Environ.*, 40, 5167–5180.

Halthore, R.N., T.F., Eck, B.N., Holben, and B.L., Markham. 1997. “Sunphotometric measurements of atmospheric water vapor column abundance in the 940-nm band. *J. Geophys. Res.* 102: 4343–4352.

Han, Z., Ueda, H., Matsuda, K. (2005), Model study of the impact of biogenic emission on regional ozone and the effectiveness of emission reduction scenarios over eastern China. *Tellus* 57B, 12–27.

Hänel, G., The properties of atmospheric aerosol particles as functions of the relative humidity at thermodynamic equilibrium with surrounding moist air. *Adv. in Geophys.*, 19, p 73-188, 1976.

Hansen, J., Sato, M., and Ruedy, R. (1997): Radiative forcing and climate response, *J. Geophys. Res.*, 102, 6831 - 6864.

- Hatakeyama, S., Takami, A., Wang, W., Tang, D. (2005), Aerial observation of air pollutants and aerosols over Bo Hai, China, *Atmos. Environ.*, 39, 5893–5898.
- Hauck, H., Berner, A., Frischer, T., Gomiscek, B., Kundi, M., Neuberger, M., Puxbaum, H., Preining, O., and AUPHEP-Team (2004): AUPHEP-Austrian Project on Health Effects of Particulates – general overview, *Atmos. Environ.*, 38, 3905 – 3915.
- Haywood, J.M., and Ramaswamy, V. (1998): Global sensitivity studies of the direct radiative forcing due to anthropogenic sulfate and black carbon aerosols, *J. Geophys. Res.*, 103, 6043 - 6058.
- He, X., Li, C. C., Lau, A. K. H., Deng, Z. Z., Mao, J. T., Wang, M. H., and Liu, X. Y. (2009), An intensive study of aerosol optical properties in Beijing urban area, *Atmos. Chem. Phys.*, 9, 8903-8915.
- Herman J. R., P. K. Bhartia, O. Torres, C. Hsu, C. Seftor, and E. Celarier (1997a), Global distribution of UV-absorbing aerosol from Nimbus 7/TOMS data, *J. Geophys. Res.*, 102, p 16911 - 16922.
- Herman M., J.L. Deuzé, C. Devaux, P. Goloub, F. M. Bréon, and D. Tanré (1997b), Remote Sensing of aerosols over land surfaces including polarization measurements and application to POLDER measurements, *J. Geophys. Res.*, 102, p 17039-17044.
- Herman, M., J. L. Deuzé, A. Marchand, B. Roger, and P. Lallart (2005): Aerosol remote sensing from POLDER/ADEOS over the ocean: Improved retrieval using non-spherical particle model, *J. Geophys. Res.*, 110, D10S02, doi:10.1029/2004JD004798.

- Hinds W.C. (1982): *Aerosol technology*, Wiley, New York, 442 pages.
- Hinds, W.C. (1999), *Aerosol Technology: Properties, Behavior, and Measurement of Airborne Particles*, 2nd ed., Wiley, New York.
- Holben, B. N., Eck, T. F., Slutsker, I., Tanré, D., Buis, J. P., Setzer, A., et al. (1998), AERONET— A federated instrument network and data archive for aerosol characterization, *Remote Sens. Environ.*, *66*, 1–16.
- Holben, B. N., Tanré, D., Smirnov, A., Eck, T. F., Slutsker, I., Abuhassen, N., et al. (2001): An emerging ground-based aerosol climatology: Aerosol optical depth from AERONET, *J. Geophys. Res.*, *106*, 12, 067–12, 097.
- Horvath, H., (1993): Atmospheric light absorption – A review, *Atmos. Environ.*, *27*, 293–317.
- Huang, J., P. Minnis, Y. Yi, Q. Tang, X. Wang, Y. Hu, Z. Liu, K. Ayers, C. Trepte, and D. Winker (2007), Summer dust aerosols detected from CALIPSO over the Tibetan Plateau, *Geophys. Res. Lett.*, *34*, L18805, doi:10.1029/2007GL029938.
- Ibald-Mulli, A., Wichmann, H.E., Kreyling, W., and Peters, A. (2002): US National Oceanic and Atmospheric Administration, *Air Resources Laboratory, Silver Spring*, web address: <http://www.arl.noaa.gov/ss/models/hysplit.html>.
- Jacobson, M.Z. (2000): Aphysically-based treatment of elemental carbon optics: Implications for global direct forcing of aerosols, *Geophys. Res. Lett.*, *27*, 217 – 220.
- Jacobson, M.Z. and Kaufman, Y.J.(2006): Wind reduction by aerosol particles, *Geophys. Res. Lett.*, *33*, L24824, doi:10.1029/2006GL027838.

- Jaenicke R. (1993): Tropospheric aerosols, *In Hobbs, P. V. editor, Aerosol-Cloud-Climate interactions*, p 1-31, Academic Press, San Diego, CA,.
- John, W. (2001): Size distribution characteristics of aerosols. In: P.A. Baron and K. Willeke, eds. *Aerosol Measurement*, 2nd edn. JohnWiley and Sons, New York.
- Junge, C.E., (1963): Air Chemistry and Radioactivity. *Academic Press Inc*, New York
- Kacenelenbogen, M., Léon, J. F., Chiapello, I., and Tanré, D. (2006), Characterization of aerosol pollution events in France using ground-based and POLDER-2 satellite data, *Atmos. Chem. Phys.*, *6*, 4843-4849.
- Kacenelenbogen, M. (2008): Application of remote sensing to monitoring air pollution, *Doctoral thesis*, Laboratory of Atmospheric Optics of USTL, France.
- Kanaya, Y., Kajii, Y., Akimoto, H. (2003): Solar actinic flux and photolysis frequency determinations by radiometers and a radiative transfer model at Rishiri Island: comparisons, cloud effects, and detection of an aerosol plume from Russian forest fires, *Atmos. Environ.*, *37*, 2463-2475.
- Kasten, F. and Young, A. T., Revised optical air mass tables and approximation formula, *Appl. Opt.*, *28*, 4735–4738, 1989 .
- Kaufman, Y.J., and R.S. Fraser (1983), Light extinction by Aerosols During Summer Air Pollution, *J. Appl. Meteor.*, *22*, 1694-1706.
- Kaufman, Y.J., D. Tanré et al., (1997a): Operational remote sensing of tropospheric aerosol over land from EOS moderate resolution imaging spectroradiometer. *J. Geophys. Res.*, *102(D14)*, 17051–17067.

Kaufman, Y.J., Wald, A.E., Remer, L.A., et al. (1997b). The MODIS 2.1 μm channel—correlation with visible reflectance for use in remote sensing of aerosol. *IEEE Trans. Geosci. Remote Sens.* 35, 1286–1298.

Kaufman Y. J. and Tanré D., Algorithm for remote sensing of tropospheric aerosol from MODIS, Product ID: MOD04, 85 pages, 1998.

Kaufman, Y., Smirnov A., Holben B., and Dubovik O., (2001): Baseline maritime aerosol: methodology to derive the optical thickness and scattering properties, *Geophys. Res. Lett.*, 28, 3251–3254.

Kaufman, Y. J., Tanré, D., Boucher, O. (2002): A satellite view of aerosols in the climate system, *Nature*, 419, 215 – 223.

Kawata Y. (1978): Circular polarization of sunlight reflected by planetary atmospheres. *Icarus*, 33, p 217-232, doi:10.1016/0019-1035(78)90035-0.

Kim, D.-H., B. -J. Sohn, T. Nakajima, T. Takamura, T. Takemura, B. -C. Choi, and S. -C. Yoon (2004), Aerosol optical properties over East Asia determined from ground-based sky radiation measurements, *J. Geophys. Res.*, 109, D02209, doi: 10.1029/2003JD003387.

Kim, S. -W., Yoon, S. -C., Kim, J. Y., and Kim S. -J. (2007), Seasonal and monthly variations of columnar aerosol optical properties over East Asia determined from multi-year MODIS, LIDAR, and AERONET Sun/sky radiometer measurements, *Atmos. Environ.*, 41, 8, 1634-1651.

Kim, S.-W., Berthier, S., Raut, J.-C., Chazette, P., Dulac, F., and Yoon, S.-C.(2008): Validation of aerosol and cloud layer structures from the space-borne lidar CALIOP

using a ground-based lidar in Seoul, Korea, *Atmos. Chem. Phys.*, 8, 3705-3720, doi:10.5194/acp-8-3705-2008.

King, M. D., Byrne, D. M., Herman, B. M., and Reagan, J. A. (1978): Aerosol size distributions obtained by inversion of spectral optical depth measurements, *J. Atmos. Sci.*, 35, 2153-2167.

King, M.; Kaufman, Y.; Tanre, D.; Nakajima, T. (1999) : Remote Sensing of Tropospheric Aerosols from Space: Past, Present, and Future; *Bull. Am. Meteorol. Soc.*, 80, 2229-2259.

Koepke, P., (1984): Effective reflectance of oceanic whitecaps. *Appl. Opt.*, 23, 1816–1842.

Kokhanovsky, Alexander A., Breon, F.-M., Cacciari, A., Carboni, E., Diner, E., et al. (2007): Aerosol remote sensing over land: A comparison of satellite retrievals using different algorithms and instruments, *Atmos. Res.*, 85, 372-394.

Kokhanovsky, Alexander A., de Leeuw, Gerrit et al. (2009), Satellite Aerosol Remote Sensing Over Land, *Springer-Praxis Books in Environmental Sciences Subject*, Germany, XVII, ISBN: 978-3-540-69396-3, 2009.

Krewski, D., et al. (2000): Reanalysis of the Harvard Six Cities Study and the American Cancer Society Study of Particulate Air Pollution and Mortality. *Health Effects Institute, Cambridge, MA*.

Kumagai, K., Iijima, A., Tago, H., Tomioka, A., Kozawa, K., and Sakamoto, K. (2009): Seasonal characteristics of water-soluble organic carbon in atmospheric particles in the inland Kanto plain, Japan, *Atmos. Environ.*, 43, 3345-3351.

- Langley, S. P., 1881: The bolometer and radiant energy. *Proc. Amer. Acad. Arts Sci.*, 16, 342
- Lee, K. H., Kim, J. E., Kim, Y. J., Kim, J., et al. (2005), Impact of the smoke aerosol from Russian forest fires on the atmospheric environment over Korea during May 2003, *Atmos. Environ.* 39, 85-99.
- Lee, K.H. , Li, Z., Kim, Y.J., and Kokhanovsky, A.A., 2009: Aerosol monitoring from satellite observations: a history of three decades, *Atmospheric and Biological Environmental Monitoring*, Y.J. Kim, U. Platt, M.B. Gu, and H. Iwahashi (eds.), Berlin: Springer.
- Legrand M., J. J. Bertrand, M. Desbois, L. Ménénger, and Y. Fouquart (1989), The potential of infrared satellite data for the retrieval of Saharan-dust optical depth over Africa, *J. Appl. Meteor.*, 28, p 309-318.
- Lenoble, J. (1993): Atmospheric radiative transfer, *A. Deepak Publishing*, Hampton, 532 pages.
- Levy, R. C., L. A. Remer, D. Tanré, Y. J. Kaufman, C. Ichoku, B. N. Holben, J. M. Livingston, P. B. Russel, and H. Maring (2003): Evaluation of the Moderate-Resolution Imaging Spectroradiometer (MODIS) retrievals of dust aerosol over the ocean during PRIDE, *J. Geophys. Res.*, 108(D19), 8594, doi:10.1029 /2002JD002460.
- Levy, R.C., Remer, L.A., and Dubovik, O., (2007a): Global aerosol optical properties and application to Moderate Resolution Imaging Spectroradiometer aerosol retrieval over land. *J. Geophys. Res.*, 112, D13210, doi: 10.1029/2006JD007815.

- Levy, R.C., Remer, L.A., Mattoo, S., Vermote, E.F., and Kaufman, Y.J., (2007b): Second-generation operational algorithm: Retrieval of aerosol properties over land from inversion of Moderate Resolution Imaging Spectroradiometer spectral reflectance. *J. Geophys. Res.*, 112, D13211, doi: 10.1029/2006JD007811.
- Li, C. C., Mao, J. T., et al. (2003), Characteristics of distribution and seasonal variation of aerosol optical depth in eastern China with MODIS products, *Chin. Sci. Bull*, 48, 22, 2488 - 2495.
- Li, C. C., Mao, J. T., Lau, A. K. (2003), Characteristics of aerosol optical depth distributions over Sichuan Basin derived from MODIS data, *J. Appl. Meteorol. Sci.*, 14, 1, 1-7.
- Li, Z., P. Goloub, O. Dubovik, L. Blarel, W. Zhang, T. Podvin, A. Sinyuk, M. Sorokin, H. Chen, B. Holben, D. Tanre, M. Canini, J.-P. Buis (2009): Improvements for ground-based remote sensing of atmospheric aerosol properties by additional polarimetric measurements, *J. Quantitative Spectroscopy and Radiative Transfer*, doi: 10.1016/j.jqsrt.2009.04.009
- Li, Z., King, M., Tsay, S., Holben, B., Kaufman, Y., Dickerson, R. R. (2002), East Asia source region aerosols (EASRA): An ideal test-bed for studying the direct and indirect climate effects of natural and anthropogenic aerosols, *the 11th Conference on Atmospheric Radiation*, Ogden, UT, USA.
- Li, J., G. Zhuang, K. Huang, Y. Lin, C. Xu, and S. Yu (2008), Characteristics and sources of air-borne particulate in Urumqi, China, the upstream area of Asia dust, *Atmos. Environ.*, 42, 776– 787, doi:10.1016/j.atmosenv. 2007. 09. 062.
- Liousse, C. H., Penner, J.E., Chuang, C., Walton, J.J., Eddleman, H. Cachier (1996): A

- global threedimensional model study of carbonaceous aerosols, *J. of Geophys. Res.*, 101, p 19411 - 19432.
- Liu, X.D., Yin, Z.Y., Zhang, X.Y., Yang, X.C. (2004): Analyses of the spring dust storm frequency of northern China in relation to antecedent and concurrent wind, precipitation, vegetation, and soil moisture conditions, *J. Geophys. Res.*, 115, D24215, doi:10.1029/2010JD014286.
- Liu, Y., R.J., Park, D.J., Jacob, Q. Li, V. Kilaru, and J. A. Samat (2004): Mapping annual mean ground-level PM_{2.5} concentrations using Multi-angle Imaging Spectroradiometer aerosol optical thickness over the contiguous United States, *J. Geophys. Res.*, 109, D22206, doi:10.1029/2004JD005025.
- Liu, Y., Sarnat, J.A., Kilaru, V., Jacob, D.J., and Koutrakis, P. (2005): Estimating Ground-level PM_{2.5} in the Eastern United States Using Satellite Remote Sensing, *Environ. Sci. Technol.*, 39, 3269-3278.
- Luo, C., St. John, J.C., Zhou, X., Lam, K.S., Wang, T., Chameides, W. L. (2000), A nonurban ozone air pollution episode over eastern China: observations and model simulations. *J. Geophys. Res.*, 105, 1889–1908.
- Luo, Y., D., Lu, X., Zhou, W. Li, and Q., He (2001), Characteristics of the spatial distribution and yearly variation of aerosol optical depth over China in last 30 years, *J. Geophys. Res.*, 106 (D13), 14, 501 – 14, 513.
- Littmann, T. (1991), Dust storm frequency in Asia: Climatic control and variability, *Int. J. Climatol.*, 11, 393–412.
- Malm, W.C., et al. (1994) : Spatial and seasonal trends in particle concentration and

- optical extinction in the United States, *J. Geophys. Res.*, 99, 1357-1370.
- Manahan, S.E., (1993): Fundamentals of Environmental Chemistry, Sixth edition, Lewis publishers, Michigan, U.S.A., 844 pages. (ISBN:1-56670-08804).
- Mandakh N., Khaulenbek A. (2002), Research activities of dust storm in Mongolia: Transportation process of dust storm and its temporal-spatial distribution in Gobi, *International Workshop on Dust Storm (IWDUST, Beijing)*.
- Marshall, J. (2005), Megacity, Mega Mess, *Nature*, 437, 312-314.
- Mauzerall, D.L., Narita, D., Akimoto, H., Horowitz, L., Walters, S., Hauglustaine, D.A., Brasseur, G. (2000), Seasonal characteristics of tropospheric ozone production and mixing ratios over East Asia: a global three-dimensional chemical transport model analysis. *J. Geophys. Res.*, 105, 17,895–17,910.
- Miao, S., Chen, F., LeMone, M., Tewari, M., Li, Q., Wang, Y. (2008): An observational and modeling study of characteristics of Urban Heat Island and boundary layer structures in Beijing. *J. Appl. Meteor. and Climat.* 48 (3), 484–501.
- Michalsky, J. (1998): The astronomical almanac's algorithm for approximate solar position (1950-2030). *Solar Energy*, 40, 227-235.
- Mie, G., Beiträge zur Optik trüber Medien, speziell kolloidaler Metallösungen, *Ann. Geophys.*, 25, p 377-445, 1908.
- Murdiyarso, D., and Lebel, L. (2007): Local to global perspectives on forest and land fires in Southeast Asia. *Mitigation and Adaptation Strategies for Global Change*, 12(1), 3-11.

- Murr, L.E. and Garza, K.M. (2009): Natural and anthropogenic environmental nanoparticulates, *Atmos. Environ.*, 43m 26, 2683-2692.
- Myhre, G., et al. (2004): Intercomparison of satellite retrieved aerosol optical depth over the ocean, *J. Atmos. Sci.*, 61, 499–513.
- Nadal, F., and F. M. Bréon (1999): Parameterization of surface polarized reflectance derived from POLDER spaceborne measurements, *IEEE Trans. Geosci. Remote Sens.*, 37, 1709 - 1718.
- National Bureau of Statistics of China (NBS): *China Statistical Yearbook 2004*, China Statistics Press, Beijing.
- Novakov, T. and Corrigan, C. E. (1996): Cloud condensation nucleus activity of the organic component of biomass smoke particles, *Geophys. Res. Lett.*, 23, 22141-2144.
- Nyeki, S., Li, F., Weingartner, E., Streit, N., Colbeck, I., Gaggeler, H.W. and Baltensperger, U. (1998): The background aerosol size distribution in the free troposphere: an analysis of the annual cycle at a high-alpine site. *Journal of Geophysical Research – Atmospheres*; 103: 31749–31761.
- O’Neill, N. T., and Miller, J. R. (1984): Combined solar aureole and solar beam extinction measurements. 1: Calibration considerations. *Appl. Opt.* 23:3691–3696.
- Padoch, C., Coffey, K., Mertz, O., Leisz, S., Fox, J., and Wadley, R. (2007), The Demise of Swidden in Southeast Asia? Local Realities and Regional Ambiguities, *Danish Journal of Geography*, 107(1), 29-41.
- Park, R. J., et al. (2005), Export efficiency of black carbon aerosol in continental

- outflow: Global implications, *J. Geophys. Res.*, *110*, D11205, doi: 10.1029/2004JD005432.
- Patasnick, H., Rupprecht, E.G. (1991): Continuous PM-10 measurement using the tapered element oscillating microbalance, *J Air waste Manage Assoc.*, *41*, p 1079-1083.
- Poschl, U. (2002): Formation and decomposition of hazardous chemical components contained in atmospheric aerosol particles, *Journal of Aerosol Medicine*, *15*, 203 – 212.
- Qian, W. H., L. S. Quan, and S. Y. Shi (2002), Variations of the dust storm in China and its climatic control, *J. Clim.*, *15*(10), 1216– 1229.
- Qian, Z. A., Cai, Y., Liu, J. T., et al. (2006), Some advances in dust storm research over China Mongolia areas, *Chinese J. Geophys. (In Chinese)*, *49*(1): 83-92.
- Ramanathan, V., P. J. Crutzen, J. T. Kiehl, and D. Rosenfeld (2001), Aerosols, climate, and the hydrological cycle, *Science*, *294*(5549), 2119–2124.
- Ramanathan, V. and Feng, Y. (2009): Air pollution, greenhouse gases and climate change: Global and regional perspectives, *Atmos. Environ.*, *43*, 37 – 50.
- Ramaswamy, V., O. Boucher, J. Haigh, D. Hauglustaine, J. Haywood, G. Myhre, T. Nakajima, G.Y. Shi, S. Solomon (2001), Radiative forcing of climate change. In: *Climate Change 2001: The Scientific Basis. Contribution of Working Group I to the Third Assessment Report of the Intergovernmental Panel on Climate Change* [Houghton, J.T., et al. (eds.)]. Cambridge University Press, Cambridge, United Kingdom and New York, NY, USA, p 349–416.

- Rayleigh, L., On the transmission of light through an atmosphere containing many small particles in suspension, and on the origin of the blue of the sky, *Phil. Mag.* 47, p. 375-384, 1889.
- Remer, L. A., Kaufman, Y. J., & Holben, B. N. (1996), The size distribution of ambient aerosol particles: Smoke vs. urban/industrial aerosol, *Global Biomass Burning. Cambridge MA: The MIT Press.*
- Remer, L.A., A.E., Wald, et al., (2001): Angular and seasonal variation of spectral surface reflectance ratios: implications for the remote sensing of aerosol over land, *IEEE Trans. Geosci. Remote Sens.*, 39(2), 275–283.
- Remer, L.A., Tanré, D., Kaufman, Y. J., Ichoku, C., Mattoo, S., Levy, R. et al. (2002): Validation of MODIS aerosol retrieval over ocean. *Geophys. Res. Lett.*, 29, 8008, doi:10.1029/2001GL013204.
- Remer, L.A., Kaufman, Y. J., Tanré, D., Mattoo, S., Chu, D.A., Martins, J.V., et al. (2005): The MODIS aerosol algorithm, products and validation, *J. Atmos. Sci.*, 62, 947–973.
- Roger, J. - C., B. Guinot, H. Cachier, M. Mallet, O. Dubovik, and T. Yu (2009), Aerosol complexity in megacities: From size - resolved chemical composition to optical properties of the Beijing atmospheric particles , *Geophys. Res. Lett.* , 36 , L18806, doi:10.1029/2009GL039238.
- Rozanov, V.V., and Kokhanovsky, A.A., 2006: The solution of the vector radiative transfer equation using the discrete ordinates technique: selected applications, *Atmos. Res.*, 79, 241–265.

- Salomonson, V. V., W. L. Barnes, P. W. Maymon, H. E. Montgomery, and H. Ostrow (1989), MODIS : Advanced Facility Instrument for studies of the Earth as a System, *IEEE Trans. Geosci. Remote Sens.*, 27, p 145-153.
- Schulz, H., Harder, V., Ibaldo-Mulli, A., Khandoga, A., Koenig, W., Krombach, F., Radykewicz, R., et al. (2005): Cardiovascular effects of fine and ultrafine particles, *Journal of Aerosol Medicine*, 18, 1-22.
- Seinfeld, J.H., and S.N. Pandis, (1998): *Atmospheric Chemistry and Physics: From Air Pollution to Climate change*, p. xxvii, John Wiley, New York.
- Shettle, E. P. and R. W. Fenn, (1979): *Models of the Aerosols of the Lower Atmosphere and the Effects of Humidity Variations on their Optical Properties. Project 7670, Air Force Geoph. Lab., Massachusetts.*
- Sikka, D. R. (1997): Desert climate and its dynamics, *Curr. Sci.*, 72(1), 35 – 46.
- Smirnov, A., Holben, B.N., Eck, T.F., Dubovik, O., and Slutsker, I., (2000). Cloud-screening and quality control algorithms for the AERONET database. *Remote Sens. Environ.* 73:337-349
- Smirnov, A, Holben, B.N., Lyapustin A., Slutsker, I. and Eck, T.F. (2004), AERONET processing algorithms refinement, *AERONET Workshop, May 10 - 14, 2004, El Arenosillo, Spain.*
- Smith, K. R., Jantunen, M. (2002): Why particles? *Chemosphere*, 49, 867-871.
- Streets, D.G., Fu, J. S., Jang, C. J., Hao, J. M., He, K. B., Tang, X. Y., et al. (2007), Air quality during the 2008 Beijing Olympic Games, *Atmos. Environ.*, 41, 480-492.

- Stull R.B. (1988), An introduction to boundary layer meteorology, *Ed. Springer*, ISBN : 978-90-277-2769-5, 680 pages.
- Su., X., P. Goloub, I. Chiapello, H. Chen, F. Ducos, and Z. Li (2010), Aerosol variability over east Asia as seen by POLDER space-borne sensors, *J. Geophys. Res.*, 115, D24215, doi:10.1029/2010JD014286.
- Sun, Y.L., Zhuang, G.S., Wang, Y., Han, L.H., Guo, J.H., Dan, M., Zhang, W.J., Wang, Z.F., Hao, Z.P. (2004), The air-borne particulate pollution in Beijing-concentration, composition, distribution and sources, *Atmos. Environ.*, 38, 5991–6004.
- Tanré, D., M. Herman, and Y. J. Kaufman, (1996): Information on aerosol size distribution contained in solar reflected spectral radiances. *J. Geophys. Res.*, 101, 19043 – 19060.
- Tanré, D., Y. J. Kaufman, M. Herman, and S. Mattoo, (1997): Remote sensing of aerosol properties over oceans using the MODIS/EOS spectral radiances. *J. Geophys. Res.*, 102, 16971–16988.
- Tie, X., Wu, D., and Brasseur, G. (2009): Lung cancer mortality and exposure to atmospheric aerosol particles in Guangzhou, China, *Atmos. Environ.*, 43, 2375-2377.
- Tucker, C.J., (1979): Red and photographic infrared linear combination for monitoring vegetation. *Rem. Sens. Environ.* 8, 127–150.
- Van de Hulst, H. C., (1957): Light Scattering by Small Particles. *Wiley*, 470 pp.
- Van Donkelaar, A., R.V. Martin, and R.J. Park (2006): Estimating ground-level PM_{2.5}

- using aerosol optical depth determined from satellite remote sensing, *J. Geophys. Res.*, 111, D21201, doi:10.1029/2005JD006996.
- Vaughan, M. A., S. A. Young, D. M. Winker, K. A. Powell, A. H. Omar, Z. Liu, Y. Hu, and C. A. Hostetler (2004), Fully automated analysis of space-based lidar data: An overview of the CALIPSO retrieval algorithms and data products, *Proc. SPIE Int. Soc. Opt. Eng.*, 5575, 16–30.
- Vermeulen, A., C. Devaux, and M. Herman, 2000: Retrieval of the scattering and microphysical properties of aerosols from ground-based optical measurements including polarization. I. Method, *Appl. Opt.*, 39, 6207–6220.
- Volten, H., O. Munoz, E. Rol, J.F. de Haan., W. Vassen., J.W. Hovenier., K. Muinonen, and T. Nousiainen, (2001): Scattering matrices of mineral aerosol particles at 441.6 nm and 632.8 nm, *J. Geophys. Res.*, 106, 17375–17401.
- Wang, J. and Christopher, S. A. (2003) Intercomparison between satellite derived aerosol optical thickness and PM_{2.5} mass: Implications for air quality studies, *Geophys. Res. Lett.*, 30(21), 2095, doi:10.1029/2003GL018174.
- Wang, M., and H. R. Gordon (1994), Radiance reflected from the ocean-atmosphere system: Synthesis from individual components of the aerosols size distribution, *Appl. Opt.*, 33, 7088–7095.
- Wang, X.W., Huang, Y.X., Liu, Z.G., Wei, F., Zhang, T.J. (2007) : Analysis of summer severe Sand-Dust Storms in Gansu Province, *Meteorological Science and Technology*, 35(5), 681-687.
- Waquet, F., P. Goloub, J-L. Deuze, J-F. Léon, F. Auriol, C. Verwaerde, J-Y. Balois, P.

- Francois, Aerosol retrieval over land using a multiband polarimeter and comparison with path radiance method (2007), *J. Geophys. Res.*, 112, D11214, doi:10.1029/2006JD008029.
- Whitby, K.T. and Svendrup, G.M. (1980): California aerosols: their physical and chemical characteristics, *Adv. Environ. Sci. Tech.*, 10, 477.
- Wilson, W.E., Chow, J.C., Claiborn, C., Wei, F.S., Engelbrecht, J. and Watson, J.G. (2002): Monitoring of particulate matter outdoors. *Chemosphere*; 49: 1009–1043.
- Winker, D. M., J. Pelon, and M. P. McCormick (2003), The CALIPSO mission: Spaceborne lidar for observations of aerosols and clouds, *Proc. SPIE Int. Soc. Opt. Eng.*, 4893, 1–11.
- Winker, D. M., W. H. Hunt, and M. J. McGill (2007): Initial performance assessment of CALIOP, *Geophys. Res. Lett.*, 34, L19803, doi:10.1029/2007GL030135.
- Wiscombe W J. (1981): Improved mie scattering algorithms. *Applied Optics*, 19(9): 1505—1509
- Xia, X. A., Chen, H. B., Wang, P. C., Zong, X. M., & Goloub, P. (2005), Aerosol properties and their spatial and temporal variations over north China in spring 2001, *Tellus, Ser. B*, 57, 28 –39.
- Xia, X. A., Chen, H. B., Wang, P. C., Zhang, W. X., Goloub, P., Chatenet, B., Eck, T. F., and Holben, B. N. (2006), Variation of column-integrated aerosol properties in a Chinese urban region, *J. Geophys. Res.*, 111, D05204, doi: 10.1029/2005JD006203.
- Xia, X., H. Chen, P. Goloub, W. Zhang, B. Chatenet, and P. Wang (2007), A

- compilation of aerosol optical properties and calculation of direct radiative forcing over an urban region in northern China, *J. Geophys. Res.*, *112*, D12203, doi: 10.1029/2006JD008119.
- Xu X. D., (2002), Dynamic issues of urban atmospheric pollution models. *J. Appl. Meteorol. Sci. (in Chinese)*, *13 (suppl.)*: 1—12
- Xu, X. D., Ding, G., Zhou, L., et al. (2003), Localized 3D-structural features of dynamic-chemical processes of urban air pollution in Beijing wither, *Chin. Sci. Bull*, *48(8)*: 819—825
- Xu, J., M. H. Bergin, R. Greenwald, J. J. Schauer, M. M. Shafer, J. L. Jaffrezo, and G. Aymoz (2004). Aerosol chemical, physical, and radiative characteristics near a desert source region of northwest China during ACE-Asia, *J. Geophys. Res.*, *109*, D19S03, doi: 10.1029/2003JD004239.
- Xu, X. D., Zhou, X. J., Shi, X.H. (2005), Spatial structure and scale feature of the atmospheric pollution source impact of city agglomeration, *Science in China ser. D Earth Science*, *48(Supp.)*, II 1-24.
- Xu, X. D., Shi, X. H., Zhang, S., J., Ding, G. A., Miao, Q. J., Zhou, L. (2006), Aerosol influence domain of Beijing and peripheral city agglomeration and its climatic effect, *Chin. Sci. Bull.*, *51*, 16, 2016-2026.
- Xuan, J., G. L. Liu, and K. Du (2000), Dust emission inventory in northern China, *Atmos. Environ.*, *34*, 4565– 4570.
- Yamamoto, G., and M. Tanaka, (1969): Determination of aerosol size distribution from spectral attenuation measurements. *Appl. Opt.*, *8*, 447-453.

- Zhang, X.Y., R., Arimoto, and Z. S. An (1997): Dust emission from Chinese desert sources linked to variations in atmospheric circulation, *J. Geophys. Res.*, 102(D23), 28,041–28,047.
- Zhang, Q., Zhao, C.S., Tie, X.X., Wei, Q., Huang, M.Y., Li, G.H., Ying, Z.M., Li, C.C. (2006): Characterizations of aerosols over the Beijing region: A case study of aircraft measurements, *Atmos. Environ.*, 40, 4513-4527, doi: 10.1016/j.atmosenv.-2006.04.032.
- Zhao, X.J., Zhang, X.L., Xu, X.F., Xu, J., Meng, W., Pu, W.W. (2009): Seasonal and diurnal variations of ambient PM_{2.5} concentration in urban and rural environments in Beijing, *Atmos. Environ.*, 43, 2893-2900, doi:10.1016/j.atmosenv.2009.03.009.
- Zhou, C. Y., Liu, Q. H., Tang, Y., Wang, K., Sun, L., He, Y. X. (2009), Comparison between MODIS aerosol product C004 and C005 and evaluation of their applicability in the north of China, *Journal of Remote Sensing*, 1007-4619 (2009) 05-854-19.